

Stability of Split-Aptamers

Dissertation

zur Erlangung des Grades eines
„Doktor rerum naturalium (Dr. rer. nat.)“
der Fachbereiche:
08 - Physik, Mathematik und Informatik
09 - Chemie, Pharmazie und Geowissenschaften,
10 – Biologie,
Universitätsmedizin
der Johannes Gutenberg-Universität

Diplom-Chemiker Thomas Nick

Geboren am 25.04.1986 in Dortmund

Mainz, 09. November 2016



Max Planck **Graduate Center** 
mit der Johannes Gutenberg-Universität



Date of Examination: December 20th, 2016

D77 – Dissertation of the Johannes Gutenberg University, Mainz

The present dissertation was composed at the Max Planck Institute for Polymer Research and the Institute of Pharmacy and Biochemistry at the University of Mainz within the Max Planck Graduate Center (MPGC) in the time between Mai 2013 and November 2016.

I hereby declare that I wrote the dissertation submitted without any unauthorized external assistance and used only sources acknowledged in the work. All textual passages which are appropriated verbatim or paraphrased from published and unpublished texts as well as all information obtained from oral sources are duly indicated and listed in accordance with bibliographical rules. In carrying out this research, I complied with the rules of standard scientific practice as formulated in the statutes of Johannes Gutenberg-University Mainz to insure standard scientific practice.

Thomas Nick

“By three methods we may learn wisdom: First, by reflection, which is noblest; second, by imitation, which is easiest; and third by experience, which is the bitterest.”

Confucius

Abstract

Oligonucleotide aptamers are widely used in fundamental research, diagnostics and technical applications, because of their property to bind analytes with high affinity and specificity. Analyte-binding can cause a change of the flanking nucleotides and thus of the aptamer structure. By combining two binding-sites with a so called communication module, the structural change of one binding-site can be transduced to the other binding-site. However, for such a construct, at least one aptamer has to be split into two strands. The aim is, to develop split-aptamers, which regained their analyte-binding property upon hybridization of the two strands. A significant stabilization of the aptamer upon analyte-binding is desired, which can be determined by monitoring the dissociation of the oligonucleotide-strands.

A force-induced dissociation of a split-aptamer, which binds streptomycin, was investigated by means of single-molecule force spectroscopy measurements. Rate dependent measurements revealed a decrease in the off-rate for the aptamer-streptomycin complex ($k_{\text{off-COMPLEX}} = 0.22 \pm 0.16 \text{ s}^{-1}$) compared to the aptamer, having an empty binding pocket ($k_{\text{off-APTAMER}} = 0.49 \pm 0.11 \text{ s}^{-1}$). In the context of the Bell-Evans potential, a decrease in the Gibbs free energy of $\approx 3.4 \text{ kJ mol}^{-1}$ emerged. The results led to the conclusion that the hydrogen-bonds between both RNA strands mainly contribute to the stability of the aptamer system studied.

In a different approach, the dissociation of oligonucleotides was investigated by means of temperature dependent UV/Vis-absorbance measurements. Here, an increase in the melting temperature upon analyte-binding indicated the functionality of the binding-site. A suitable splitting position was identified for the neomycin-aptamer between the nucleotides A14 and G15. The split neomycin-aptamer showed the same shift in the melting temperature as the original neomycin-aptamer. Thus, the functionality of the binding-site was verified. The binding-sites were connected with a communication module of three nucleotides length. The truncation of the communication module to a length of one nucleotide revealed a decreased functionality of the Hg^{2+} -binding DNA. The simultaneous presence of neomycin molecules compensated the destabilization and the affinity of Hg^{2+} -ions to the binding-site was restored. Thus, an oligonucleotide with a positive allostery was developed, which exhibits a $\approx 13 \text{ }^\circ\text{C}$ larger melting temperature upon binding of both analytes, compared to the unbound aptamer. This system might be the basis for molecular switches.

Zusammenfassung

Oligonukleotid-Aptamere sind weit verbreitet in der Grundlagenforschung, in der Diagnostik und in technischen Anwendungen, weil sie Analyte mit hoher Affinität und Spezifität binden können. Die Analytbindung kann eine Strukturänderung des Aptamers und der flankierenden Oligonukleotide verursachen. Beim Verbinden von zwei Bindungs-Stellen mit einem Kommunikationsmodul, kann die strukturelle Änderung von einer Bindungs-Stelle auf die andere Bindungs-Stelle übertragen werden. Für die Kombination eines Aptamers mit anderen Nukleotiden, ist das Aufspalten des Aptamers in zwei separate Oligonukleotid-Stränge von größter Wichtigkeit. Das Ziel ist es, geteilte Aptamere zu entwickeln, die nach Hybridisierung der Oligonukleotid-Stränge wieder die Bindungs-Stelle ausformen und den Analyten binden. Des Weiteren ist eine signifikante Stabilisierung des Aptamers bei Analyt-Bindung erwünscht, welche anhand der Dissoziation der Oligonukleotid-Stränge bestimmt werden kann.

Eine Kraft-induzierte Dissoziation des gespaltenen-Aptamers, welches Streptomycin bindet, wurde mittels einzelmolekülkraftspektroskopischer Messungen durchgeführt. Raten-abhängige Messungen zeigten eine Verringerung der off-Rate für den Aptamer-Streptomycin-Komplex ($k_{\text{off-COMPLEX}} = 0.22 \pm 0.16 \text{ s}^{-1}$), im Vergleich zum Aptamer mit leerer Bindungstasche ($k_{\text{off-APTAMER}} = 0.49 \pm 0.11 \text{ s}^{-1}$). Im Kontext des Bell-Evans-Potentials, ergibt sich eine Verringerung der Gibbs freien Energie von $\approx 3.4 \text{ kJ mol}^{-1}$. Das Resultat führt zu der Schlussfolgerung, dass hauptsächlich die Wasserstoffbrückenbindungen zwischen den Oligonukleotid-Strängen zur Stabilisierung des Aptamers beitragen.

In einem anderen Ansatz, wurde die Dissoziation der Oligonukleotid-Stränge mittels temperatur-abhängiger UV/Vis-Spektroskopie untersucht. Eine Erhöhung der Schmelztemperatur des Aptamers bei Analyt-Bindung, war ein Zeichen für eine funktionelle Bindungs-Stelle. Eine geeignete Spalt-Position für das Neomycin-Aptamer, wurde zwischen den Nukleotiden A14 und G15 identifiziert und anhand einer Erhöhung der Schmelztemperatur bestätigt. Anschließend wurden die Bindungs-Stellen mittels eines Kommunikations-Moduls verbunden, das aus drei Nukleotiden bestand. Die Verkürzung des Kommunikations-Moduls auf ein Nukleotid führte zu einer verringerten Funktionalität der Hg^{2+} -bindenden DNA. Die gleichzeitige Präsenz von Neomycin Molekülen, kompensierte die Destabilisierung und stellte die Funktionalität der Hg^{2+} -bindenden DNA wieder her. Damit wurde ein Oligonukleotid mit positiver Allosterie entwickelt, das eine $\approx 13 \text{ }^\circ\text{C}$ Schmelztemperatur bei gleichzeitiger Anwesenheit von Hg^{2+} -Ionen und Neomycin Molekülen aufweist. Dieses System könnte eine Basis für neue molekulare Schalter darstellen.

Glossary

A	absorbance
AFM	Atomic Force Microscope
α_s	sensitivity
$\alpha(T)$	fraction folded
AMP	adenosine monophosphate
APTES	3-Triethoxysilylpropylamine
ATP	adenosine triphosphate
bp	base pair
c	concentration
COM1	combined Hg^{2+} -binding DNA - neomycin-aptamer, separated by 1 nt
COM2	combined Hg^{2+} -binding DNA - neomycin-aptamer, separated by 2 nt
COM3	combined Hg^{2+} -binding DNA - neomycin-aptamer, separated by 3 nt
cRNA	complementary RNA
D	distance
ΔC_p°	heat capacity
ΔG°	Gibbs free energy
ΔH°	standard enthalpy
ΔS°	standard entropy
Δz_c	deflection of the cantilever
DNA	deoxyribonucleic acid
ϵ_{LJ}	depth of the potential well
ϵ_m	dielectric constant of the medium
ϵ	material-specific extinction coefficient
F	force
FD	force-distance
FJC	freely jointed chain
FWHM	full width at half maximum
h	Planck constant
ITC	isothermal titration calorimetry
k	proportionality constant
K_a	association constant
k_B	Boltzmann constant
k_{cant}	cantilever spring constant

K_d	dissociation constant
k_{eff}	effective spring constant
k_L	PEG-linker spring constant
k_{off}	off-rate
k_{on}	on-rate
L	contour length
l	path length of the beam of light through the material sample
λ_f	frequency of binding events
l_K	chain link size
MD simulation	molecular dynamics simulation
mRNA	messenger ribonucleic acid
N_b	number of bonds
NHS	<i>N</i> -Hydroxysuccinimid
NMR spectroscopy	nuclear magnetic resonance spectroscopy
nt	nucleotide
PCR	polymerase chain reaction
PEG	polyethylene glycol
pN	pico newton
q	charge of an atom
r_{LJ}	distance between the tip and the sample
r_f	loading rate
RNA	ribonucleic acid
RNATs	RNA thermometers
RT-PCR	reverse transcription polymerase chain reaction
S	Svedberg
SAD	single-wavelength anomalous diffraction
SELEX	systematic evolution of ligands by exponential enrichment
SMFS	single-molecule force spectroscopy
θ_B	fraction of bound binding partner B
T_m	melting temperature
U	photodiode-voltage
UTR	untranslated region
UV	ultra violet
v	velocity
$U(r_{LJ})$	Lennard-Jones potential

Vis	visible
x	end-to-end distance
x_{β}	width of the potential
x_{cant}	distance from the bond minimum to the external potential minimum
z_c	cantilever deflection
z_p	z-piezo-position

Table of Content

1. Background and Motivation	1
2. Experimental Details.....	7
2.1 Single-Molecule Force Spectroscopy - Sample Preparation	7
2.1 Single-Molecule Force Spectroscopy - Measurements	8
2.2 SMFS - Data Analysis	9
2.3 FWHM Calculation	10
2.4 UV/Vis-Spectroscopy Measurements.....	10
3. How Can One Receive the Off-Rate of RNA-Strands?.....	13
3.1 Intermolecular Interactions.....	13
3.2 Atomic Force Microscopy	14
3.3 Measuring-Mode – Force Spectroscopy.....	17
3.4 Theory of Force Spectroscopy.....	22
3.5 Motivation	30
3.6 Results and Discussion	30
3.7 Summary and Conclusion.....	40
4. Split-RNA-Aptamer, Capable of Streptomycin-Binding.....	41
4.1 Aptamers.....	41
4.2 Single-Molecule Force Spectroscopy of RNA	46
4.3 Motivation	47
4.4 Rupture Geometries.....	47
4.5 Summary and Conclusion.....	59
5. Combination of Analyte-Binding-Oligonucleotides	61
5.1 Temperature Dependent UV/Vis-Absorbance Measurements	61
5.2 Neomycin-Aptamer	63
5.3 Hg ²⁺ -Binding DNA.....	75
5.1 Theoretical Consideration for the Combination of two Different Binding-Sites	79
5.2 Control Experiments.....	80
5.3 Summary and Conclusion.....	82
6. Communication Between Binding-Sites	85
6.1 Combined Split-Neomycin-Aptamer with a Hg ²⁺ -Binding DNA	86
6.2 Summary and Conclusion.....	92
7. Summary and Conclusion	95
8. Bibliography	99

9. Appendix	109
10.Acknowledgments.....	113
11.List of Publications.....	115
12.List of Presentations.....	115
13.Curriculum Vitae	116

1. Background and Motivation

Oligonucleotide aptamers have been investigated in the context of fundamental research. [1] Aptamers are capable of analyte binding with high affinity and specificity and their binding-constants reach down to the nanomolar regime. [2, 3] Furthermore, aptamers are selected by means of the Systematic Evolution of Ligands by EXponential Enrichment (SELEX) process. [4] With this process, aptamers can be identified, which bind to almost any analyte (Figure 1.1a). [5] The variety of suitable analytes ranges from single ions, over molecules to proteins. [6] Binding occurs at a binding-site, referred to as binding-pocket, which mostly constitutes of a stretch of unhybridized nucleotides flanked by hybridized oligonucleotides (Figure 1.1b). [7] Thus, aptamers have the potential to be widely adopted for applications in diagnostics and industry.

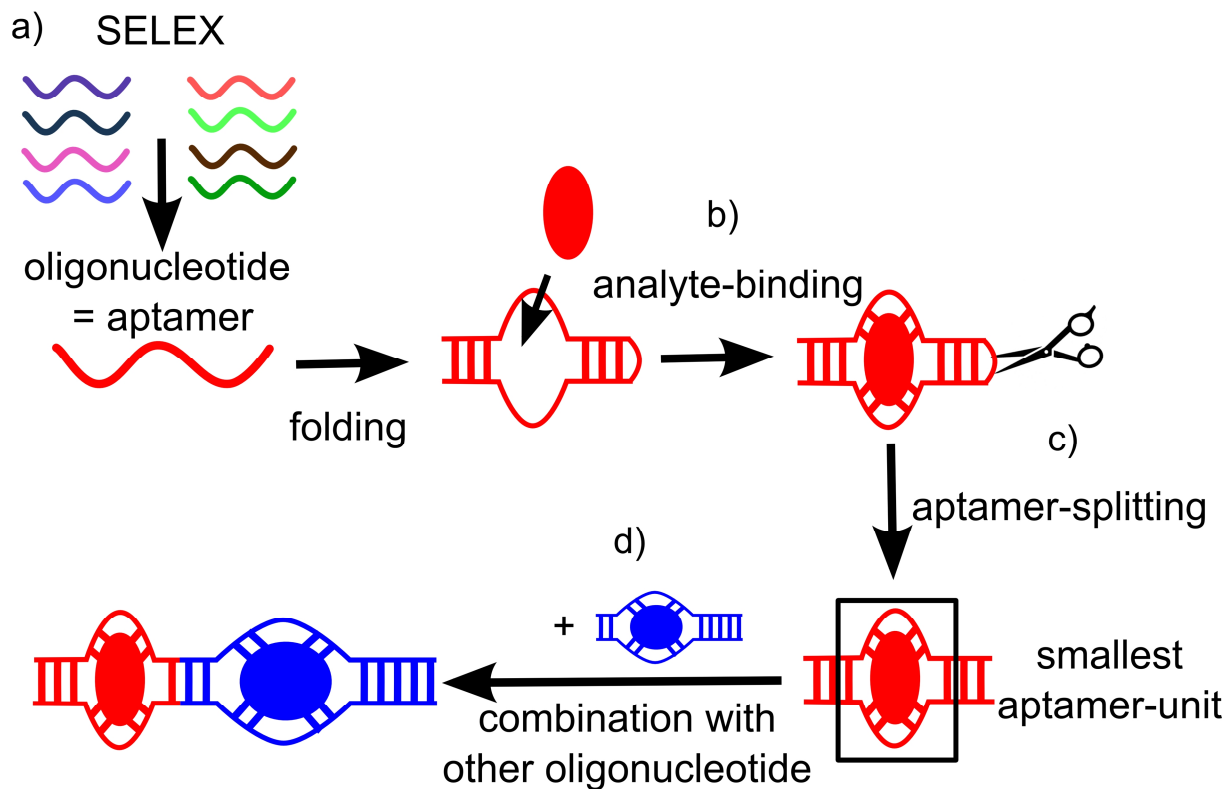


Figure 1.1: Concept of constructs used in aptamer-aptamer-communication studies. The development is sketched from the selection (a), over analyte-binding (b), towards splitting (c) and combination with other oligonucleotides (d). One aptamer construct is depicted in red and the other aptamer in blue. The corresponding analytes are depicted as red and blue ovals, respectively. The hydrogen-bonds between the nucleotides as well as between the nucleotides and the analytes are also depicted in red and in blue, respectively.

The first aptamers, developed by the SELEX-process, were RNA aptamers. Later, the SELEX-technology was adapted for the selection of DNA aptamers and catalytic nucleic acids, called ribozymes and DNAzymes. [8] A decade after the invention of the SELEX-process, natural aptamers were found in nature. [9, 10] There, aptamers are parts of so called riboswitches, which play a major

role in gene expression. [11] The working principle of those switches is a structural rearrangement of the binding pocket upon analyte-binding, which changes the accessibility of the neighboring nucleotides. [12, 13] The switch can trigger, for instance, a regulatory process like the translation from mRNA into proteins [11] or artificial processes like an induced nanoparticle aggregation [14, 15] or the organization of DNA nanostructures like DNA three-way junctions. [16]

Here split-aptamers are investigated, which are obtained by splitting the aptamer into two separated oligonucleotide strands. This concept of split-aptamers can only be applied to aptamers, which have an internal loop as binding-pocket, which is framed by two stretches of oligonucleotides. The hybridization of both strands stabilizes the binding-pocket and results in a functional split-aptamer (Figure 1.1c). [17, 18] The advantage of split-aptamers is a regained functionality of the hybridized oligonucleotide strands. [19-29] Analytes are only bound to the functional aptamer, which opens up the possibility to control analyte-binding by hybridization. Thus, split-aptamers can be even fused with other oligonucleotides to create switches (Figure 1.1d).

Interesting data for understanding analyte-binding of split-aptamers can be obtained by means of single-molecule force spectroscopy (SMFS) measurements. The latter is a very powerful technique, because it provides information about the forces, which are needed to separate single molecules (Figure 1.2a and b). [30]

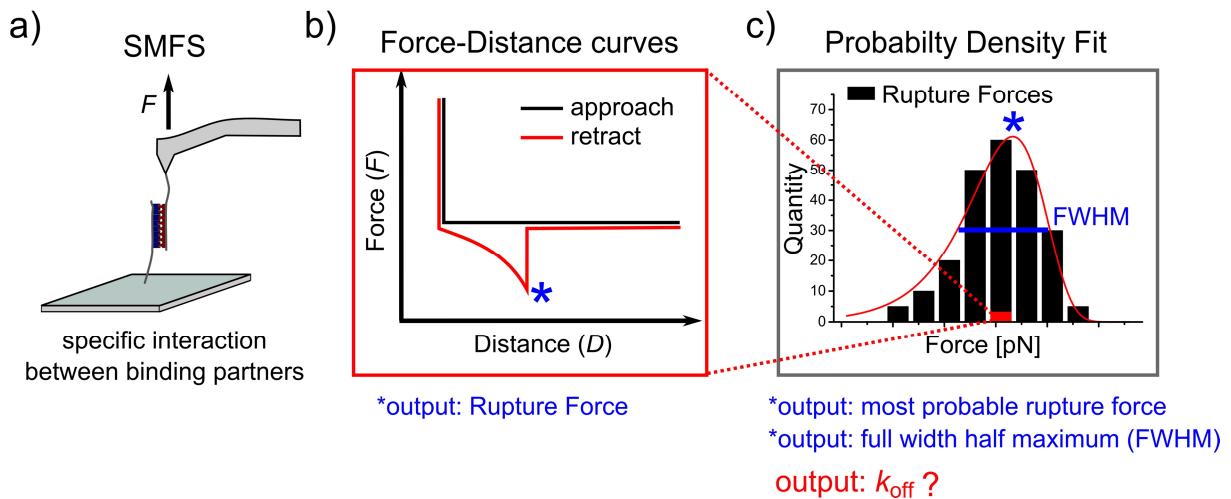


Figure 1.2. a) Scheme of SMFS measurements, performed with complementary RNA-strands, immobilized on the measuring probe and on the substrate, respectively. b) Exemplary Force-Distance curve of a specific rupture event. c) Example of a force distribution, which was fitted by means of a probability density fit. The latter revealed the full width at half maximum (FWHM) and the most probable rupture force. The question is addressed, whether this fit also provides reliable values for k_{off} .

The forces, which are required to rupture the non-covalent bonds between the molecules, allow inferring the natural off-rate (k_{off}) of the oligonucleotide strands. [31-33] The latter is a kinetic key parameter, which describes the rate of the dissociation of the complex. The lower the k_{off} value, the

longer the complex remains intact. [34] The lifetime of a complex is typically calculated by $1/k_{\text{off}}$. [35]

The SMFS technique opened up the possibility to analyze molecular bonds [31], conformational changes [36] or the adhesion between molecules and surfaces. [37] In order to analyze aptamer-analyte interactions by SMFS, aptamers were immobilized on the sample and the analyte on the tip of the cantilever. [38] This approach is still the standard for the investigation of protein-binding aptamers. Large analytes, like proteins can be immobilized on surfaces without blocking the subunit, which is necessary for binding. Smaller molecules have a lower number of functional groups, which are not involved in the binding process, which makes the immobilization more difficult. [39] Here, the split-aptamer concept is a promising approach, because the aptamer-structure is rebuilt during the approach- and retract-cycle of the cantilever tip and an unhindered analyte-binding is facilitated. The split-aptamer concept has been successfully applied to split-DNA-aptamers, which bind the analytes AMP [18], malachite green [40] and Cu^{2+} [41]. There is interest in expanding the split-aptamer concept to RNA for various reasons, including the possibility to develop switching units into mRNA. To the best of my knowledge and through literature survey, only RNA-oligonucleotides featuring a non-functional internal loop or bulge have been investigated by SMFS. Those binding motifs were either caused by non-complementary bases in both RNA-strands [42] or nucleotide mismatches and protuberances within the duplex. [43] In this thesis an RNA-aptamer was investigated, which featured an internal loop that is simultaneously a binding-pocket for streptomycin. The goal was to find out, whether the destabilizing effect of the internal loop on the oligonucleotide could be compensated by streptomycin-binding. Streptomycin is a relevant analyte, which is used in agriculture as antibiotic. Thus, the detection of streptomycin in milk and meat is highly important.

In the first part of the thesis, the stability of a complementary RNA-oligonucleotide and a streptomycin-aptamer is elucidated. In order to increase the efficiency of the performed SMFS-measurements, a data analysis method was evaluated, which utilizes a probability density function to extract k_{off} directly from one measurement of rupture forces at one loading rate (Figure 1.2c). [37] A parameter, which has been neglected in literature, is the full width at half maximum (FWHM) of the probability fit. I observed that the FWHM has a significant influence on the determined k_{off} value. The applicability of this data analysis method is discussed on the basis of the results obtained from the rupture of complementary RNA experiments, as well as of results, presented in literature (**chapter 3**).

In the second part of the thesis, the discussion regarding the increase in the stability of a split-aptamer upon binding of streptomycin is presented (**chapter 4**). In addition, the split-aptamer concept allows conducting the SMFS experiments in the rupture geometries “shear” and “zipper” in one course of experiments. Those experiments were facilitated with the same cantilever, by using glass substrates with oligonucleotides, which were either immobilized with their 3'- or 5'-ends to the glass. I discussed

in particular, the off-rate of the aptamer alone, in the presence of excess analyte, and of a similar sequence without a binding pocket.

Interesting molecular switches can be developed by the combination of binding-sites (Figure 1.3). For an oligonucleotide with several binding-sites for different analytes, binding of the first analyte may directly affect the binding of the second analyte. This phenomenon is referred to as allostery (from the Greek *allos*, "other," and *stereos*, "solid object"). [44] Allostery can be either positive (favored binding) or negative (unfavored binding). [45] The structural information from the first binding-site towards the second binding-site can be transduced by the sequence between the binding-sites, also referred to as communication module. [8] In aptamer engineering, different oligonucleotide-units are combined. Depending on the sensitivity of the binding-sites on the flanking nucleotides, analyte-binding is either unaffected (Figure 1.3a), decreased (Figure 1.3b) or increased by the other binding-site (Figure 1.3c). The goal was to identify a combined oligonucleotide, which has the property of positive allostery.

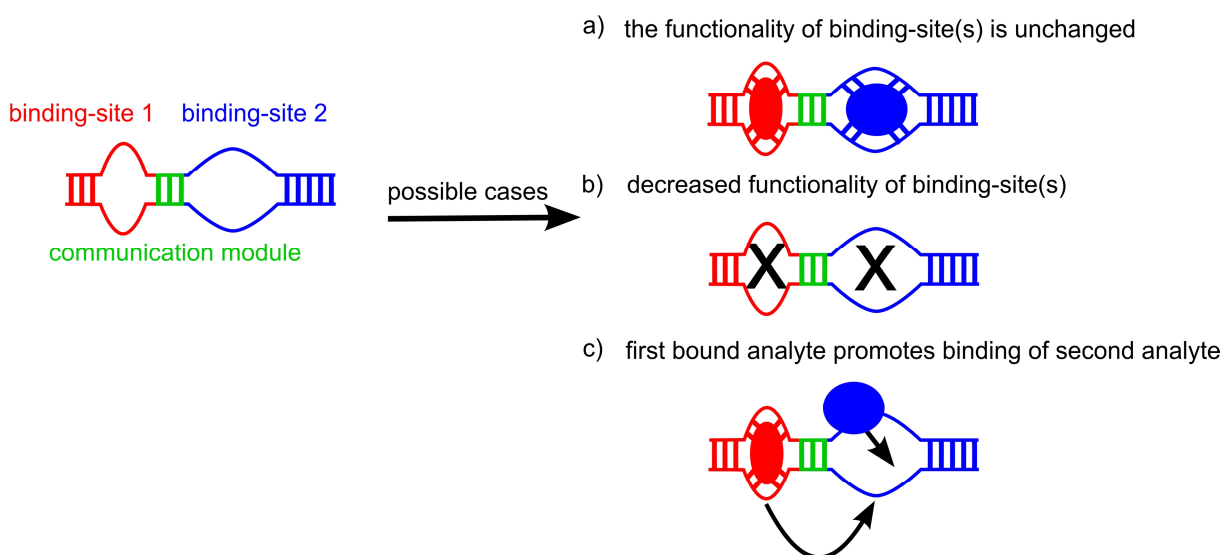


Figure 1.3: Scheme of the combined oligonucleotide with the possible cases for analyte-binding

In literature, mostly allosteric oligonucleotides, featuring communication modules with a length of less than 7 nucleotides, were reported. [46] In general, the communication module is structurally relatively unstable, which allows the transduction of structural changes from one binding-site to the other. [47, 48] The identification of communication modules is typically carried out by combinatorial methods [49, 50] as well as by rational design [45, 46]. In literature, the insertion of unsymmetrical communication modules was performed for the creation of logic gates. Here, the input is given by analyte-binding to the binding-sites and a corresponding output according to the logical operation: AND, OR, NAND, NOR. [51]

In order to investigate significantly stabilized binding-sites, those constructs were chosen, which exhibit an increased melting temperature (T_m) upon analyte-binding (Figure 1.4). As readout, temperature dependent UV/Vis-absorbance measurements were performed. During this so called melting-process, the non-covalent interactions between the hybridized oligonucleotides are broken. [52] The melting temperature is a measure of oligonucleotide stability and is defined as temperature, at which half of the oligonucleotides are separated. [53] In literature, only a few examples of analyte-binding oligonucleotides have been reported, which exhibit an increased melting temperature upon analyte-binding (Figure 1.5). [54-57] The increase in the melting temperature is assumed to depend on the number of intermolecular interactions, formed between the analyte and the binding-site. Thus, an increased melting temperature indicates the functionality of the binding-site.

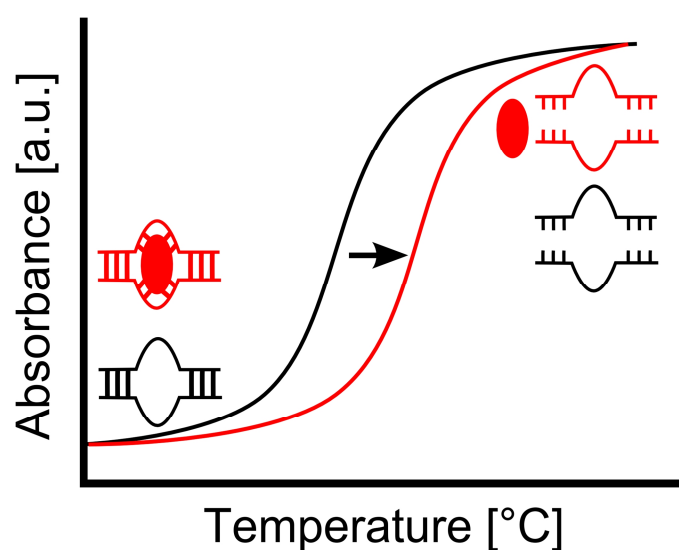


Figure 1.4: The absorbance versus temperature plot of oligonucleotides has a characteristic sigmoidal shape. The melting curve corresponding to the aptamer with empty binding pocket is sketched in black. The melting curve of the aptamer-analyte complex is shown in red. The arrow indicates the increase in the melting temperature upon analyte-binding. As readout for the functionality of the binding-sites, temperature dependent UV/Vis-absorbance measurements were performed.

In this work, the combination of two binding-sites with a communication module of three nucleotides length was performed (Figure 1.5). To my knowledge, the investigation of combined binding-sites by means of temperature dependent UV/Vis-absorbance measurements has not been conducted before. Especially the neomycin-aptamer and the Hg^{2+} -binding DNA have been prominent for a significant increase in the melting temperature. Upon binding of the neomycin molecule, 16 hydrogen bonds are built, which cause a shift in T_m of $\approx 6^\circ\text{C}$ at a NaCl concentration of 80 mM. It has been shown that the temperature shift upon analyte-binding of the Hg^{2+} -binding DNA depends on the number of binding-sites and also on the nucleotides, flanking the binding-site. This neighboring effect was reported for a Hg^{2+} -binding DNA with two binding-sites. [58] There, the maximal increase in the melting temperature upon analyte-binding was 29°C . Understanding how aptamers can systematically be combined, may lead to molecular switches with applications in biosensing. Especially combined

oligonucleotides, which exhibit a higher melting temperature upon analyte-binding could have applications as switches in gene regulation.

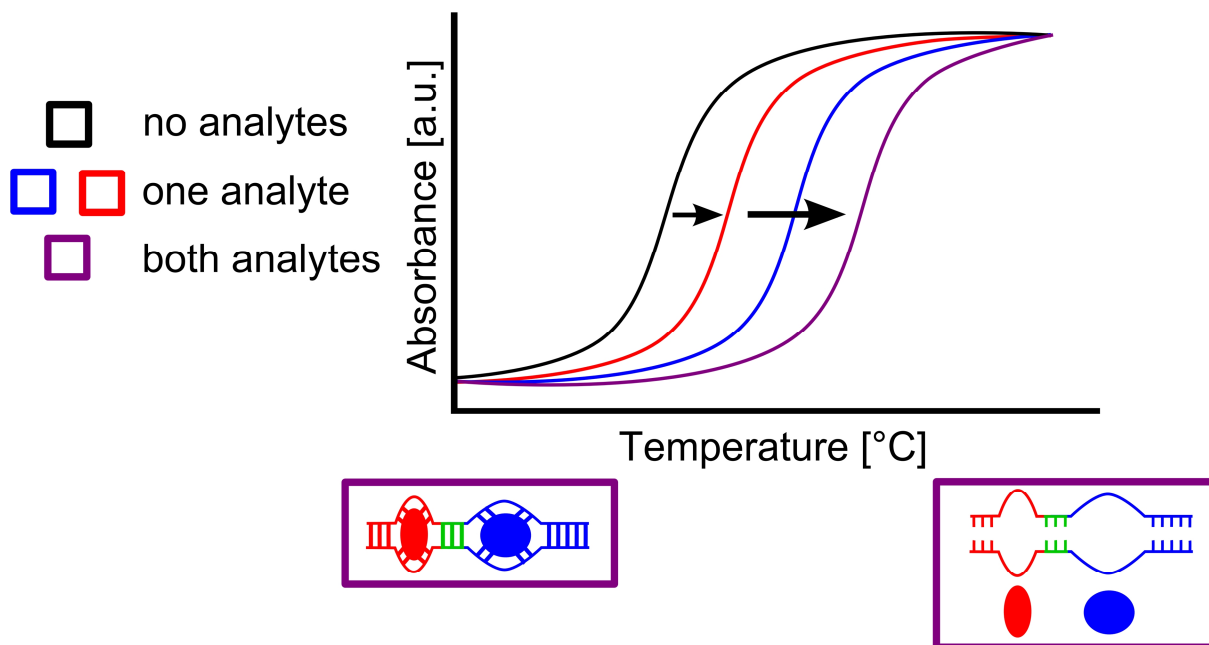


Figure 1.5: Scheme of the melting curves that I expect for the combined oligonucleotide, with the color-code: black – no analytes, red – neomycin, blue – Hg^{2+} and violet – both analytes. Exemplarily, the structures of the combined oligonucleotide with both analytes are depicted in their start and end state.

In the third part, the results of a combined oligonucleotide are elucidated. It was tested, whether the Hg^{2+} -binding DNA as well as the neomycin-aptamer keep their functionality in a chosen buffer. This property is fundamental for the combination of the binding-sites. Furthermore, I located a position within the neomycin-aptamer strand, which can be split and combined with the Hg^{2+} -binding DNA, without a loss of functionality (**chapter 5**). In order to test, at which length of the communication module the functionality of one binding-site is reduced and influenced by the other analyte, the communication module was truncated from 3 to 1 nucleotide. An allosteric oligonucleotide would show a different affinity for one analyte, depending whether the other analyte is present or absent (**chapter 6**).

2. Experimental Details

2.1 Single-Molecule Force Spectroscopy - Sample Preparation

Covalent and directed immobilization of the oligonucleotides to the tip and the substrate is achieved by a NHS-PEG-Maleimide-spacer. All oligonucleotides were purchased from IBA GmbH (Göttingen, Germany). The scanning force microscopy chip (MSCT; Bruker, Camarillo, CA), supporting the cantilever and tip, was washed in 20 mL chloroform (Fischer Chemical) for 15 minutes. After drying in a stream of argon gas, the chip was placed inside an argon gas flushed desiccator (5 L). One tray with 30 μ L APTES (Santa Cruz Biotechnology, Heidelberg, Germany) and another tray with 10 μ L trimethylamine (Sigma-Aldrich) was placed next to the cantilever. After 2 h of reaction time, the trays were removed and the desiccator was flushed again with argon gas (\approx 1 bar) to store the amino functionalized cantilever for 2 days. A portion of 2.5 mg Maleimide-PEG-NHS (Rapp Polymere GmbH, Tübingen, Germany, molecular weight, 5000 g/mol) was dissolved in 0.5 mL chloroform and mixed inside a small in-house built Teflon-reaction chamber. The chip was placed inside and the reaction chamber was closed with a cap to avoid evaporation of the solvent. After two hours of incubation, the chip was washed in a glass beaker filled with chloroform. After drying the chip in a stream of argon gas, it was placed on Parafilm® in a polystyrene Petri dish. The solutions were prepared with highly pure water provided by a Sartorius Arium 611 VF purification system (MilliQ, specific resistivity of 18.2 M Ω •cm). A mixture of 10 μ L (100 μ M) Oligonucleotide, 180 μ L milliQ water, 4 μ L EDTA (100 mM, pH 7.5, Carl Roth), 5 μ L Hepes (1 M, pH 7.5, Sigma-Aldrich), 1 μ L TCEP hydrochloride (500 mM, Thermo Fischer Scientific) and 4 μ L Hepes (1 M, pH 9.6, Sigma-Aldrich) was produced for three chips. The chip was positioned inside the drop and incubated for 16 h. The incubation was stopped by washing with buffer solution (3 x 5 min).

As substrate, an amino-functionalized slide type A+ (Schott Nexterion, Jena, Germany, cat. No. 1064875) was incubated with borate-buffer (500 mM sodium borate pH 8.5, Alfa Aesar) for 1 h. The slide was dried under a stream of argon gas and placed in a disposable petri dish. An amount of 2 mg Maleimide-PEG-NHS was dissolved in 15 μ L borate-buffer and dropped on the substrate. The reaction solution was covered with a coverslip. After incubation for 1 h, the coverslip was washed away under flowing milliQ water. A mixture of 10 μ L (100 μ M) thiol functionalized oligonucleotide, 180 μ L milliQ water, 4 μ L EDTA (100 mM, pH 7.5), 5 μ L Hepes (1 M, pH 7.5), 1 μ L TCEP hydrochloride (500 mM) and 4 μ L Hepes (1 M, pH 9.6) was prepared, being sufficient for two experiments. The cantilever was positioned inside the drop and incubated for 16 h. The incubation was stopped by washing with buffer solution (3 x 5 min). For the verification of a successful functionalization of the cantilever tips with RNA-strands, x-ray Photoelectron Spectroscopy measurements (XPS) were performed by Hao Lu (Appendix, chapter 9).

Table 2.1: Oligonucleotides, used for the SMFS measurements. DNA nucleotides are indicated in upper case and RNA oligonucleotides in lower case.

Oligonucleotide	Sequence 5' → 3'
First strand (cantilever)	HS-gga ucg cau uuu gga cuu cug cc
Second strand(sample)	HS-cgg cac cac ggu cgg auc
Ctr-complementary to b (sample)	HS-gau ccg acc gug gug ccg
ssDNA	HS-A ₂₀ -GAG CCU AAA ACA UAC CAG AGA
Ctr. First strand(cantilever)	gga ucg cau uug gac uuc ugc c-SH
Ctr. Second strand (sample)	cgg cac cac ggu cgg auc-SH
Zip - Second strand	HS-cgg cac cac ggu cgg auc

2.1 Single-Molecule Force Spectroscopy - Measurements

The measurements were performed with a JPK Instrument NanoWizard™ III (JPK Instruments AG, Berlin, Germany) Scanning Force Microscope (SFM). The thermal tune of the V-shaped Si₃N₄ cantilever type C (MSCT; Bruker, Camarillo, CA) provided cantilever spring constants, ranging from 0.008 to 0.011 N/m with an accuracy of 10 %. [59] It has been reported for the streptavidin-biotin-system that an increase in the temperature of 7 K, k_{off} decreased by a factor of more than 10. [60] SMFS measurements of complementary DNA strands also revealed a strong dependency on the temperature and thus on the rupture forces. [61] Therefore, all measurements were performed at 300 ± 2 K, which was measured by a High-Temperature-Heater (JPK Instruments AG, Berlin, Germany) inside the acoustic chamber of the SFM. The SMFS measurements were carried out in a small volume closed liquid cell (SmallCell™, JPK Instruments AG, Berlin, Germany) filled with the buffer composition: 50 mM Tris (Alfa Aesar), 250 mM NaCl (Carl Roth, Karlsruhe, Germany), 5 mM MgCl₂, pH = 7.4 (Carl Roth, Karlsruhe, Germany). The buffer solution has the same composition as the selection buffer, which was used in the SELEX-Process and in the Strepto-Tag-Purification. [62, 63] To obtain single binding events, the approach velocity was set to 1000 nm/s with a trigger setpoint of 100 pN. The sampling rate was set to 20 kHz to ensure a sufficient amount of data points. [64] The retract velocity was varied in steps from 25 – 1600 nm/s. To achieve adequate statistics, 1000 force-distance curves were collected for each set of measurements. The experiment was carried out at 400 - 1000 different positions on a 100 μm² big sample area. At a streptomycin (Sigma Aldrich) concentration of 50 μM, 98% of the binding pockets should be occupied. For control experiments, with different samples or streptomycin solutions, the liquid cell was rinsed with 3 mL buffer solution. After thermal equilibration was achieved (≈ 30 min) the next measurement was started.

2.2 SMFS - Data Analysis

The program JPK Data Processing software (version spm-4.3.19) was used for the data analysis. The values of the rupture forces (F) were obtained from the last detectable force-jump in the retraction curve of the force spectroscopy measurements. In my analysis, rupture-forces < 100 pN with a clear single event were selected (Figure 2.1d). The force-distance (F-D) curves, which showed no event, multiple events or adhesion events were not evaluated (Figure 2.1a-c). The obtained rupture-forces were plotted in histograms by using a bin size of 4 pN. The bin size corresponds to the value of the root mean square deviation of the baseline at a retract velocity of 25 nm/s.

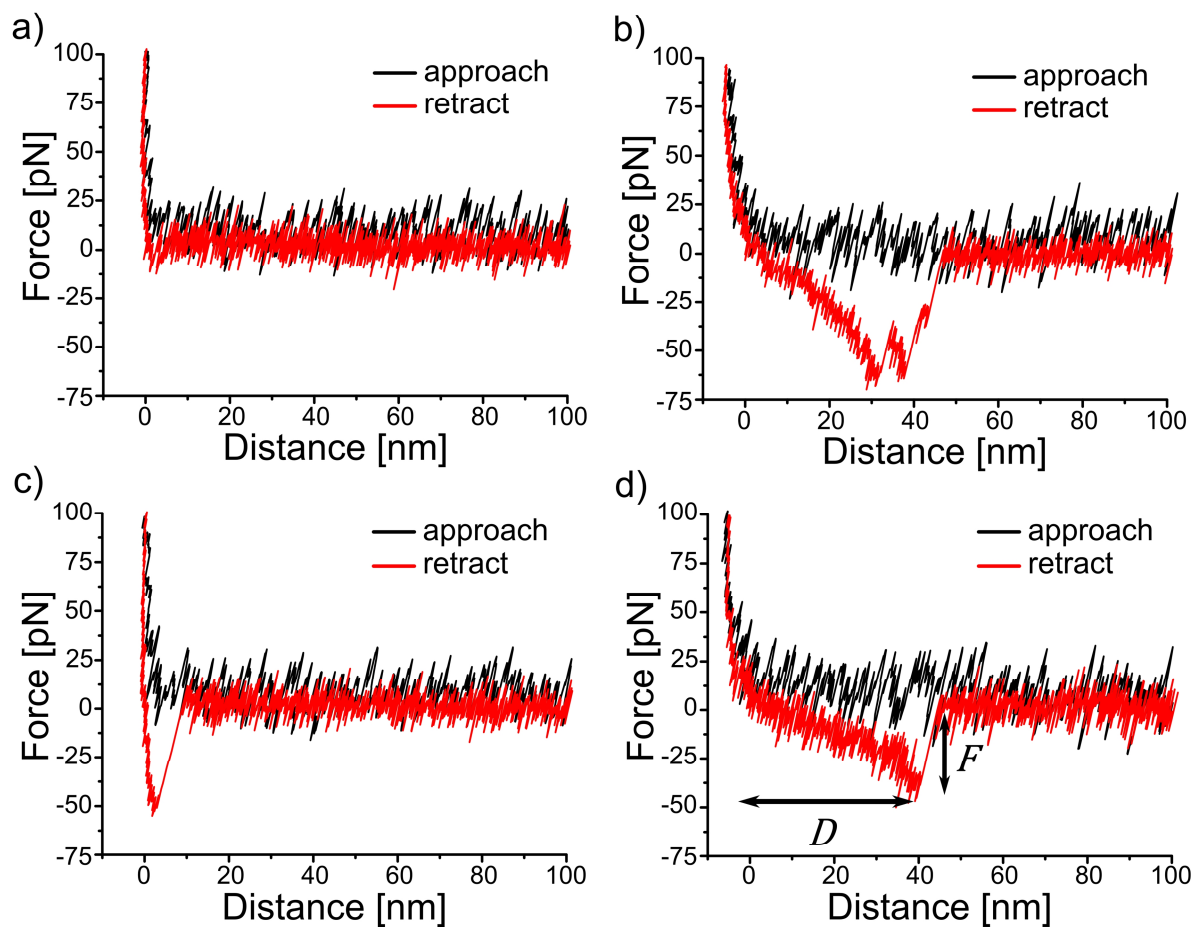


Figure 2.1. Exemplary force distance curves: a) no rupture of oligonucleotides, b) rupture event of several oligonucleotides, c) adhesion event and d) specific rupture event.

The effective spring constant k_{eff} of the cantilever linker system was estimated from the slope before the force-jump, which is described in detail in chapter 3.3.3. The effective loading rate for one rupture event was calculated by multiplying the retract velocity (v) with the effective spring constant. To obtain the averaged effective loading rate (r_f), the logarithm of the single effective loading rates were plotted in a histogram and fitted with a Gaussian fit (chapter 3.6.3). The most probable rupture

force is the peak value of the probability density function 3.33. [65] The parameter k_{off} and x_{β} were calculated, as explained in paragraph 3.4.2.

2.3 FWHM Calculation

The calculations for the width of the probability distributions were performed together with Dominik Pilat by means of the program Matlab R2012a. The maximum of the probability function was determined and the function was moved along the Y-axis at half maximum. The intersections with the x-axis were identified. The distance between the intersections is the full width at half maximum. The first derivative is used to calculate the x_{β} and k_{off} values for a constant F_{max} and a constant loading rate.

2.4 UV/Vis-Spectroscopy Measurements

The oligonucleotides, which were used in the UV/Vis-measurements were purchased from metabion (Planegg, Germany). The samples for the UV/Vis measurements were prepared in 1.5 mL Eppendorf tubes. The sodium phosphate buffer (20 mM, pH 7, Sigma-Aldrich), which was used for all measurements, contained 100 mM NaCl. For the samples, the RNA was added to a final concentration of 1 μ M hybridized oligonucleotide. The concentration of the stock solutions were tested beforehand by NanoDrop ND-2000 (Peqlab, Erlangen, Germany) to verify the concentration, given by the manufacturer. The analytes were added in the final step to a concentration of 12 μ M neomycin (neomycin trisulfate salt hydrate, Sigma-Aldrich) and 10 μ M Hg^{2+} ($HgCl_2$, Sigma-Aldrich). Following, the samples were heated at 90 °C for one minute and mixed at 300 rpm at 20 °C for 1 h to ensure hybridization. In order to degas the samples, they were treated for 5 min. in a SpeedVac Concentrator plus (Eppendorf, Hamburg, Germany) with the settings: V-AL, RT, 130 mbar. The UV/Vis-melting measurements were performed in a JASCO V-6500 spectrophotometer (Jasco, Groß-Umstadt, Germany) UV-visible spectrophotometer in quartz cuvettes (Hellma 114-OS, Müllheim, Germany) with a path length of 1 cm and a volume of 1.4 mL. The melting was carried out by raising the temperature from 20 °C to 85 °C at a rate of 0.5 °C/min, in case not further specified in the text. The absorbance values were measured every degree at 260 nm. The samples were equilibrated for 10 minutes at the starting temperature. Usually six cuvettes were placed inside the measurement chamber: One reference cuvette with the buffer, besides the cuvettes filled with oligonucleotide samples. The spectroscopic data were exported as ASCII files and analyzed by means of the program OriginPro version 9.1 (OriginLab™ Corporation). The data analysis was performed in accordance with the van' Hoff analysis as described in chapter 5.1, which provided the melting temperature (T_m).

Table 2.2: Oligonucleotides, used for the UV-melting experiments. DNA nucleotides are indicated in upper case and RNA oligonucleotides in lower case.

Oligonucleotide	Sequence 5' → 3'
Hg-Apt-a	CCG CG TT CTC CG
Hg-Apt-b	CG GAG TT CG CGG
Neo-Apt-ori	gga cug ggc gag (2AP)ag uuu agu cc
Neo-Hg-Apt-a	gga cug ggc ga CGA ACT CCG
Neo-Hg-Apt-b	CGG AGT TCG g(2AP)a guu uag ucc
Neo-Hg-Apt-c	gga cug ggc ga CGT TCT CCG
Neo-Hg-Apt-d	CGG AGT TC g(2AP)a guu uag ucc
Neo-Hg-Apt-e	gga cug ggc ga GT TCT CCG
Neo-Hg-Apt-f	CGG AGT T g(2AP)a guu uag ucc
Neo-Hg-Apt-g	gga cug ggc ga T TCT CCG
Neo-Hg-Apt-c-mut	gga cug agc ua CGT TCT CCG

3. How Can One Receive the Off-Rate of RNA-Strands?

In this chapter, I will give an introduction into the single-molecule force spectroscopy technique (SMFS). The latter enables the observation of dissociation processes of binding partners on the molecular level. In particular the forces are measured, which are needed to break the intermolecular interactions, which act between the binding partners. Within this chapter I address the question, to which extend the distributions of rupture forces can be used to calculate reliable off-rates.

3.1 Intermolecular Interactions

The intermolecular interactions are considered as forces, which hold macromolecules together. The forces, being most important for nucleic acids, are electrostatic interactions, hydrogen bonding, and van der Waals forces. Although referred to as forces, the energy required to break the intermolecular interactions is usually mentioned. The latter is with < 25 kJ/mol significantly smaller than for covalent bonds (≈ 350 kJ/mol). Macromolecules are built by the collective contribution of intermolecular forces, which stabilize the final structure.

In oligonucleotides, **electrostatic interactions** are formed e.g. between Na^+ -ions and the negatively charged phosphate-backbone. The binding energy (E) of those electrostatic interactions is given by Coulomb's-law:

$$\Delta E = -k \frac{q_1 q_2}{\epsilon_m r} \quad (3.1)$$

with the charge of the atoms (q_1 and q_2), the distance between the atoms (r), the dielectric constant of the medium (ϵ_m) and a proportionality constant (k). Usually the binding energies of two oppositely charged groups in a biomolecule is in the range of ≈ -6 kJ/mol (at a charge of $1e$ of the functional groups, with a distance of 0.3 nm and a dielectric constant of 80). [66] Charged groups of macromolecules, which are less accessed by water molecules have dielectric constants in the range of $2-20$. Thus, the binding energy of oppositely charged groups can vary by an order of magnitude. [67]

Hydrogen bonds are in principle electrostatic interactions between molecules, which are partially charged. [68] These molecules (e.g. water molecules) have dipole moments due to the different electronegativity of the atoms and align with other dipole molecules. The acceptor atom (H) decentralizes the charge of the donor atom (e.g. O, N) and the dipoles are compensated. For the hydrogen bond in water, the attraction of electrostatic charges is strongest at a distance of 0.272 nm to the donor atom. An angle of $\theta = 180^\circ$ (Figure 3.1) between the donor and acceptor results in the largest energy of the hydrogen bonds ($E_{\text{O-H}\dots\text{O}}$ $12 - 25$ kJ/mol). [69]

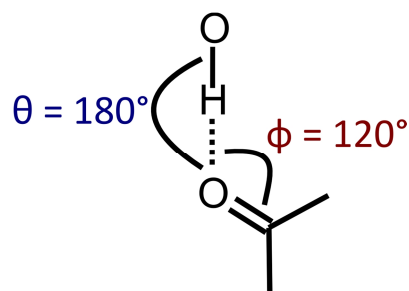


Figure 3.1: Scheme of the orientation for the largest energy between a hydrogen bond donor and acceptor.

Hydrogen bonds are widely distributed as intramolecular- or intermolecular bonds. One important example for intermolecular bonds is the base pairing in DNA or RNA of the Watson-Crick-type. In the latter, two hydrogen bonds are built between the adenine and thymine and three hydrogen bonds between guanine and cytosine bases. Thus, hydrogen bonds are the basis for sequence specific hybridization of nucleic acid strands, which is the basis of life. Intramolecular hydrogen bonds are formed between hydrogen bond-donor and -acceptor groups in the same molecule. The energy of the hydrogen bonds strongly depends on the conformation, given by the angle and the distance between the functional groups. Even slight changes in the conformation reduce the energy drastically. [70]

The basis of **van der Waals interactions** is an unsymmetrical charge distribution of electron charges in atoms. Attractive forces act between two unsymmetrically charged atoms with an energy in the range of 0.5 – 4.5 kJ/mol. [71]

3.2 Atomic Force Microscopy

The Atomic Force Microscope (AFM) was developed in 1986 by G. Binnig, C. Quate and C. Gerber and opened the way for the investigation of intermolecular forces. Especially the forces, which act between molecular binding partners were accessible. [72]

The key-element of an AFM is the measuring probe. This probe consists on one site of a mountable chip and on the other site of a spring, called cantilever (Figure 3.2). The cantilever is equipped with a nanometer-sized tip, made by microfabrication technology. The deflection of the flexible cantilever is usually measured by the optical lever technique. The principle of this technique is the detection of the reflection of a laser beam from the metal-coated backside of the cantilever. The reflected laser beam is focused on a four-quadrant photodiode. [73] With the tip not in contact with the surface, the laser spot is focused on the center of the photodiode. Bending of the cantilever changes the position of the laser spot on the photodiode. Thus, depending on the position of the laser spot on the photodiode, a current of the photodiode is measured. This current is converted into a voltage. This optical lever technique requires a well aligned laser and photodiode for a precise detection. The

photodiode consists of four quadrants, which allow the detection of cantilever bending and torsion in both vertical and lateral directions. [74]

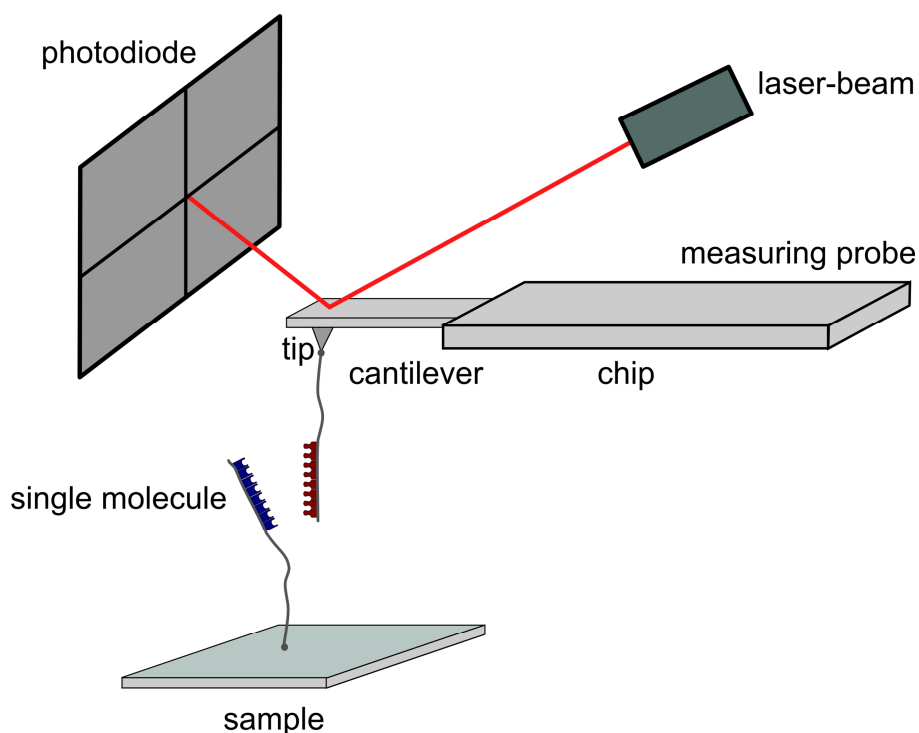


Figure 3.2: Working principle of an AFM in the single-molecule force spectroscopy mode. The measuring probe consists of a cantilever with a tip, which is mounted on a chip. For the readout of tip-sample interactions, a laser beam is aligned on the metal coated backside of the cantilever. Bending of the cantilever is detected by a deflection of the laser beam on the photodiode (optical lever principal). Single molecules can be attached to the tip and the sample, respectively.

3.2.1 Contact Mode

In a contact mode measurement, the tip and the sample surface are usually in direct contact with each other. This mode is applied to image the sample surface by raster scanning. The attractive and repulsive forces that are acting between the tip and the sample can be described by the Lennard-Jones potential $U(r_{LJ})$.

$$U(r_{LJ}) = 4\epsilon_{LJ} \left[\left(\frac{\sigma}{r_{LJ}} \right)^{12} - \left(\frac{\sigma}{r_{LJ}} \right)^6 \right] \quad (3.2)$$

with the depth of the potential well (ϵ_{LJ}) and the distance between the tip and the sample (r_{LJ}). At the finite distance σ , the Lennard-Jones potential is zero (Figure 3.3). The first term describes repulsive interactions, caused by ionic- or Pauli-repulsion. These interactions are short ranged, because they arise from overlapping electron orbitals of the involved atoms. The second term describes long range attractive interactions. This effect is caused by van der Waals forces. The contact mode is performed in the repulsive regime. [75]

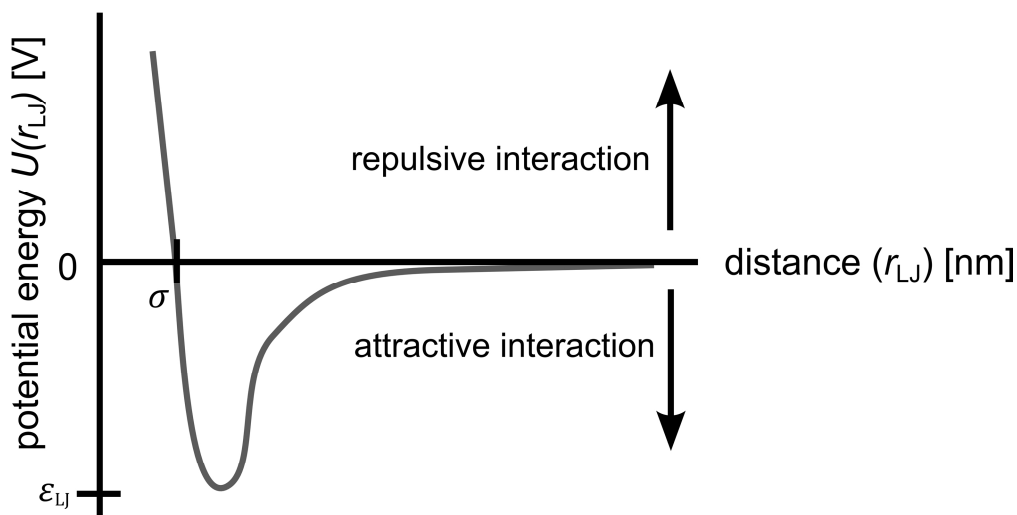


Figure 3.3: Schematic illustration of the Lennard-Jones potential as interaction between a tip and a sample. The potential energy versus the tip-sample distance (r_{LJ}) is plotted.

The force (F), acting between a tip and a sample surface, can be calculated by Hook's law:

$$F = k_{\text{cant}} \Delta z_c \quad (3.3)$$

with the spring constant (k_{cant}) and the deflection of the cantilever (Δz_c).

3.2.2 Spring Constant Calibration

The determination of the spring constant is important for the reliable evaluation of force-distance curves. Hutter and Bechhoefer introduced the so-called ‘‘Thermal-Noise-Method’’, which is implemented in many AFM. This method is based on the equipartition theorem, which provides the relation between the thermal noise of the cantilever deflection signal and the spring constant of the cantilever. [76] A freely oscillating cantilever is necessary, with no attractive or repulsive forces acting between the tip and the sample. The cantilever can be considered as harmonic oscillator at small thermal oscillation amplitudes. [77] The following equations describe the mean square deflection caused by thermal fluctuations of the cantilever:

$$\frac{1}{2} k_{\text{cant}} \langle z_c^2 \rangle = \frac{1}{2} k_B T \quad (3.4)$$

$$k_{\text{cant}} = \frac{k_B T}{\langle z_c^2 \rangle} \quad (3.5)$$

with the Boltzmann constant (k_B), the temperature (T) and the mean square displacement of the cantilever, caused by thermal fluctuation $\langle z_c^2 \rangle$. The latter is determined by recording the cantilever deflection in buffer and followed by a power spectral density analysis, which is given by the Fourier

transformation of the plot z_c^2 versus the frequency. The integral of the power spectrum ($P(\nu)$) provides the total value of $\langle z_c^2 \rangle$. [78]

$$\langle z_c^2 \rangle = \int_0^\infty P(\nu) d\nu = \frac{k_B T}{k_{\text{cant}}} \quad (3.6)$$

The power spectrum follows the response function of a simple harmonic oscillator, because the thermal excitation acts as white noise. A Lorentz curve can be applied to calculate the area underneath the peak, which is typically used to calculate the spring constant. [79]

The cantilever is not an ideal harmonic oscillator, because different vibration-modes with the mean thermal energy $k_B T/2$ are present. By fitting just the first oscillation mode, the spring constant is overestimated. Measurements are frequently carried out in liquid, where the resonance frequency is decreased. The optical lever technique is used to detect the inclination of the cantilever, which is proportional to the deflection of the cantilever. The proportionality depends, whether the cantilever is in contact with the surface. Thus, for V-shaped cantilever, the determined spring constant is usually multiplied with a correction factor of 0.78. [59, 80, 81] The error of the calculated spring constant with the thermal calibration method is approximately 10 - 20%. [77, 82, 83]

3.3 Measuring-Mode – Force Spectroscopy

Single-molecular force spectroscopy (SMFS) is a specific application of the AFM, which allows the determination of forces between single molecules. [32, 84, 85] In SMFS, the cantilever tip approaches the surface in z-direction with a defined speed, until a predefined cantilever deflection is reached (z-point). The cantilever tip is subsequently withdrawn from the surface, till a predefined distance between the tip and the sample is reached. Thus, in this measuring mode the contact times between tip and sample can be adjusted. The readout of one approach- and retraction-cycle is the photodiode signal versus the z-piezo-position (Figure 3.4).

In the initial position, the tip is not in contact with the surface (Figure 3.4-1). Due to the distance between the tip and the sample, no attractive or repulsive forces act between the surfaces. Thus, the cantilever is not bent. As the tip approaches the surface, attractive forces cause the cantilever to bend towards the sample. A “jump-into contact” is observed as soon as the gradient of the surface forces exceeds the spring constant (Figure 3.4-2). Assuming a hard surface, the characteristic linear regime of the cantilever deflection reveals the constant compliance region (Figure 3.4-3). The approach ends as soon as the z-point is reached. At the end of the constant compliance region of the retraction, unspecific adhesion forces can keep the tip in contact with the sample (Figure 3.4-4). Once the pulling forces exceed the adhesion forces, the tip retracts from the sample.

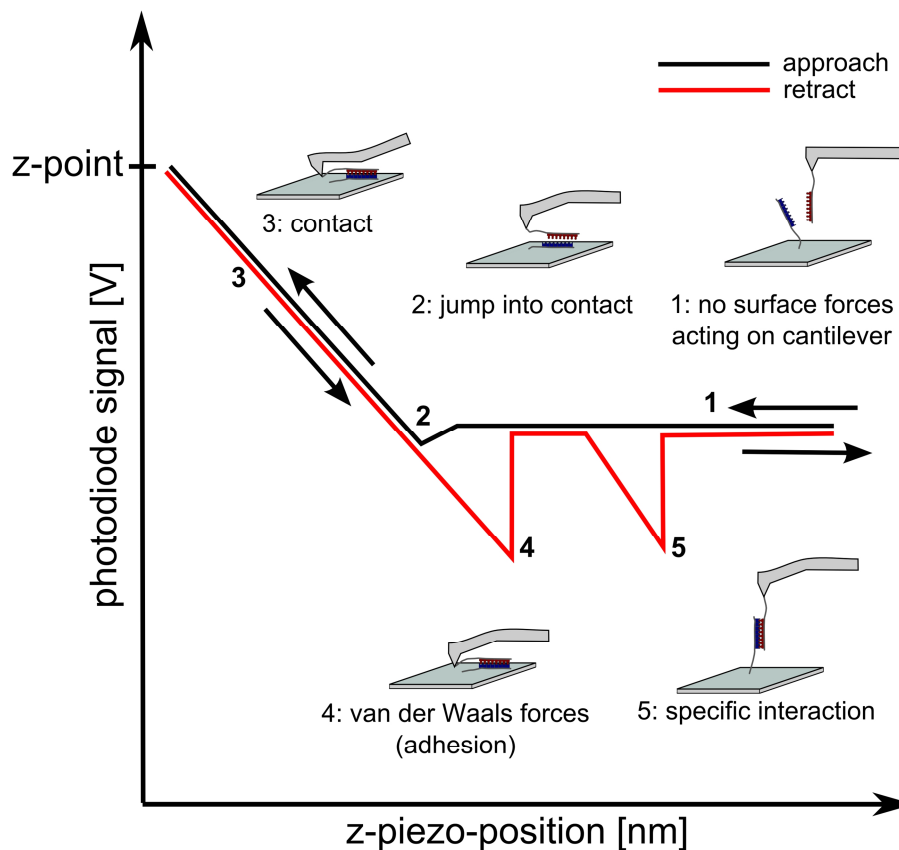


Figure 3.4: Schematic of an approach- (black line) and retract-cycle (red line). The photodiode signal in Volt is plotted against the position of the z-piezo. The different stages of a typical cycle are highlighted. 1) In the “zero force regime”, no forces are acting between tip and sample. 2) Attractive forces may cause a jump into contact. 3) In the constant compliance region, the tip and the sample are in contact. 4) Van der Waals forces may lead to an adhesion between the tip and the sample. 5) In the case, the tip and the sample are functionalized with single-molecules, specific rupture-events are observable.

In the case of binding partners, immobilized on the tip and the surface, their intermolecular interaction can be investigated. Subsequent stretching of bound molecules induces a tension of the non-covalent bindings until the force reaches a threshold. The rupture of the bindings occurs, when the pulling force overcomes the sum of the intermolecular forces between the binding partners (Figure 3.4-5). These rupture forces are characteristic for the investigated molecules and usually cover a range from less than 5 pN to the nN regime. To achieve this force-resolution, typically cantilevers with spring constants between 0.01 and 0.5 N/m are used.

3.3.1 Conversion into Force-Distance Curve

In order to determine intermolecular forces, the photodiode-signal has to be converted into a force and the z-piezo-position into the distance between the tip and the sample (Figure 3.5). Here the calculation for infinitely hard materials is presented, because for this work a glass substrate and a silicon nitride tip were used.

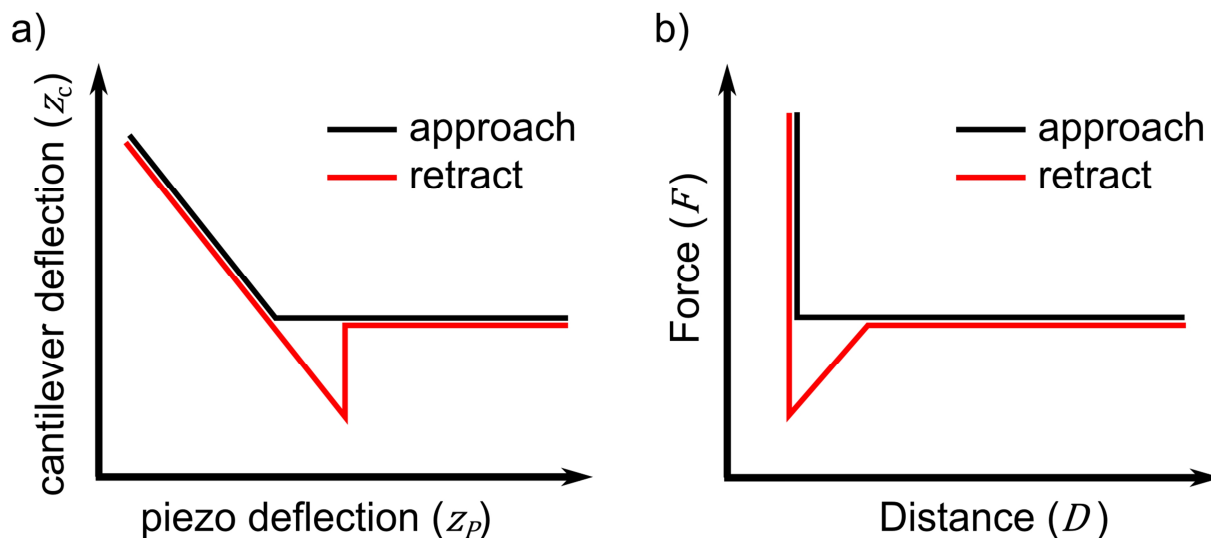


Figure 3.5: Schematic of the conversion into a force-distance curve (F-D curve) for an infinitely hard material. a) The cantilever deflection is plotted against the piezo displacement. b) A conversion into a force-distance curve is calculated by applying the equations 3.7 to 3.9.

In the “non-contact” regime, no cantilever deflection is present (Figure 3.4-1). The slope of the linear part of the constant compliance region is the sensitivity (α_s) (Figure 3.4-3):

$$\alpha_s = \frac{\Delta U}{\Delta z_p} \quad (3.7)$$

with the photodiode-voltage (U) and the z -piezo-position (z_p). The cantilever-deflection (z_c) is calculated from the photodiode-voltage signal (U) and the sensitivity:

$$z_c = \frac{U}{\alpha_s} \quad (3.8)$$

Hook’s law (equation 3.3) can then be applied to calculate the force. The true distance (D) between tip and sample is calculated by the addition of the deformation of the piezo actuator with the cantilever deflection.

$$D = z_c + z_p \quad (3.9)$$

The zero position is given by the intersection point of the linear regimes of the force distance curve. The force can be calculated for a known spring constant and sensitivity. [77] The calculated force can differ from the real force value due to the error of the spring constant and the sensitivity. An increase in the spring constant by 20 % results in a 20 % larger force. The sensitivity has the same effect on the calculated force. In contrast to that, is the rupture distance just changed by only 2 % for an increase in the spring constant of 20 %. The same accounts for the sensitivity.

3.3.2 Functionalization of Tip- and Sample-Surface

The use of functionalized tips and samples allows insights into the intermolecular forces between the binding partners. One molecular partner is immobilized on the cantilever-tip and its counterpart on the sample surface (Figure 3.6). Important for the investigation of binding partners, is a covalent connection between the molecules of interest to the tip- and sample-surface. This connection has to be stronger than the sum of the forces between the binding partners. The force, needed to rupture a covalent bond is in the range of 1 - 2 nN. [86] Usually the surfaces are functionalized with linker molecules, which allow an oriented connection to the molecule of interest. There are two advantages arising from the use of linkers: (i) an unhindered complex-formation and (ii) a complex-rupture, which is distinguishable from adhesion events. Polyethylene glycol (PEG) spacers, which carry a maleimide-group on one side of the chain and a NHS-group (*N*-Hydroxysuccinimide) on the other side, are suitable linker molecules (Figure 3.6). [87] In this work, the thiol-modified RNA is connected to the maleimide-group of the linker (smaller inset in Figure 3.6). The cantilever tip was modified with APTES (3-Triethoxysilylpropylamine) to generate primary amines (-NH₂) as anchor groups on the surface. In the reaction of a primary amine with the linker-molecule, the NHS-group was released and a covalent bond was built (upper inset in Figure 3.6).

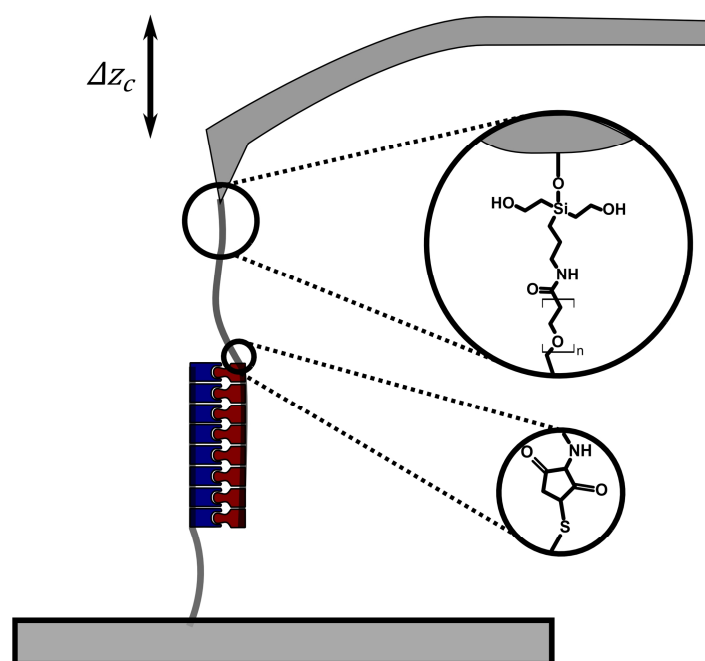


Figure 3.6: Schematic of functionalized tip- and sample-surface. The inset highlights the covalent connections to the tip and the single-molecule (RNA) via a PEG-linker.

The presented immobilization chemistry has the advantage that the grafting density can be minimized. The polymer-linkers increase the flexibility of the single molecules, which improves the binding-process. Ideally, only one pair of binding partners forms during one approach- and retract-cycle, which is facilitated by a low number of immobilized single-molecules. In order to improve the

performance of SMFS experiments, short contact times (< 400 ms) and low contact forces (< 300 pN) between the tip and the sample are desired. Ideally the number of specific binding events is below 10 %. The probability for the formation of one pair of binding partners follows the Poisson statistics according to the following equation:

$$P\left(N_b = \frac{1}{N_b} > 0\right) = \frac{\lambda_f}{\exp(\lambda_f) - 1} \quad (3.10)$$

with the number of bonds (N_b) and the frequency of binding events (λ_f). Assuming that less than 30 % of the recorded F-D curves contain one rupture event, the probability of observing the rupture between one pair of binding partners is ≈ 86 %. [88]

3.3.3 Effective Spring Constant

The rupture force (F) and the rupture distance (D) are obtained from the last force-jump of the retraction curve (Figure 3.7). Due to the flexible polymer linker, the effective spring constant is lower than the spring constant of the cantilever. The PEG-linker molecules, e.g. with a molecular weight of 5000 g/mol, consist of 130 ± 20 units. [89] Under the applied load, the PEG-linker molecule straightens from a random configuration to a stretched molecule. For the evaluation of PEG-stretching, the Freely-Jointed chain (FJC) extension model is often applied. The stretching process is described by an extended Langevin function:

$$x(F) = L \left[\coth\left(\frac{Fl_K}{k_B T}\right) - \frac{k_B T}{Fl_K} \right] \quad (3.11)$$

with the end-to-end distance (x), the force (F) the chain link size (l_K), the contour length ($L = n l_K$), the number of units (n), the temperature (T) and the Boltzmann-constant (k_B).

The effective spring constant (k_{eff}) of the cantilever linker system is estimated from the slope before the force-jump. [65] Depending on the amount of data points, which are used for the calculation of the slope, different effective spring constants are calculated (Figure 3.7). Thus, I estimated the corresponding error to be up to 30%. The effective spring constant is the combination of the cantilever-spring constant (k_{cant}) and the PEG-linker spring constant (k_L). [90]

$$k_{\text{eff}} = \frac{k_{\text{cant}} k_L}{k_{\text{cant}} + k_L} \quad (3.12)$$

Exemplarily, I calculated the effective spring constant for a system consisting of cantilever, PEG-linker and complementary RNA strands. The combination of $k_{\text{cant}} = 10$ pN/nm and $k_L = 3$ pN/nm resulted in an effective spring constant of $k_{\text{eff}} = 2.3$ pN/nm.

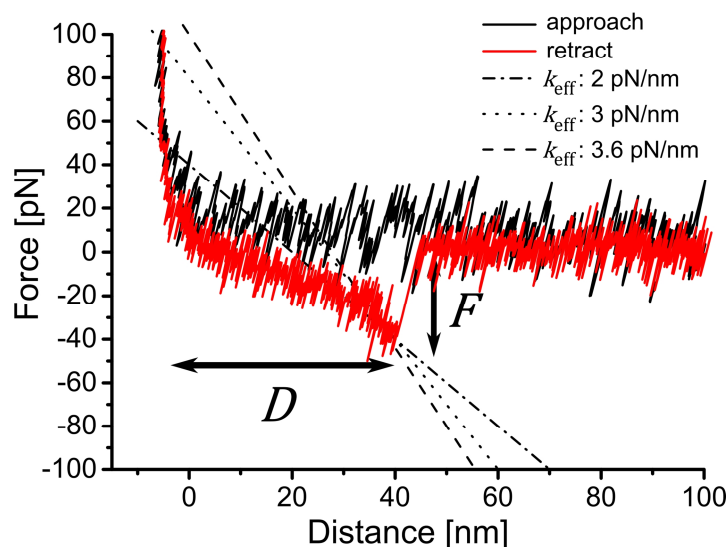


Figure 3.7: Exemplary F-D curve. The rupture distance (D) and the rupture force (F) are indicated. The effective spring constant (k_{eff}) of the cantilever linker system is estimated from the slope before the force-jump.

3.4 Theory of Force Spectroscopy

The separation of binding partners is a thermally driven process that follows a system-specific energy landscape (blue line Figure 3.8) and requires a certain amount of energy (ΔG_0) to overcome the energy barrier. The distance between the energy minimum and the energy barrier is referred to as the potential width x_β , which is a characteristic length of the investigated system. [31-33] The separation of the binding partners is described by the off-rate (k_{off}) and the rebinding process by the on-rate (k_{on}), respectively. Typical off-rates range between 10^1 and 10^{-7} s^{-1} . The corresponding on-rates range between 10^1 to $10^{10} \text{ M}^{-1}\text{s}^{-1}$. [91] Consequently the rebinding process (described by the on-rate) is typically much faster. To determine k_{off} , it is necessary to prevent the rebinding process efficiently. The benefit of the force spectroscopy technique is the effective separation of binding partners, which prevents the rebinding process. In the following, the theory of the effect of an applied force field on the energy landscape is described. The aim is to extrapolate the equilibrium parameter k_{off} and x_β by probing the binding partner out of equilibrium.

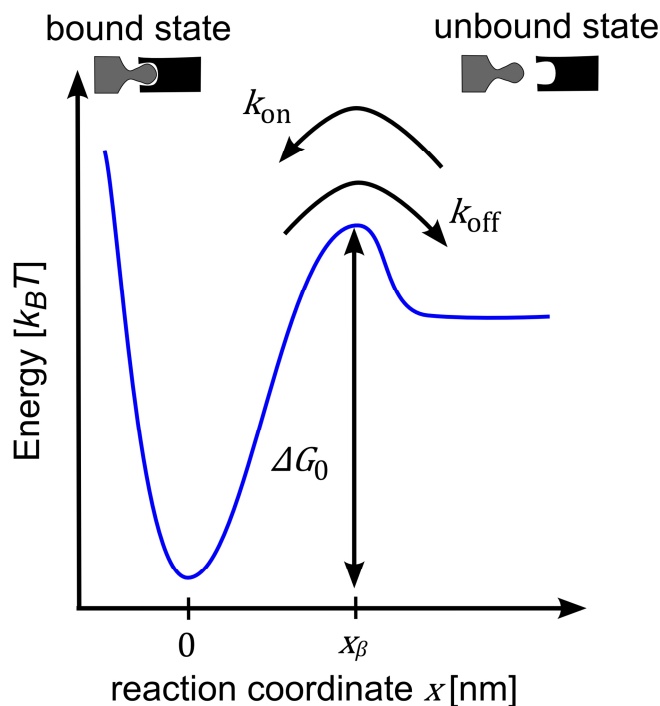


Figure 3.8: Schematic representation of the dissociation/ association process of binding partners. The potential barrier (height: ΔG_0 and width: x_β) has to be overcome to separate the binding partners. The dissociation of the complex is described by the natural off-rate (k_{off}) and the association by the on-rate (k_{on}).

Different models have been applied for the analysis of single-molecule force spectroscopy data. The foundation of all theories was established by Eyring [92, 93] using an Arrhenius-like model to describe the relaxation of polymers under stress. At the same time Kramer [94] approached the topic of calculating the rate of chemical reactions by observing the escape of a bond over a potential barrier. Initially located in a local free energy minimum, the energy barrier may be overcome by thermal fluctuations (Brownian motion) on a certain timescale. Based on the theory of stochastic processes, Bell [95] and Evans [96, 97] were able to analyze the behavior of single molecules between cells under applied load. They described the bond rupture as thermally driven separation that depends on the applied load. This so called phenomenological model takes a single energy barrier into account. The crossing over this barrier is valid for small forces. The reaction distance x_β is assumed to stay fixed under the external force. [98]

3.4.1 Bimolecular Systems

The purpose of the previously introduced models is to understand the interaction between two binding partners. The interaction of binding partner A with binding partner B leads to the formation of a complex AB .



The equilibrium constant k_{on} describes the formation of the complex, whereas k_{off} describes the separation of the complex. The time dependent thermal equilibrium is reached, when the molar concentrations of the binding partners do not change:

$$\frac{d[AB]}{dt} = [A][B]k_{\text{on}} - [AB]k_{\text{off}} = 0 \quad (3.14)$$

The terms in brackets present the molar concentration of the binding partners $[A]$ and $[B]$ and their complex $[AB]$. K_d is the equilibrium constant that provides the concentration at which half of the complexes are dissociated:

$$K_d = \frac{k_{\text{off}}}{k_{\text{on}}} = \frac{[A][B]}{[AB]} \quad (3.15)$$

To visualize K_d , the fraction of bound binding partner B (θ_B) is plotted versus the concentration of free binding partner A ($[A]$).

$$\theta_B = \frac{[AB]}{[B] + [AB]} = \frac{1}{\frac{[B]}{[AB]} + 1} = \frac{1}{\frac{K_d}{[A]} + 1} = \frac{[A]}{K_d + [A]} \quad (3.16)$$

For $[A] = K_d$, the fraction of bound binding partner B (θ_B) is 0.5. Consequently one can directly relate the value for K_d in a binding curve, as the concentration of binding partner A at the half maximum fraction of bound B (Figure 3.9).

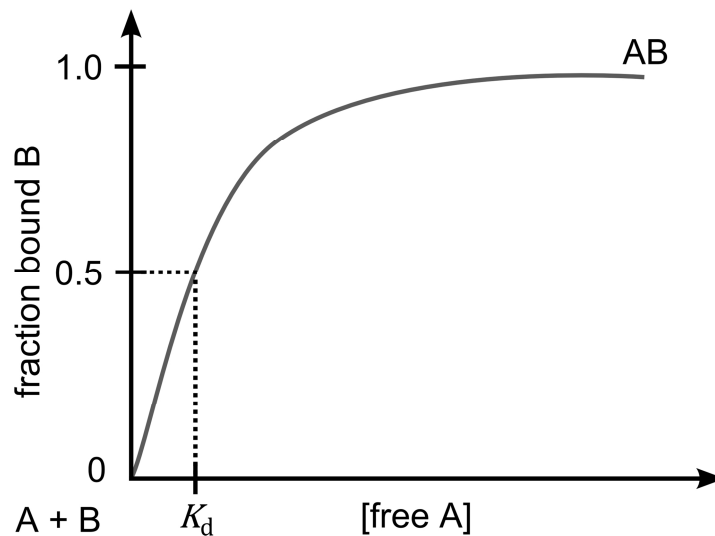


Figure 3.9: This binding curve represents the fraction of bound binding partner B versus the concentration of free binding partner A. The K_d is defined as half maximum value.

3.4.2 The Bell-Model

In the following the Bell-model is derived according to literature. [91] The Bell-model describes the influence of an external pulling potential on a bond between two binding partners. The external force is usually generated by a withdrawn spring (here the cantilever), which can be described by a parabolic potential:

$$V(x, x_{\text{cant}}) = \frac{1}{2} k_{\text{cant}} (x - x_{\text{cant}})^2 \quad (3.17)$$

x_{cant} is the distance from the bond minimum to the external potential minimum. The binding partners are assumed to be bound at the position $x = 0$. According to Hook's law, the pulling potential, acting on the bound state, can be written as:

$$V(x, F) = \frac{1}{2} k_{\text{cant}} \left(x - \frac{F}{k_{\text{cant}}} \right)^2 \quad (3.18)$$

$$V(x, F) = \frac{F^2}{2k_{\text{cant}}} - Fx + \frac{1}{2} k_{\text{cant}} x^2 \quad (3.19)$$

During the approach and retraction cycle, the pulling potential covers a large distance of x . In order to understand the rupture process, the distance between the local minimum ($x = 0$) and the energy barrier (x_{β}) is essential (Figure 3.10). Assuming a sharp energy barrier (= small x_{β}), only a small tangential part of the pulling potential has to be taken into account. The energy of the bound state increases relative to the pulling potential, as described by the term $F^2/2k_{\text{cant}}$. The potential gradient $-F$ along the reaction coordinate x is the second term (height difference between blue and red line in Figure 3.10). The last term describes a small nonlinear contribution ($0.5 k_{\text{cant}} x^2$). The resulting height of the energy barrier under the influence of the pulling potential is:

$$\Delta G(F) = G(x_{\beta}) + V(x_{\beta}, F) - [G(0) + V(0, F)] \quad (3.20)$$

after inserting equation 3.19 it follows:

$$\Delta G(F) = \Delta G_0 - Fx_{\beta} + \frac{1}{2} k_{\text{cant}} x_{\beta}^2 \quad (3.21)$$

The combination of the Arrhenius escape rate (3.22) and the linear term (3.21) provides the transition rate under force:

$$k(F) = A \exp \left[\frac{-\Delta G(F)}{k_{\text{B}}T} \right] \quad (3.22)$$

$$k(F) = k^0 \exp \left[\frac{Fx_{\beta} - \frac{1}{2} k_{\text{cant}} x_{\beta}^2}{k_{\text{B}}T} \right] \quad (3.23)$$

The transition rate, reported by Bell, excludes the term $\frac{1}{2}k_{\text{cant}}x_{\beta}^2$. This term is neglectable for soft springs and small x_{β} (i.e. deflections) (Figure 3.10). [91]

$$k(F) = k^0 \exp\left[\frac{Fx_{\beta}}{k_{\text{B}}T}\right] \quad (3.24)$$

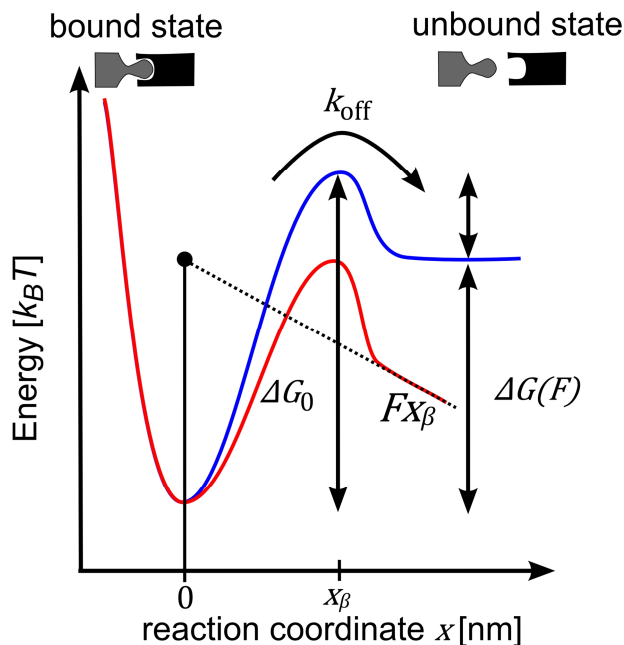


Figure 3.10: Schematic representation of the influence of an external force on the dissociation process of binding partners. The potential barrier (ΔG_0) is lowered by Fx_{β} due to the applied force. The dissociation of the complex is described by the natural off-rate (k_{off}) and the height of the resulting energy barrier is ($\Delta G_0(F)$).

3.4.2.1 Force Ramp Bond Rupture

The separation process of two binding partners, here referred to as A and B , has at least two states: The initial bound state and the dissociated final state. This Markovian two-state process with time-dependent unbinding ($k_{\text{off}}(t)$) and binding ($k_{\text{on}}(t)$) rates is given by:

$$\frac{d}{dt}p_{\text{on}}(t) = -k_{\text{off}}(t)p_{\text{on}}(t) + k_{\text{on}}(t)p_{\text{off}}(t) \quad (3.25)$$

$$\frac{d}{dt}p_{\text{off}}(t) = k_{\text{off}}(t)p_{\text{on}}(t) - k_{\text{on}}(t)p_{\text{off}}(t) \quad (3.26)$$

The probability to find the system in a bound- or unbound state at the time (t) is given by $p_{\text{on}}(t)$ and $p_{\text{off}}(t)$. At the beginning, A and B are in the bound state, which can be described with the initial conditions:

$$p_{\text{on}}(0) = 1, p_{\text{off}}(0) = 0 \quad (3.27)$$

$$p_{\text{on}}(t) + p_{\text{off}}(t) = 1 \quad (3.28)$$

3.4.2.2 First-Passage Approximation

With an external pulling potential applied on the bond, the force increases with time until the bond breaks. Rebinding of the bond becomes more unlikely the higher the force gets. Large forces are reached quickly due to the fast constant separation of tip and sample. Consequently the equation 3.25 can be simplified to: [91]

$$\frac{d}{dt}p_{\text{on}}(t) = -k_{\text{off}}(t)p_{\text{on}}(t) \quad (3.29)$$

At the beginning of the experiment, A and B are bound and the population is given by $p_{\text{on}}(0) = 1$. In AFM based force spectroscopy measurements, not the time until rupture, but the rupture force is measured. Thus, to calculate the remaining force at a force (F), a substitution has to be proceeded from time to force ($(1/r_f)dF = dt$). With the loading rate (r_f), which is given by the multiplication of the spring constant, times the retract velocity.

$$\int_1^{p_{\text{on}}} \frac{dp'_{\text{on}}}{p'_{\text{on}}} = -\frac{1}{r_f} \int_0^F k_{\text{off}}(F') dF' \quad (3.30)$$

The integration of the left side provides the probability of the binding partner, which remain in the bound state.

$$p_{\text{on}}(F) = -\frac{1}{r_f} \int_0^F k_{\text{off}}(F') dF' \quad (3.31)$$

3.4.2.3 Distribution

The probability density of the first passage forces is given by:

$$\rho_{\text{fp}}(F) = \frac{1}{r_f} k(F) p_{\text{on}}(F) = \frac{1}{r_f} k(F) \exp \left[-\frac{1}{r_f} \int_0^F k(F') dF' \right] \quad (3.32)$$

At the initial position, the binding partner A and B are bound. In that moment, no force is acting on the bond ($F = 0$). Thus, the probability ($p_{\text{on}}(0)$) to find the binding partner A and B in the bound state is 1 and the density of transition times ($\rho_{\text{fp}}(0)$) is equivalent to the kinetic transition rate ($k_{\text{off}}(0)$). By increasing the force, the probability to find A and B in the bound state, decreases. The probability density function of the first-passage rupture forces was described by Evans and Ritchie:

$$\rho_{\text{fp}}(F) = \frac{1}{r_f} k(F) \exp \left[-\frac{k_{\text{B}}T}{r_f x_{\beta}} (k(F) - k(0)) \right] \quad (3.33)$$

The final probability density function is obtained by replacing the unbinding transition rate ($k(F)$) according to equation 3.24:

$$\rho_{\text{fp}}(F) = \frac{k_{\text{off}}}{r_f} \exp \left[\frac{Fx_\beta}{k_B T} - \frac{k_B T k_{\text{off}}}{r_f x_\beta} \left(\exp \left(\frac{Fx_\beta}{k_B T} \right) - 1 \right) \right] \quad (3.34)$$

The maximum value of $\rho_{\text{fp}}(F)$ corresponds to the most probable rupture force (F^*), which induces a rupture event. The unbinding transition rate ($k(F)$) is independent from the loading rate. This means that the unbinding transition rate only depends on the force and not on the history of the force with time. To get the frequency of rupture events, the unbinding transition rate ($k(F)$) has to be scaled by the probability ($p_{\text{on}}(F)$). This probability indicates, whether the formation of a bond between the binding partners at force F is still likely. The amount of the time, necessary to reach the rupture force, is given by F/r_f . This means that the probability depends on the loading-rate. The conversion of the first order rate process into a force related equation shows that the loading rate is inversely proportional to the probability of losing bound states. This relation explains why higher rupture forces are measured at higher loading rates.

$$\frac{dp_{\text{on}}(F)}{dF} = -\frac{1}{r_f} k_{\text{off}}(F) p_{\text{on}}(F) \quad (3.35)$$

By forming the derivation of $d\rho_{\text{fp}}(F^*)$ to dF , the expression for the most probable rupture force is given:

$$\begin{aligned} \frac{d\rho_{\text{fp}}(F^*)}{dF} &= 0 \\ 0 &= \frac{1}{r_f} \frac{dk(F)}{dF} \exp \left[-\frac{1}{r_f} \int_0^F k(F') dF' \right] - \frac{1}{r_f^2} k(F)^2 \exp \left[-\frac{1}{r_f} \int_0^F k(F') dF' \right] \\ \frac{1}{r_f} k(F) &= \frac{1}{k(F)} \frac{dk(F)}{dF} \\ k(F)|_{F^*} &= r_f \left. \frac{d \ln k(F)}{dF} \right|_{F^*} \\ F^* &= \frac{k_B T}{x_\beta} \ln \left(\frac{r_\beta x_0}{k^0 k_B T} \right) \end{aligned} \quad (3.36)$$

In order to determine the natural off-rate, the most probable rupture forces are plotted semi logarithmically versus the loading rate. The plotted most probable rupture forces increase proportionally to $\ln(r_f)$ and follow a linear dependency. This allows the application of the Bell-Evans model to calculate the natural off-rate (k_{off}) and the potential width (x_β) by using a linear fit ($F^* = a + \ln(r_f) \cdot b$). The potential width is given by $k_B T/b$ and the natural off-rate by $x_\beta e^{-a/b}/k_B T$. This calculation requires measurements at different pulling velocities, ranging from 50 nm/s to 2000 nm/s.

Thus, based on the Bell-Evans model, two different fitting routes can be used to calculate k_{off} and x_{β} (Figure 3.11):

- The probability density fit method, which is based on equation 3.34, provides k_{off} and x_{β} as fit parameters. [37] The rupture forces, collected during the measurement at one loading rate, are plotted in a histogram (Figure 3.11a). It is advantageous to apply this method, when the following circumstances reduce the possible number of measurements. Those circumstances are instable samples, which degrade fast. An additional advantage of this method is that the measurement can be performed at one rupture velocity.
- The linear Bell-Evans method is based on the measurement of rupture forces at different rupture velocities. The fit of the most probable rupture forces by means of equation 3.36 provides the k_{off} value (Figure 3.11b). This method is widely used in the field of single-molecule force spectroscopy analysis.

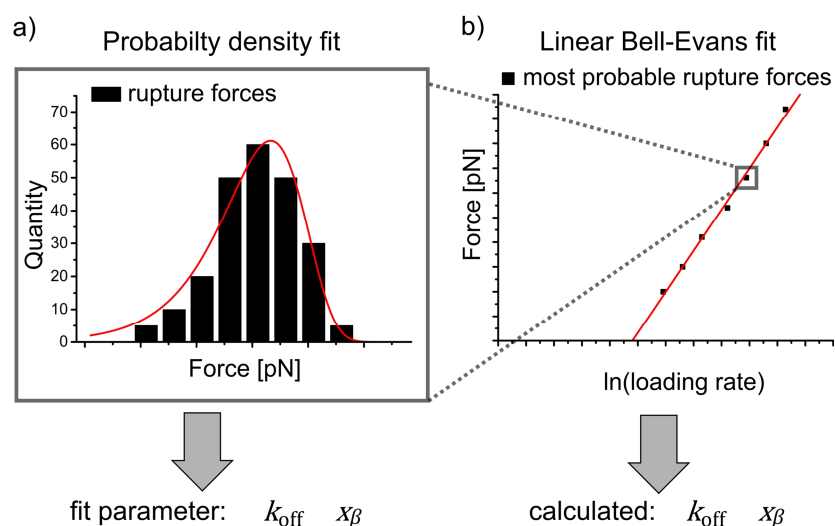


Figure 3.11: Schematic representation of the k_{off} and x_{β} calculation, which is derived from the Bell-Evans model. a) The histogram of rupture forces is fitted with the probability density function, using the fit parameter k_{off} and x_{β} . The maximum value of the probability fit is the most probable rupture force, which is used for the linear Bell-Evans fit. b) The most probable rupture forces are plotted against the logarithm of the loading rate. After calculations, k_{off} and x_{β} are received.

3.5 Motivation

In this chapter I will address the following questions: Where are the limitations of the probability density fit method? Which influence does the full width at half maximum (FWHM) of the fit function has on the fit parameters k_{off} and x_{β} ? How does k_{off} change in the case, the peak position (most probable rupture force) stays constant and the FWHM of the histogram is varied? The last question is particularly important, because many effects have an impact on the FWHM. Those effects will be addressed in this chapter.

3.6 Results and Discussion

As example, the dissociation of complementary RNA-strands (18 bp) is investigated. In general, RNA has been investigated only rarely by force spectroscopy techniques. One reason is RNA's susceptibility to ribonucleases, which lead to a degradation into smaller RNA components. Thus, the sample preparation has to be performed with caution to avoid contamination with ribonucleases.

3.6.1 How Does the FWHM Value Affect the Potential Width?

The FWHM of the probability density function (3.34) has a direct influence on k_{off} and x_{β} . One can correlate a larger FWHM of the probability function to a lower x_{β} value (Figure 3.12).

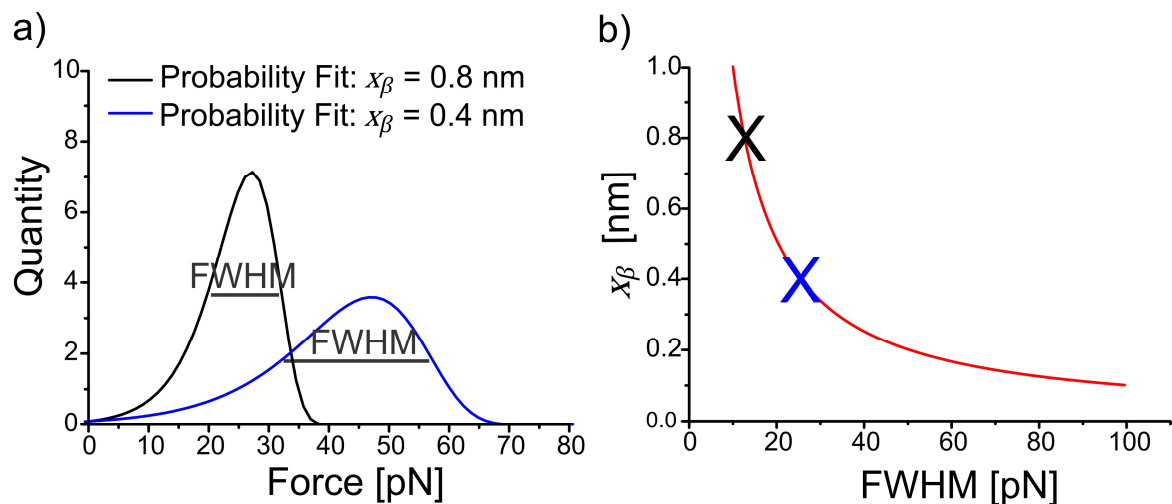


Figure 3.12: a) Two probability density functions at constant $k_{\text{off}} = 1 \text{ s}^{-1}$ and a loading rate of 980 pN/s. For x_{β} , the values 0.8 nm (black line) and 0.4 nm (blue line) were chosen. b) A plot of x_{β} versus the FWHM. The black and blue X indicates the corresponding data point to a).

As an example, two probability density functions at a constant loading rate of 980 pN/s and a constant k_{off} of 1 s^{-1} are plotted (Figure 3.12a). An increase of x_{β} from 0.4 nm to 0.8 nm leads to a decrease of the FWHM by $\approx 30 \%$ (Figure 3.12b). These probability fits also show that at a constant k_{off} and a lower x_{β} value, the most probable rupture force decreases. The most probable rupture forces of the

probability fits are ≈ 47 pN ($x_\beta = 0.4$ nm) and ≈ 26 pN ($x_\beta = 0.8$ nm). That gives rise to the question, how the FWHM correlates with k_{off} for constant most probable rupture forces.

3.6.2 Does the Off-Rate change with different FWHM-Values?

In order to obtain the effect of the FWHM on the fit parameter, the most probable rupture force (F^*) was kept constant and k_{off} and x_β were varied. This resulted in different shapes and width of the probability density function (Figure 3.13a). It can be observed that the probability fit for $k_{\text{off}} = 1$ s $^{-1}$ has a FWHM of ≈ 15 pN and the probability fit for $k_{\text{off}} = 3$ s $^{-1}$ has a FWHM of ≈ 20 pN. To compare the width of the probability fits, the full width at half maximum (FWHM) was calculated. Next the k_{off} values were plotted versus the FWHM for different most probable rupture forces (Figure 3.13b). This analysis revealed a significant increase in k_{off} with an increasing FWHM. For a most probable rupture force of 30 pN (blue triangles in Figure 3.13b), an increase in the FWHM from 15 pN to 20 pN resulted in a three-fold increase of k_{off} . An increase in the FWHM of 5 pN for a most probable rupture force of 50 pN (green squares in Figure 3.13b) led to an 1.5 fold increase in k_{off} . This calculation showed that the FWHM has a bigger influence on the determined k_{off} value for smaller most probable rupture forces.

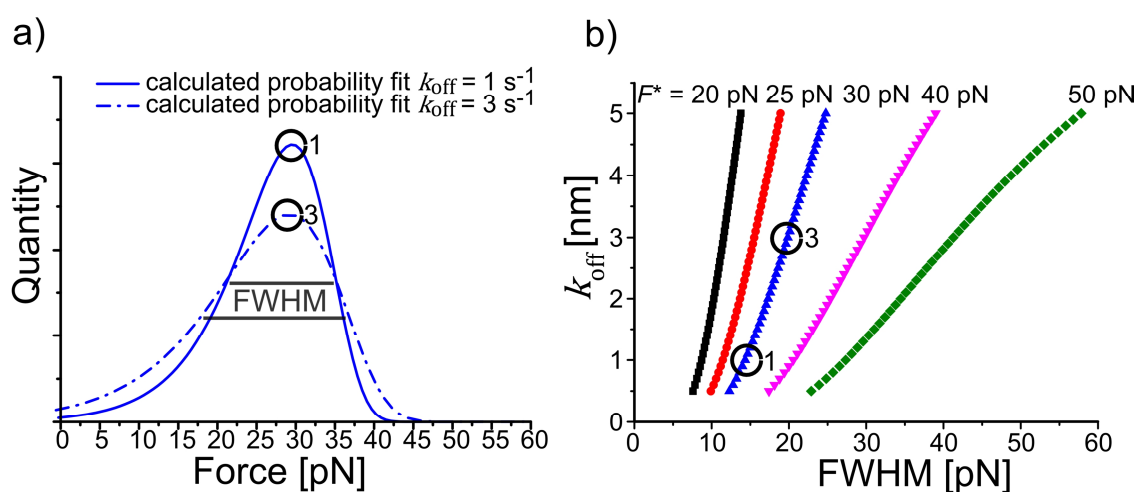


Figure 3.13: Effect of the probability function's FWHM on the k_{off} value. a) Calculated probability function for the same most probable rupture force and two different k_{off} (1 and 3 s $^{-1}$) with the corresponding x_β (0.72 and 0.53 nm). b) Dependency between the FWHM (x-axis) and k_{off} (y-axis) at a constant loading rate (980 pN/s) and different most probable rupture forces (black: 20 pN, red: 25 pN, blue: 30 pN, pink: 40 pN, green: 50 pN).

The effects, which can lead to an increase in the FWHM are roughly estimated in the following. The overlapping of single rupture events (e.g. $F^* = 30$ pN) with multiple rupture events (e.g. $F^* = 60$ pN) may increase the peak maximum of the probability fit. As an example, this value is estimated to be ≈ 40 pN. This would lead to an increase in the FWHM by a factor of ≈ 2 . The consequence would be a change of k_{off} from 1 s $^{-1}$ to 3 s $^{-1}$. Consequently the increase in FWHM and

the most probable rupture force would compensate to a certain degree the change of k_{off} . On the contrary x_{β} would decrease with increasing FWHM. In the cases of conformational changes within the molecule and rebinding of molecules, the most probable rupture force would probably remain almost constant. These effects might on the other site increase the FWHM, because more states of intermolecular interactions are possible at the time of rupture. An increase of the FWHM by a factor of ≈ 2 would increase k_{off} by a factor of ≈ 10 . The influence of the noise of the instrument has the opposite effect and occurs for low forces, which are in the range of the noise of the instrument. Thus, low forces are not detected and the FWHM of the distribution can be underestimated and consequently k_{off} appears smaller than it should be. In summary, the calculations demonstrate that the probability density method should be performed with caution in particular for small values of most probable rupture forces. On the contrary, this method can give reasonable k_{off} values for measurements of higher rupture forces. In the next section, the direct fit method is applied to data from SMFS measurements of complementary RNA.

3.6.3 Example – Complementary RNA

The tip was functionalized with 5'-thiolated RNA-oligonucleotides 5'-HS-gau ccg acc gug gug ccg-3' and the sample surface with the complementary RNA strands 5'-HS-cgg cac ggu cgg auc-3'. Hybridization between both RNA strands was achieved in buffer solution by bringing the tip in proximity to the sample surface. Upon subsequent retraction of the tip, the RNA-strands were separated and their rupture forces were measured. The thiol functionalization of the RNA-strands at the 5'-ends enabled measurements in shear-geometry, where the load is applied parallel to the RNA-backbone. Typically 10 – 15 % of the force-distance curves showed specific rupture events. The obtained rupture-forces were plotted in histograms at a bin size of 4 pN (Figure 3.14). The bin size corresponds to the value of the root mean square deviation of the baseline at a retract velocity of 50 nm/s (RMSD \approx 4 pN). The histograms represent probability distributions for the rupture events at a specific retract velocity (Figure 3.14). At the retract velocity of 50 nm/s, the peak maximum is located between 25 and 35 pN. It can be observed that the peak shifts to forces between 50 and 80 pN at higher retract velocities (1000 nm/s). The probability fit at the retract velocity 1000 nm/s is by a factor of ≈ 2 broader in comparison to the probability fit at a retract velocity of 50 nm/s.

The expected forces for the separation of the 18 bp RNA strands are in a force range of 20 – 40 pN. [39] The lower detection limit of rupture forces is given by the root mean square deviation of the force-distance curve (non-contact regime). Depending on the thermal noise of the cantilever and the detector, typical values between 3 and 7 pN are measured. The upper limit is in the range of several hundred nN.

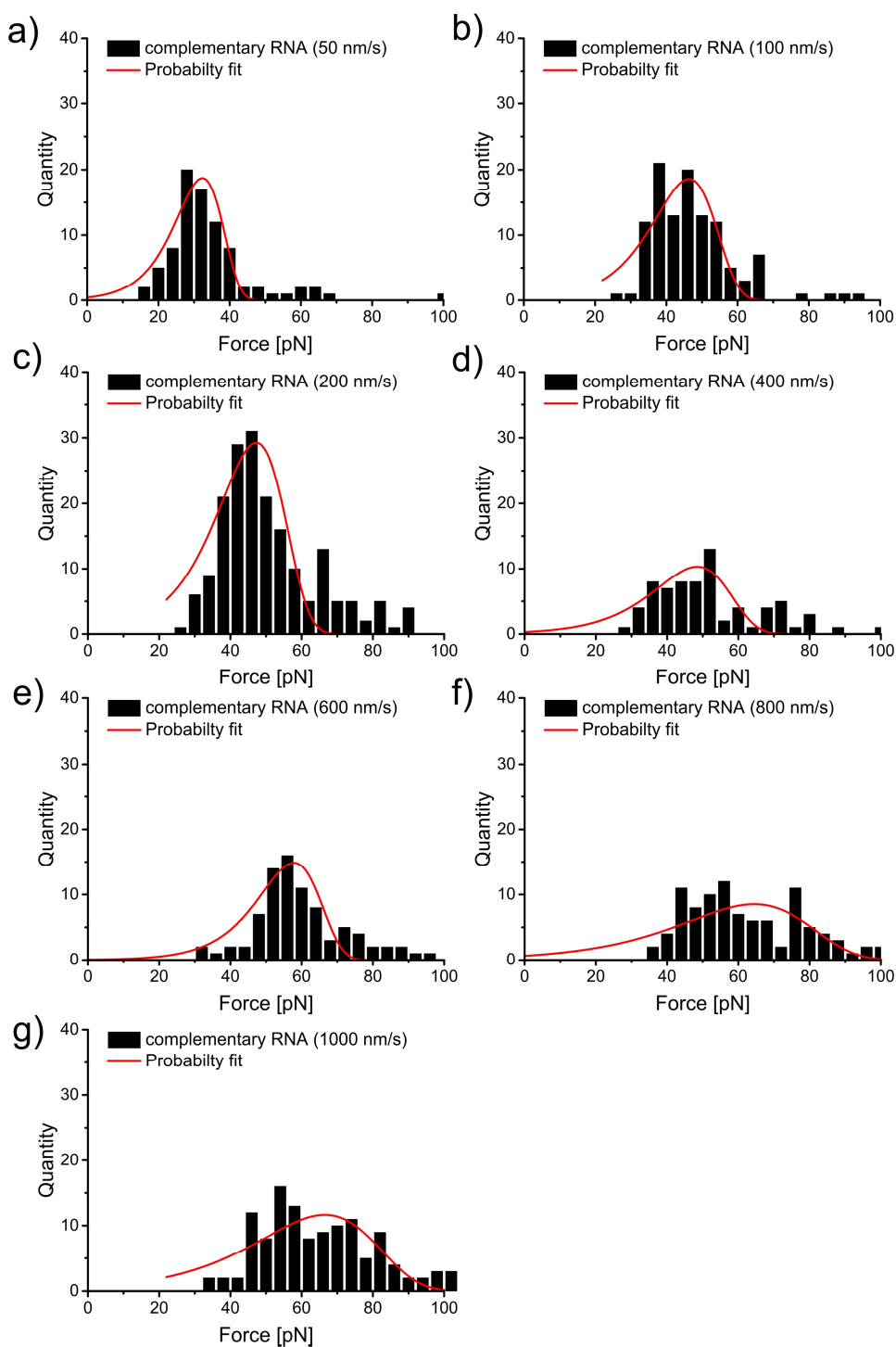


Figure 3.14: Histograms of rupture forces of complementary RNA-strands. Measurements at the following retract velocities were performed: 50 nm/s (a), 100 nm/s (b), 200 nm/s (c), 400 nm/s (d), 600 nm/s (e), 800 nm/s (f) and 1000 nm/s (g). A bin size of 4 pN was used. The probability function based on the Bell-Evans model (equation 3.34) was used to estimate the most probable rupture force of the histogram. The error value of the most probable rupture force was determined by the propagation of uncertainties for the fit-parameter k_{off} and χ_{β} .

The measurements were performed at the retract velocities (v) ranging from 50 nm/s to 1000 nm/s. The effective loading rate for one rupture event was calculated by multiplying the retract velocity (v) with the effective spring constant. To obtain the averaged effective loading rates (r_f), the natural

logarithm of the single effective loading rates were plotted in a histogram and fitted with a Gaussian fit (Figure 3.15).

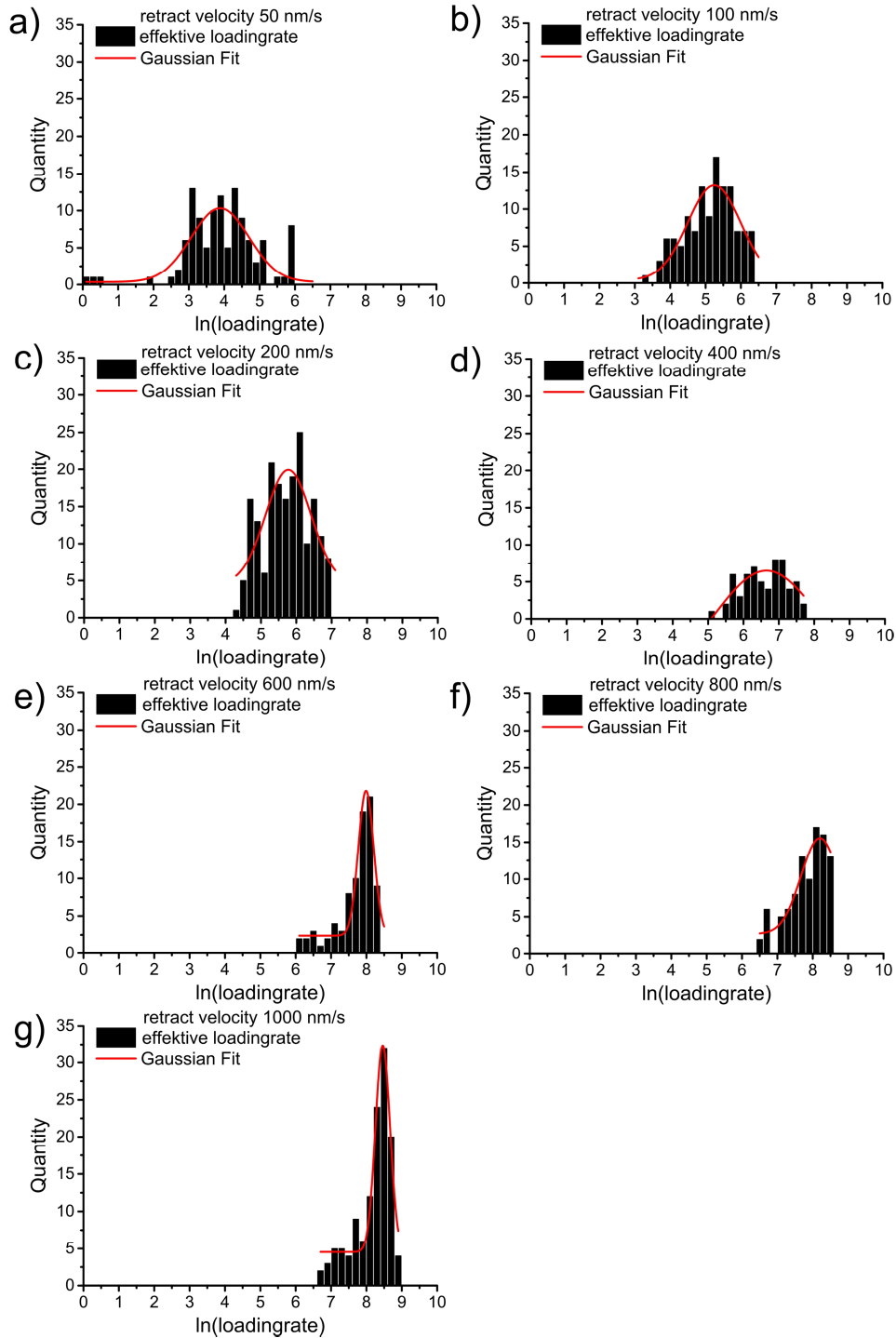


Figure 3.15: Histograms of the logarithm of the effective loading rates for the retract velocities, ranging from 50 nm/s to 1000 nm/s.

The distribution of the low to medium loading rates at 48.59 ± 2.63 pN/s (Figure 3.15a) to 773.30 ± 5.51 pN/s (Figure 3.15d) are similar in their FWHM and their symmetrical shape. The loading rates of 2945.95 ± 1.29 pN/s (Figure 3.15e) to 4726.73 ± 1.27 pN/s (Figure 3.15g) are narrower than the previously mentioned loading rates and unsymmetrical as presented in literature. [41]

Considering the effective loading rates, the values for k_{off} and x_{β} are provided as fit parameter (Table 3.1). At the loading rate of 48.59 ± 2.63 pN/s, a k_{off} value of 0.06 ± 0.01 s⁻¹ is determined. At the loading rate of 4726.73 ± 1.27 pN/s a k_{off} value of 5.44 ± 1.61 s⁻¹ is given. In contrast to that, x_{β} is decreased from 0.61 ± 0.03 nm to 0.25 ± 0.02 nm with increasing loading rate.

Table 3.1: Kinetic- and thermodynamic-parameter of the complementary RNA-strands derived by equation 3.34.

Retract velocity [nm/s]	Effective loading rate [pN/s]	k_{off} [1/s]	x_{β} [nm]
50	48.59 ± 2.63	0.06 ± 0.01	0.61 ± 0.03
100	189.55 ± 2.42	0.12 ± 0.07	0.46 ± 0.05
200	321.74 ± 2.14	0.24 ± 0.10	0.43 ± 0.04
400	773.30 ± 5.51	0.77 ± 0.28	0.39 ± 0.04
600	2945.95 ± 1.29	0.46 ± 0.19	0.47 ± 0.03
800	3647.21 ± 1.87	5.70 ± 1.78	0.23 ± 0.02
1000	4726.73 ± 1.27	5.44 ± 1.61	0.25 ± 0.02

In summary, the x_{β} values decrease and the k_{off} values increase with increasing retract velocity. This trend can be explained by the theoretical considerations, which were explained before. The FWHM has an influence on the calculated values x_{β} and k_{off} . The larger the FWHM, the lower is x_{β} and the higher is the calculated k_{off} value. In order to evaluate the results, the kinetic- and thermodynamic-parameter were calculated with the linear Bell-Evans fit. The most probable rupture forces were obtained, by fitting the histograms with the probability density function (Figure 3.14). The most probable rupture forces increase with the retract velocities. At a retract velocity of 400 nm/s, a most probable rupture force of 30.0 ± 2.0 pN is measured for example.

In order to determine the natural off-rate, the most probable rupture forces were plotted semi logarithmically versus the effective loading rate (Figure 3.16). As described earlier in theory, the most probable rupture forces increase proportionally to $\ln(r_f)$ and follow a linear dependency. By applying the Bell-Evans model, k_{off} and x_{β} were calculated to 0.054 ± 0.023 s⁻¹ and 0.68 ± 0.29 nm, respectively (black line in Figure 3.16). In literature, k_{off} values from 0.001 to 5 s⁻¹ have been reported for the rupture of 24 to 10 bp long oligonucleotides. [41-43]

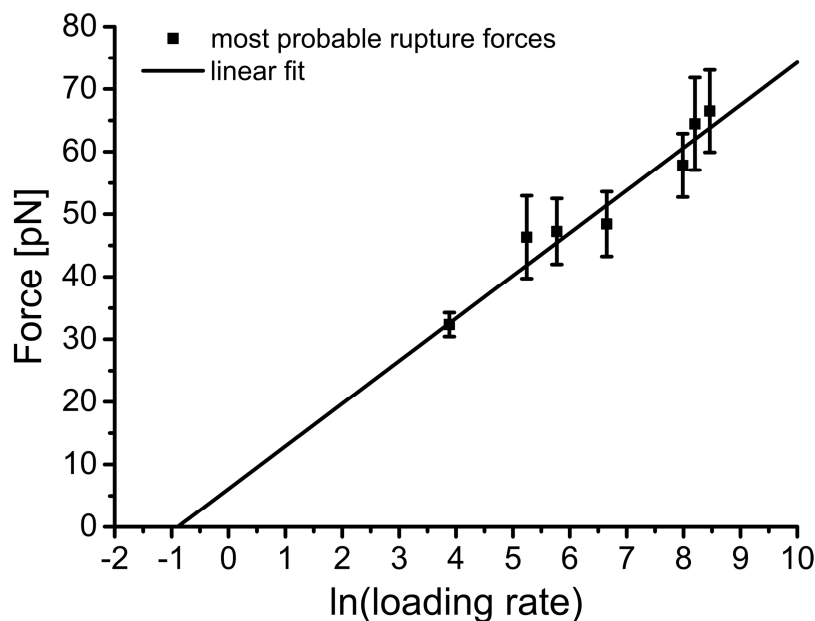


Figure 3.16: Most probable rupture forces, plotted as a function of the natural logarithm of the loading rate. The data points were fitted with a linear fit by means of equation 3.36. The underlying histograms, which were used to calculate the most probable rupture forces, are shown in Figure 3.14.

In the following, the percentage of agreement between the results of the probability density fit and the linear Bell-Evans fit are plotted against the effective loading rates (Figure 3.17). These percentages are calculated according to:

$$\left(100 (k_{\text{off-linear}} - k_{\text{off-prob}} / k_{\text{off-prob}})\right) + 100 \text{ and } \left(100 (x_{\beta\text{-prob}} - x_{\beta\text{-linear}} / x_{\beta\text{-linear}})\right) + 100$$

Only at the loading rate 48.59 ± 2.63 pN/s, there is an agreement of 90 % between the results of both methods for the k_{off} and x_{β} values. In general, the higher the loading rate, the lower the accordance between the results of both methods. Especially at the loading rates 3647.21 ± 1.87 pN/s and 4726.73 ± 1.27 pN/s, the agreement for the k_{off} and x_{β} is 1 % and 37 %, respectively. The convergence of the values, derived by the probability fit and the linear Bell-Evans fit, is just given in the cases, where both values match. The deviation of one value results in the deviation of the other. This can be explained by the fact that in the linear Bell-Evans fit only one x_{β} value is determined. The probability density fit method provides in contrast to that x_{β} values for every loading rate (Table 3.1). These x_{β} values are strongly correlated with the FWHM of the probability density functions. Thus, similar k_{off} values are found for the cases with similar x_{β} values.

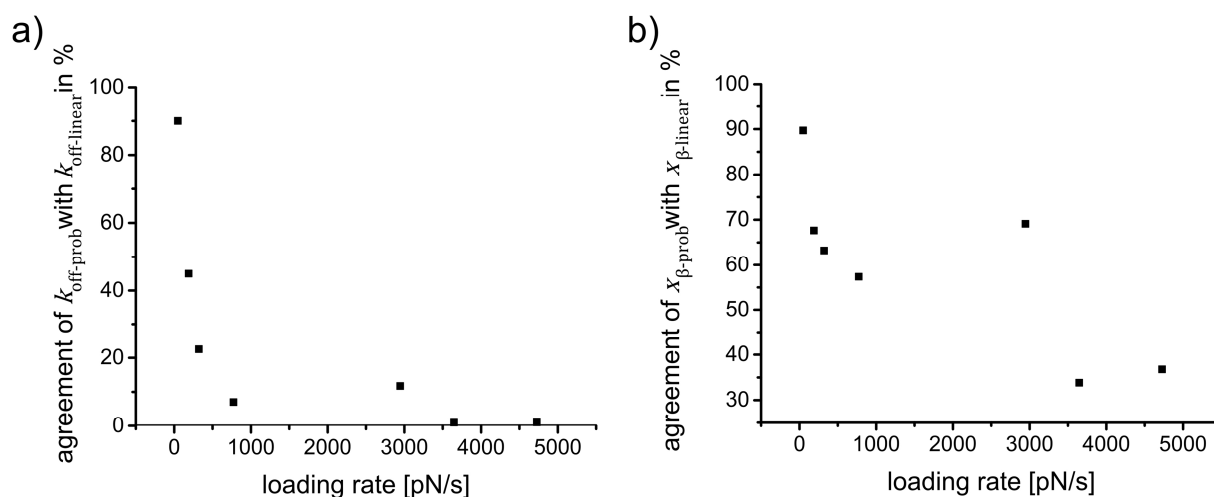


Figure 3.17: Agreement of the k_{off} and x_{β} values, determined by both methods. a) Plot of $(100(k_{\text{off-linear}} - k_{\text{off-prob}}/k_{\text{off-prob}})) + 100$ versus the effective loading rate. b) Plot of $(100(x_{\beta\text{-prob}} - x_{\beta\text{-linear}}/x_{\beta\text{-linear}})) + 100$ versus the effective loading rate.

3.6.4 Comparison to Literature

In the following, I will compare the probability fit calculation method to results from literature. The reason is, to cover a larger range of loading rates and most probable rupture forces, than available for complementary RNA. The first example shows the results of SMFS experiments with dimers of the amyloid β -protein. [99] The aggregation of amyloids is known to cause neurodegenerative diseases. In that particular paper, the intermolecular forces between different amyloid proteins were investigated. The thermodynamic- and kinetic-parameter were reportedly determined by the linear Bell-Evans fit and revealed the values $k_{\text{off}} = 1.9 \pm 0.1 \text{ s}^{-1}$ and $x_{\beta} = 0.305 \pm 0.029 \text{ nm}$ for the [VP]A β 40 construct ($F^* = 83.6 \text{ pN}$). Secondly, the construct A β 40 ($F^* = 57.0 \text{ pN}$) was investigated, which provided the parameter: $k_{\text{off}} = 9.0 \pm 2.4 \text{ s}^{-1}$ and $x_{\beta} = 0.222 \pm 0.018 \text{ nm}$. In order to evaluate the probability fit, I redraw their published histograms and applied the probability fit to their results. The results match perfectly with the published results (Table 3.2). Only the k_{off} of the A β 40 construct was with $12.4 \pm 6.5 \text{ pN/s} \approx 35\%$ larger than determined by the linear Bell-Evans fit.

Table 3.2: Analysis of published data from Lv et al. [99] with the here presented probability density fit method.

	loading rate [pN/s]	k_{off} [1/s]	x_{β} [nm]
[VP]A β 40	6068	1.9 ± 0.8	0.28 ± 0.03
A β 40	6215	12.4 ± 6.5	0.25 ± 0.05
A β 42	704	4.7 ± 1.5	0.36 ± 0.05
	2044	5.0 ± 3.2	0.30 ± 0.06
	4251	2.7 ± 2.3	0.37 ± 0.07
	10231	14.7 ± 6.8	0.19 ± 0.03
	21393	16.4 ± 8.2	0.19 ± 0.03
	52597	78.7 ± 31.1	0.11 ± 0.02

For the construct, named A β 42, a larger range of loading rates was tested (704 to 52597 pN/s). Their calculation revealed a k_{off} value of $5.7 \pm 0.3 \text{ s}^{-1}$ and a x_{β} value of $0.274 \pm 0.013 \text{ nm}$. The results of the probability fit provided a good match for the loading rates 704 pN/s to 2044 pN/s. At the loading rate 4251 pN/s, the published k_{off} was by a factor of ≈ 2 larger than the results obtained by the probability fit. In contrast to that, the k_{off} values at the loading rates 10231 pN/s and 21393 pN/s were by a factor of ≈ 3 larger. At the highest loading rate (52597 pN/s), the k_{off} value, determined by the probability fit, was even by a factor of ≈ 14 larger. In those cases with the largest difference between the published and the calculated k_{off} values, also the x_{β} values were the lowest. At the loading rate 52597 pN/s for example, the probability fit provided a x_{β} value of $0.11 \pm 0.02 \text{ nm}$. This values differs the most from the published x_{β} value of $0.274 \pm 0.013 \text{ nm}$. Thus, these results confirm that the probability-fit method provides reliable k_{off} values in case the x_{β} values are in agreement.

In a different example, also the interaction between amyloid- β proteins was reported. [100] The authors of that publication did not focus on the findings of amyloid- β aggregation, but compared different analysis models, namely Bell–Evans, Dudko–Hummer–Szabo and Friddle–De Yoreo (Table 3.3). The Bell model has been modified by Dudko, Hummer and Szabo to the so called microscopic model. The latter takes the harmonic spring of the pulled molecule and different shapes of the energy barrier into account. The model allows the assumption of a “cusp-like”, “linear-cubic” or “linear” barrier. The latter is equal to the Bell-Evans model. In the last years, Friddle and De Yoreo have addressed the possibility of rebinding between binding partners during SFMS experiments especially at low loading rates. [101] As result of their investigation, different dissociation rates were obtained, depending on the applied model. The k_{off} values, determined by the Bell-Evans model under consideration of the effective loading rate (correction for the PEG linker), differed by a factor of 30 from the calculation without correction. Also the dissociation rates, calculated either with the Friddle–De Yoreo or Dudko–Hummer–Szabo model differed by a factor of ≈ 16 . [100] Consequently, the

correction for the PEG linkers is needed to calculate reasonable k_{off} and x_{β} values. Rebinding of RNA-molecules is not expected for SMFS measurements by means of AFM, thus the Bell-Evans model is suitable.

Table 3.3: Comparison of the kinetic and thermodynamic parameter, analyzed with three different models. (Data used from Hane et al. [100])

DFS Model used for amyloid-β (1–42) data	k_{off} [1/s]	x_{β} [nm]
Bell–Evans (uncorrected for PEG linkers)	240.3 ± 36.5	0.143 ± 0.017
Bell–Evans (loading rates corrected for PEG linker)	8.44 ± 1.2	0.143 ± 0.016
Dudko–Hummer–Szabo (cusp model)	0.68 ± 0.4	0.205 ± 0.052
Friddle–De Yoreo (binned data)	11.1 ± 7.4	0.104 ± 0.019

The published histograms [100] were used to calculate the parameter according to equation 3.34. The closest results compared to literature are given for the loading rates 1850 and 9860 pN/s (Table 3.4). Here the k_{off} values are with a factor of ≈ 1 to 2 in the range of the published data. For the loading rates 23900 pN/s and 51900 pN/s the k_{off} values increased by a factor of ≈ 5 to 7, respectively. It can be observed that the convergence of k_{off} values is given for similar x_{β} values. In general, the x_{β} values decrease at higher loading rates. This can be correlated to larger FWHM values of the probability fits. At larger loading rates, the distribution of rupture forces becomes broader in comparison to measurements at smaller loading rates. The comparison with literature values gives an indication that reasonable k_{off} values may be calculated by the probability fit method for loading rates up to ≈ 3000 pN/s.

Table 3.4: Analysis of published data from Hane et al. [100] with the here presented direct fit method.

	F^* [pN]	Corrected loading rate [pN/s]	k_{off} [1/s]	x_{β} [nm]
amyloid- β (1–42)	55.4	1850	8.7 ± 3.3	0.15 ± 0.03
	99.6	9860	19.1 ± 6.4	0.11 ± 0.02
	136.9	23900	46.0 ± 18.7	0.06 ± 0.01
	128.2	51900	64.8 ± 33.5	0.09 ± 0.02

3.7 Summary and Conclusion

As an example for the dissociation of two binding partner, I presented the SMFS-based investigation of complementary RNA-strands. Two fitting models, based on the Bell-Evans method, were applied for the interpretation of rupture forces: The probability density fit model and the linear Bell-Evans model. I tested, to which extend the probability fit model can be used for a fast and reliable evaluation of force spectroscopy data. I found out that the full width at half maximum (FWHM) of the probability density functions has a big influence on the fit parameter k_{off} and x_{β} . An increase in FWHM is directly correlated to a decrease in x_{β} . More important is the effect of the FWHM on the k_{off} value, in case the most probable rupture force stays constant. That means, there are several effects that have an influence on the FWHM of the probability density function: overlap of the single rupture events with multiple rupture events [102, 103], (b) rebinding of molecules [84], (c) conformational changes within the molecule and (d) noise of the instrument [84]. The latter can result in a cut-off of the measured probability distributions at low forces. Thus the width of the distribution can be underestimated and consequently k_{off} appears smaller than it should be. In the case the most probable rupture force of a probability density function is kept constant, the effect of the FWHM on the determined k_{off} value becomes clear. An increase in the FWHM of the probability density function is related to an increase in k_{off} . These calculations sum up the large influence of the FWHM on the determined parameter.

The analysis of rupture force data has shown that reliable k_{off} values may be calculated with the probability fit method for loading rates < 3000 pN/s in case the x_{β} value matches the value, determined by the linear Bell-Evans method. At these loading rates, the probability distributions were narrower in comparison to the distribution of rupture data at higher loading rates. At the latter loading rates, not all intermolecular interactions might have been built between the binding partners. This results in the possibility of a larger number of different binding constellations, which lead to a larger FWHM. This observation was made for the rupture of complementary RNA-strands as well as for published force distributions of amyloid- β . Thus, the probability fit method may be used, in case the number of tested loading rates has to be minimized due to sample sensitivity. At low loading rates, the measurement with 1000 force-distance curves may require up to 3 h. Thus, sensitive samples could be investigated at one loading rate and the method would provide good estimates for k_{off} values. In contrast, stable samples should be analyzed at different loading rates with the linear Bell-Evans method to validate the results.

4. Split-RNA-Aptamer, Capable of Streptomycin-Binding

In the previous chapter, the single-molecule force spectroscopy technique was introduced as versatile tool for the analysis of interactions between binding partners. The foundation is set to expand the investigation of complementary nucleic acids to an aptamer, which has a binding pocket for specific analyte-binding. Due to the SELEX-process, the isolated aptamers usually consist of one single oligonucleotide strand, which folds to the functional aptamer. Nowadays, aptamers are frequently inserted into other oligonucleotide sequences to create functional elements. This may require the use of split-aptamers, which regain the aptamer properties upon hybridization. As a model system, I investigated the split-streptomycin-aptamer (pdb: 1NTB) by means of rate dependent force spectroscopy measurements.

4.1 Aptamers

Aptamers are oligonucleotides or peptides that are optimized for analyte-binding. Usually the term “aptamer” defines analyte-binding oligonucleotides. Whereas aptamers, which consist of amino acids, are called “peptide-aptamers”. Aptamers were discovered more than two decades ago by three independent working groups. Ellington and Szostak investigated the *in vitro* selection of RNA-sequences, capable of binding specifically small organic dyes (e.g. Reactive Blue 4). [7] Türk and Gold focused on the systematic evolution of random RNA-strands towards an oligonucleotide, which binds the T4-DNA-Polymerase of phages (gp43) with high affinity. [104] However, Joyce and colleagues investigated the directed amplification, mutation and selection of catalytic RNA. [105] All studies resulted in the generation of new aptamers with a high affinity for one analyte. [106] After the ground-breaking discovery of *in vitro* aptamers, similar nucleic acid structures were found in nature. In many different organisms, aptamers are parts of riboswitches and are coupled to regulatory units. [9] Depending on the presence of a specific analyte, they activate or deactivate cellular processes. [107]

The most important part of the aptamer is the binding-pocket, which enables analyte binding. The binding-pocket is a structural motif, which consists of the most prominent RNA-folding motifs (Figure 4.1). Watson-Crick base pairing stabilizes the structure of the aptamer-scaffold. Bulges and loops offer space and flexibility for the interaction between the nucleotides and the analyte, thus forming the structural motif of a selective recognition site. [108] The analyte is bound by intermolecular interactions to the binding-pocket. Depending on the chemical composition of the analytes, van der Waals forces, electrostatic interaction as well as hydrogen bonds facilitate analyte binding. [3] A larger number of intermolecular interactions increase the stability of the complex. The stability is a key parameter in biophysics for the efficient use of aptamers in drug and medical research. [38, 109, 110]

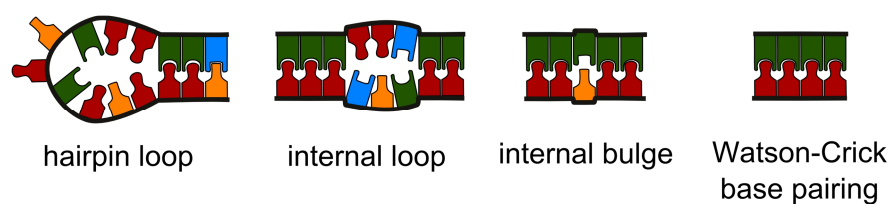


Figure 4.1: Schematic illustration of RNA binding motifs. Binding-pockets are usually built by internal bulges or loops, whereas Watson-Crick base pairing provides the stability for the overall structure. The bases are depicted as colored building blocks. (Adapted from [111])

4.1.1 SELEX-Process

The selection of aptamers is usually carried out by the so called SELEX-process (Systematic Evolution of Ligands by EXponential Enrichment). One round of the classical SELEX-process consists of five steps. The aim of the process is to select an aptamer with a high affinity and specificity for the analyte molecule of choice. In this process of *in vitro* selection and enzymatic amplification, just the oligonucleotides fitting/binding best to the analyte are selected (Figure 4.2).

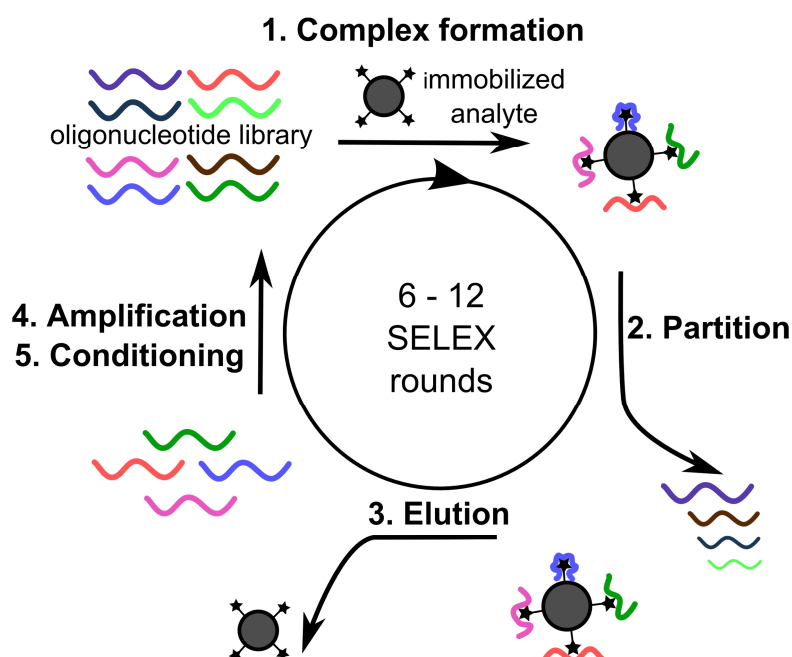


Figure 4.2: Schematic of the SELEX-process. The systematic evolution starts with an oligonucleotide library of typically $\approx 10^{15}$ different sequences. In the complex formation step, the analytes (black stars) are added to the oligonucleotide library. Usually the analytes are immobilized on a matrix, e.g. sepharose beads. In the partition step, the bound oligonucleotides are separated from the free oligonucleotides. In the elution step the evolved oligonucleotides are separated from the analytes. DNA oligonucleotides are amplified by PCR and purified in the conditioning step. RNA oligonucleotides are amplified by RT-PCR and conditioned by *in vitro* transcription. This results in an evolved oligonucleotide library. After 6-12 selection-rounds, aptamers with high affinity and specificity are selected. (Adapted from [112])

Usually, the process starts with a pool of 10^{15} different, randomized oligonucleotide sequences, referred to as library (Figure 4.2.1). Typically, these oligonucleotides have a length of 25 to 120 nucleotides. In the first step of the cycle, oligonucleotides attach to the added analyte molecules. The complex-formation step is performed in the so called selection buffer. This buffer contains mono- and divalent-ions and has a neutral pH, allowing the intramolecular hybridization of the oligonucleotides to specific tertiary structures. These tertiary structures are often equipped with bulges, internal loops and hairpin loops, which ensure the space and flexibility for analyte binding. [112] The selection conditions (buffer, pH, temperature) are usually similar to the conditions used in the detection systems and assays. Thus, the tertiary structure is likely to be the same.

In the partitioning step, the bound oligonucleotides are separated physically from the unbound oligonucleotides. In order to perform this partitioning, the analyte molecules are typically immobilized on sepharose beads. In the first selection-round, some oligonucleotides from the library may bind to the immobilized analytes. There are oligonucleotides, which build stable (Figure 4.2.1 blue) or less stable complexes (Figure 4.2.1 green) with the analytes. In the partitioning step (Figure 4.2.2), the unbound oligonucleotides are washed away and the bound oligonucleotides remain on the sepharose beads. In the following step, the preselected oligonucleotides are eluted from the sepharose beads (Figure 4.2.3). After amplification and conditioning of the evolved oligonucleotides, this round results in a new library of oligonucleotides (Figure 4.2.4). Typically between 6 and 12 rounds are necessary to obtain oligonucleotides with affinity constants in the micromolar range or lower, referred to as aptamers. The final oligonucleotide library is traditionally cloned into bacterial vectors for amplification. Each individual bacterial colony is sequenced to obtain the aptamer-sequence. After the aptamers primary composition is known, the aptamers can be synthesized chemically or *in vitro*. Often the selected aptamer sequences are compared for consistency and truncated to receive the smallest binding aptamer-building block. Finally, the dissociation constant is determined by binding studies, such as isothermal titration calorimetry (ITC), gel electrophoresis, high-performance liquid chromatography (HPLC) or surface plasmon resonance (SPR). [113] In the last two decades various modifications and improvements of the SELEX-process were introduced. [114]

Nevertheless, there are some fundamental differences in the evolution of DNA- and RNA-aptamers (Figure 4.3). The template oligonucleotides in the DNA-aptamer library consist of a random middle sequence and fixed 5'- and 3'-flanking regions. The middle sequence is usually composed of 20-80 nucleotides. The flanking 3'-regions consist of constant sequences, which are complementary to the used primers. For the selection of DNA-aptamers, the ssDNA library can directly be used. For the amplification of suitable candidates, PCR (polymerase chain reaction) is performed. In the denaturation step of the PCR-cycle, all hydrogen-bonds between the primer and the template oligonucleotides, as well as intramolecular hydrogen-bonds are broken at typically ≈ 95 °C. In the

annealing step at 50-65 °C, the primers hybridize specifically to the fixed sequences of the single-stranded template oligonucleotide. In the extension-step of the PCR-cycle, the Taq polymerase from *Thermus aquaticus* is used at its temperature optimum (≈ 72 °C) to build in 5' to 3' direction a complementary DNA strand to the DNA template strand. DNA oligonucleotides are amplified by PCR and purified in the conditioning step.

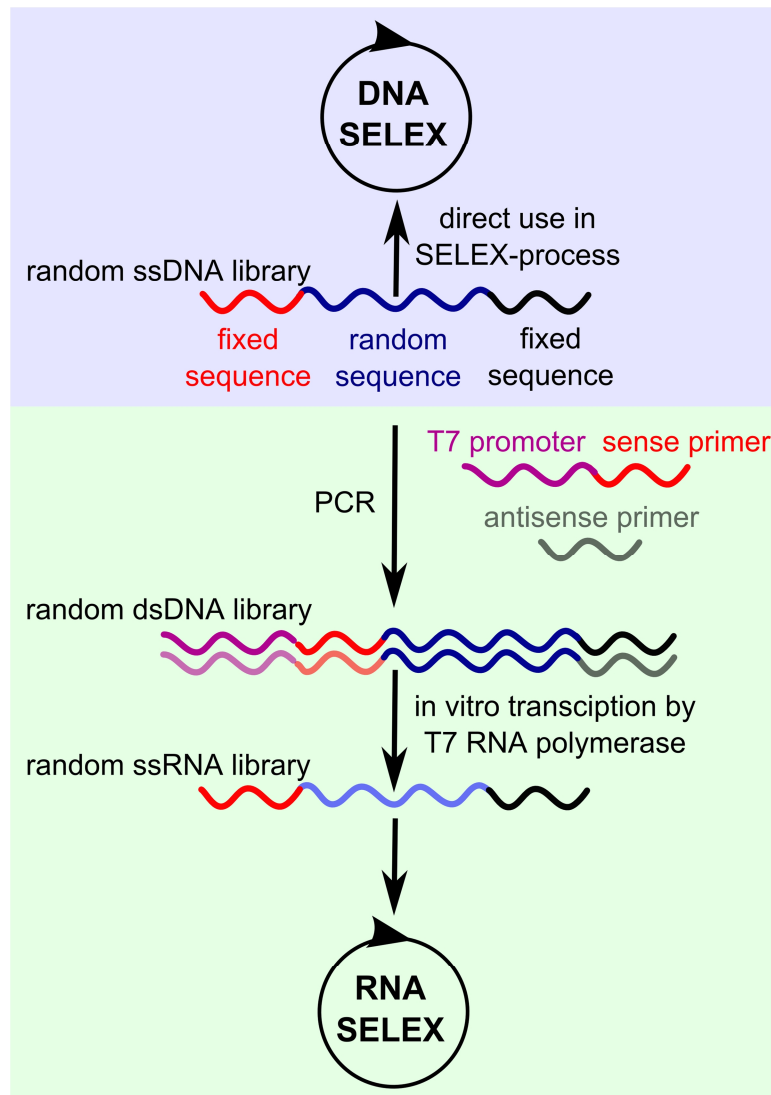


Figure 4.3: Schematic illustration of the oligonucleotide library preparation, adapted from Stoltenburg et al. [112]. The starting point of the DNA- and RNA-SELEX-processes is a random ssDNA library. These oligonucleotides have a random middle sequence and flanking fixed sequences. In the DNA SELEX, a random ssDNA library can directly be used. In contrast to that, in the RNA SELEX-process, the ssDNA has to be transformed into a ssRNA library by PCR and *in vitro* transcription.

The selection of RNA aptamers requires a translation of the single stranded DNA library (ssDNA library) into a single stranded RNA library (ssRNA library). Therefore, a PCR is performed with an antisense primer (indicated in gray) and a sense primer (indicated in red), which is connected to the T7 promoter region (indicated in violet). By means of PCR, a dsDNA library is generated, which contains

the T7 promoter region, named after the bacteriophage T7. In the next step, the T7 RNA polymerase uses the dsDNA library to generate, by *in vitro* transcription, a ssRNA library. In the last step of the SELEX, RNA oligonucleotides are transcribed by reverse transcription polymerase chain reaction (RT-PCR) into DNA, which is amplified. The conditioning is performed by *in vitro* transcription.

4.1.2 Streptomycin-Aptamer

Streptomycin ($C_{21}H_{39}N_7O_{12}$) belongs to the group of aminoglycoside antibiotics, which mediates its effect by binding to the 16S bacterial ribosomal RNA. [115] Therefore, it is often used as food additive in agriculture, causing disadvantageous residual amounts of streptomycin in food products [116]. One possibility to detect those residues with high selectivity is the use of aptamers. [117] Wallace et al. applied the SELEX-technique to identify an aptamer with high selectivity and moderate affinity ($K_d = 1 \mu\text{M}$) for streptomycin. [62] They used dihydrostreptomycin coupled to a sepharose matrix for the selection of the RNA-aptamer. Due to the selection process, this 46-mer aptamer consisted of one oligonucleotide strand. Tereshko et al. modified the aptamer by cutting the hairpin loop and adding dangling 5'-flanking ends for better crystallization. More precisely, one strand was extended with a single guanine and the other strand with a single cytosine base. These so called sticky ends facilitated the formation of co-crystal structures (Figure 4.4). [118] The hybridization of the 18-mer and the 22-mer RNA-strands resulted in a 40-mer aptamer. The first aptamer strand is numbered from nucleotide 1 to 22 and the second strand from nucleotide 101 to 118. Crystals of the streptomycin-RNA aptamer were grown within weeks and investigated by X-ray diffraction. Single-wavelength anomalous diffraction (SAD) revealed the structure of the complex at a resolution of 2.9 Å. The structure of the complex indicated intermolecular interactions between the aptamer and streptomycin and the formation of a 90° kink. The latter is located between the bases 12 and 16, bringing both internal loops closer together. The investigation revealed the stabilization of the geometry by additional hydrogen bonds between the streptidine ring and the surrounding atoms inside the binding pocket. [119]

In the following, the hydrogen bonds, identified by crystal structure analysis, are listed. The 2'OH of uracil at nucleotide position 11 (blue background in Figure 4.4) builds a hydrogen bond to the NH-group and to the glycosidic bond of the streptomycin molecule. The N7 of guanine at nucleotide position 12 (grey background in Figure 4.4) forms a hydrogen bond to the OH-group of streptomycin. Also the C6 carbonyl forms one hydrogen bond to the NH-group of streptomycin (grey background in Figure 4.4). The N3 of uracil at nucleotide position 16 (violet background in Figure 4.4) builds a hydrogen bond to the OH-group. The C4 carbonyl of uracil 17 (rose background in Figure 4.4) binds to the NH₂-group. The N7 of guanine 111 (yellow background in Figure 4.4) binds to the NH₂-group. The N7 of guanine 110 (orange background in Figure 4.4) binds to the NH₂-group and the phosphate

backbone binds to the NH-group. The 2'-ribose of cytosine 109 (green background in Figure 4.4) binds to the NH-group.

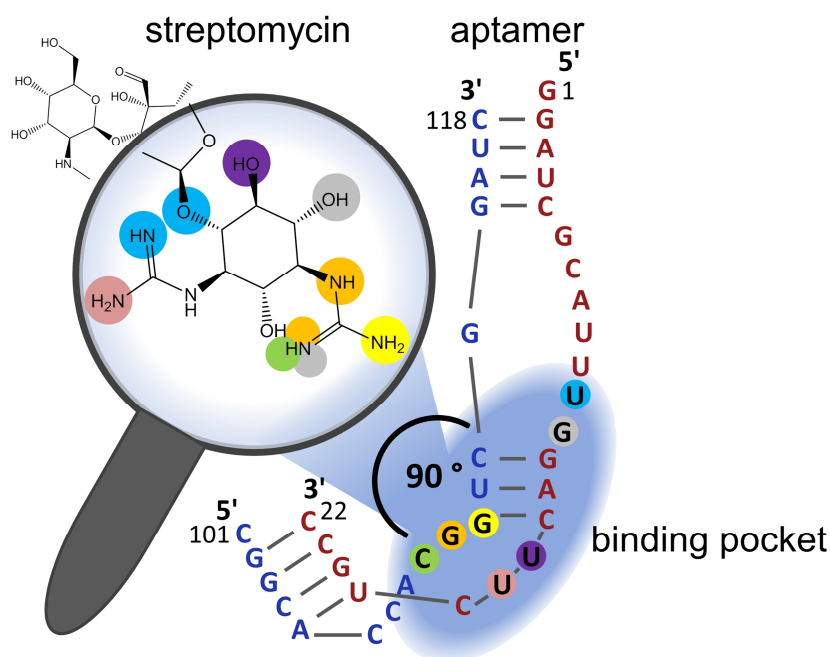


Figure 4.4: Scheme of the streptomycin-aptamer. The aptamer consists of two strands that form a binding pocket for streptomycin. The magnifying glass gives an insight into the chemical groups of the streptidine ring, involved in the formation of hydrogen bonds. The color code indicates the location of hydrogen bonds between the streptidine ring and the binding pocket. [120] The picture was adapted from Tereshko et al. [119] Reprinted with permission from (Nick, Thomas Alexander, et al. "Stability of a Split-RNA-Aptamer, Capable of Streptomycin Binding." *The Journal of Physical Chemistry B* (2016)). Copyright (2016) American Chemical Society.

The streptomycin-aptamer has found wide-spread use in the purification of RNA-protein complexes out of cellular lysate. This so-called "StreptoTag" consists of one oligonucleotide strand, which is immobilized on a column matrix. [63] The use of streptomycin as "StreptoTag" is possible, because just the streptidine ring protrudes inside the binding pocket (Figure 4.4). The other two rings are outside the binding pocket and enable a chemical connection of streptomycin to a matrix (e.g. glass) for an efficient purification process of RNA-protein complexes.

4.2 Single-Molecule Force Spectroscopy of RNA

Up to now, single-molecule force spectroscopy has rarely been used to investigate RNA-structures, carrying internal bulges or loops in the sequence. The origin of the bulges that have been studied were either non-complementary bases in both RNA-strands [42] or nucleotide mismatches and protuberances within the duplex. [43] The latter was investigated by Green and colleagues. [43] They studied 12-mer and 24-mer RNA-strands, which were either fully complementary or carried a bulge of three nucleotides in the middle of the sequence. In the case of the 12-mer RNA, the introduction of a bulge resulted in a decrease in the stability. The k_{off} -value increased from $0.40 \pm 0.20 \text{ s}^{-1}$ to

$7.94 \pm 1.77 \text{ s}^{-1}$. The authors concluded that changing a 12-mer into two 6-mers weakens the structure and thereby changes the energy landscape. For the 24-mer constructs, the opposite observation was made. There the bulge led to a decrease in k_{off} from $5.01 \pm 4.30 \text{ s}^{-1}$ to $0.0001 \pm 0.00002 \text{ s}^{-1}$. This result suggested a stabilization, derived by the bulge. Green and colleagues assumed an increase in flexibility upon bulge insertion, which allows a better hybridization of the oligonucleotides. These results showed that not only the bulge, but also the number of flanking oligonucleotides affects the stability of the oligonucleotides.

In a second example, Heus et al. reported on SMFS measurements with a part of the HIV-1 genome, which encodes for the envelope genes. This structure is built by two RNA-strands with two unsymmetrically internal loops, which have 4 complementary bases at both ends, respectively. The SMFS study revealed a k_{off} of 0.9 s^{-1} . Heus et al. concluded that this is a typical value for the rupture of only 4 - 6 complementary bases. The two internal loops interrupted the RNA-sequence and only a fraction of the complementary bases contributed to the stability. However, the two strands were still separated in a cooperative rupture process. [42]

4.3 Motivation

Here, the investigated, internal loop containing RNA sequence is an aptamer. Consequently I will elucidate in the following, the effect of bulges and internal loops as well as the effect of analyte binding in terms of k_{off} . [121] The measurements indicated that the internal loops in the streptomycin-aptamer decreased the overall stability, but the presence of streptomycin in the binding pocket counteracted this destabilization.

4.4 Rupture Geometries

The rupture geometry, which is chosen for SMFS experiments, affects the measured rupture forces of the oligonucleotide and thus its stability related to a parallel or perpendicular applied load. In shear geometry, [31] the load is applied parallel to the oligonucleotide-backbone (Figure 4.5a), while in zipper-geometry the load is applied perpendicular to the oligonucleotide-backbone. [122, 123] In the latter, the oligonucleotides are thought to be zipped open, nucleotide by nucleotide (Figure 4.5b). This work focused on the investigation of the streptomycin-aptamer in shear- and zipper-geometry. In order to eliminate error sources arising from different spring constants of cantilevers, the experiments were designed in such a way that the same tip was used throughout one experiment.

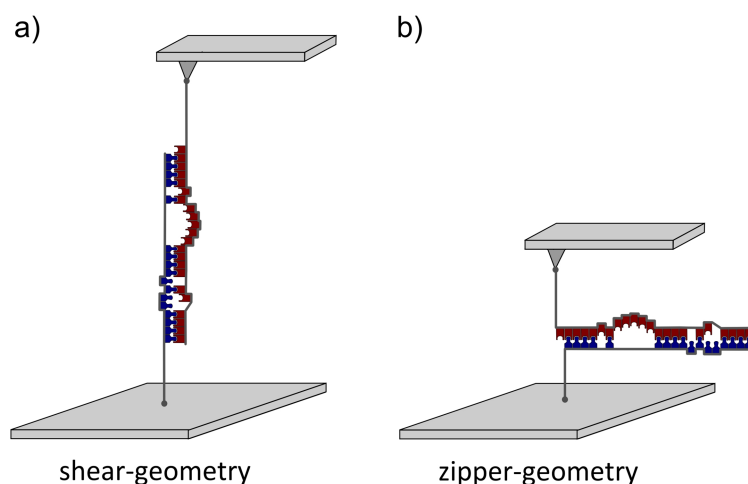


Figure 4.5: Schematic of the measurement-design for the investigated split streptomycin aptamer. The two rupture geometries shear (a) and zipper (b) are shown. Experiments in shear-, zipper- and subsequent reference experiments were performed with the same functionalized tip.

4.4.1 Shear-Geometry

The surfaces were prepared according to the protocol presented before (Chapter 2.1). The tip was functionalized with a 5'-thiolated RNA oligonucleotide (first strand: 5'-HS-gga ucg cau uug gac uuc UGC C-3') and the counterpart RNA strand (second strand: 5'-HS- cgg cac cac ggu cgg auc -3') was immobilized on the sample surface. The experiments were performed in the selection buffer solution (abbreviated with APTAMER), followed by experiments in buffer solution containing 50 μM of the target molecule streptomycin (abbreviated with COMPLEX). As control, the streptomycin molecules were washed away by rinsing the measurement chamber with pure buffer and the SMFS experiments were repeated. Approximately 10 – 15 % of the force-distance curves measured at one retract-velocity showed specific rupture events. The rupture-force and the rupture-distance were received from the final rupture point and plotted in histograms (Figure 3.7). The distance between the sample surface and the cantilever at the rupture point was denoted as rupture distance.

The probability fit (equation 3.34) revealed a most probable rupture force of 21.9 ± 1.7 pN for the measurement in buffer (Figure 4.6a). The error value of the most probable rupture force was determined by a propagation of uncertainties for the fit-parameters k_{off} and x_{β} . For the measurement in buffer solution, containing 50 μM streptomycin target molecule, a most probable rupture force of 31.1 ± 3.0 pN was obtained (Figure 4.6b). After washing the streptomycin molecules away, the rupture force shifted to 23.6 ± 1.3 pN (Figure 4.6c). Thus, the presence of streptomycin increased the most probable rupture force by ≈ 8 pN. This increase indicated additional intermolecular interactions, which were present until the complex ruptured. Considering SMFS experiments in literature, the increase in rupture force by 8 pN is reasonable. There, for the separation of two complementary DNA strands,

rupture forces of 4 ± 2 pN per 10 hydrogen bonds at a retract velocity of 100 nm/s were measured. Those systems consisted of DNA and did not exhibit bulges or internal loops. [39]

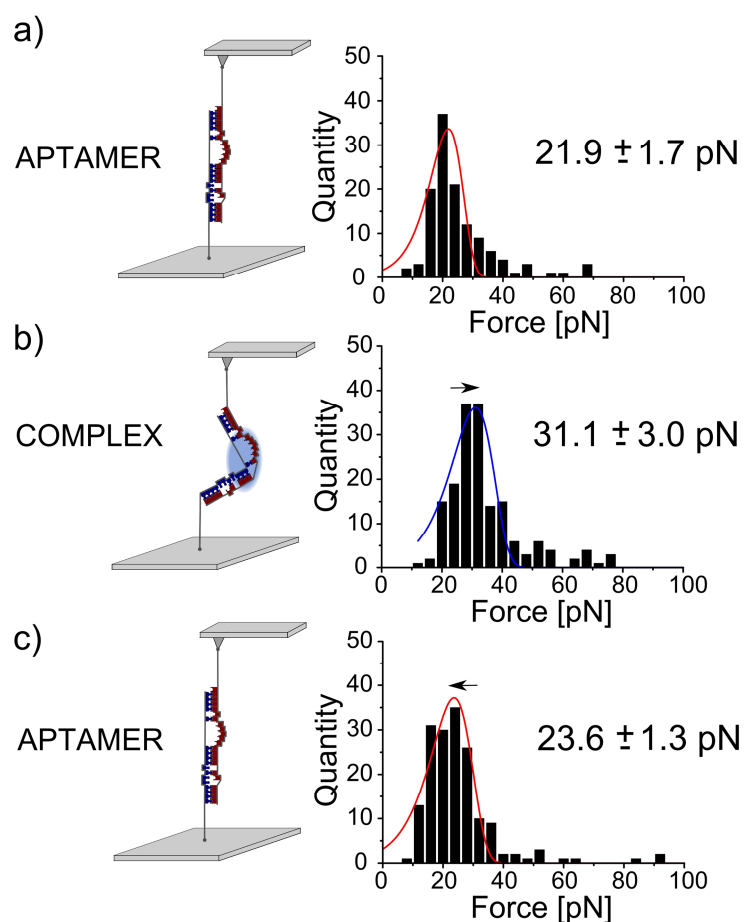


Figure 4.6: Exemplary histograms of rupture forces in shear-geometry, recorded at a retract velocity of 100 nm/s. The rupture forces were plotted in histograms with a bin size of 4 pN. The first histogram (a) represents the measurement in buffer (APTAMER) (123 rupture events). The second histogram (b) represents the measurement in the presence of streptomycin ($50 \mu\text{M}$) (COMPLEX) (170 rupture events). As control, streptomycin was washed away with buffer-solution (c) (APTAMER) (168 rupture events). The same tip was used throughout the experiments. The probability function, which is based on the Evans-Ritchie model (equation 3.34), was used to estimate the most probable rupture force of the histogram. [120] Reprinted with permission from (Nick, Thomas Alexander, et al. "Stability of a Split-RNA-Aptamer, Capable of Streptomycin Binding." *The Journal of Physical Chemistry B* (2016)). Copyright (2016) American Chemical Society.

According to the crystal structure analysis, the increase in the most probable rupture force could be attributed to additional hydrogen bonds, formed between the aptamer and the streptomycin. Based on the study by Tereshko, ≈ 10 additional hydrogen bonds were formed between the streptidine ring and the aptamer-binding pocket. [124]

Molecular dynamics (MD) simulations, performed by Paulo Netz, supported the results of Tereshko and coauthors. The inter-strand RNA-RNA hydrogen bonds, which build the scaffold for the aptamer, corresponded to the nucleotides 2 - 5, 7, 13 - 15 and 20 - 22 of the first strand. They formed

Watson-Crick base pairs with their complementary nucleotides of the second strand: 102 - 104, 111 - 114 and 115 - 118 (highlighted with a grey background in Figure 4.7a).

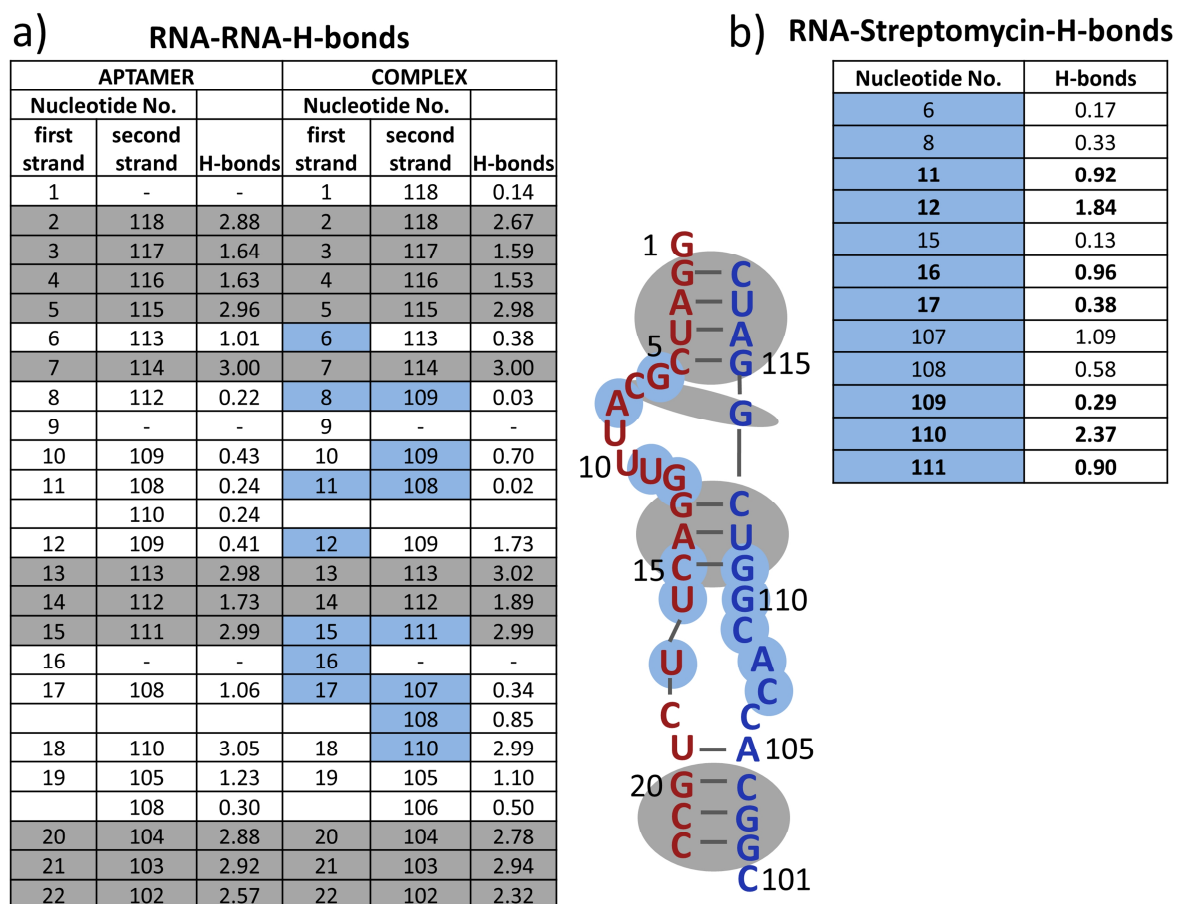


Figure 4.7: a) Average number of hydrogen bonds (abbreviated: H-bonds) between the nucleotides of both strands, as inferred by MD simulations. The aptamer scaffold was built by base pairing of the Watson-Crick type between the RNA-strands (highlighted with grey background). This table displays only those interactions to nucleotides that exhibited more than 0.1 hydrogen bonds in all three MD simulations. For clarity, just the most prominent Watson-Crick binding partners are shown. b) The average number of hydrogen bonds between the nucleotides and streptomycin are shown. The nucleotides, involved in streptomycin-binding, mostly belong to the unpaired nucleotides (highlighted with blue background). Most of those nucleotides were known by crystal structure (highlighted with bold letters). The average numbers of hydrogen bonds determined by three simulations are shown. Reprinted with permission from (Nick, Thomas Alexander, et al. "Stability of a Split-RNA-Aptamer, Capable of Streptomycin Binding." *The Journal of Physical Chemistry B* (2016)) Copyright (2016) American Chemical Society.

The MD simulation revealed that for these nucleotides, the average number of hydrogen bonds increased by approximately three hydrogen bonds upon streptomycin-binding. The other nucleotides did not have complementary nucleotides in direct proximity. Thus, they may build hydrogen bonds to the best suitable nucleotides. For example, the MD simulation showed that the nucleotides 8 and 112 just built in average 0.22 hydrogen bonds within the simulation time. The amount of hydrogen bonds between the nucleotides 6 and 113 was reduced (from 1.01 to 0.38) and increased between the nucleotides 12 and 109 (from 0.41 to 1.73) upon streptomycin-binding. The nucleotides 12 and 109 were not in proximity for the APTAMER but situated much closer for the COMPLEX. This could be

understood by the presence of a 90° kink, located between the nucleotides 12 and 16, in the COMPLEX structure, which was in agreement with the crystal structure. [124] Furthermore, the MD simulations showed that the nucleotides 9 and 16 were facing out of the tertiary aptamer structure and neither of them participated in the formation of the APTAMER nor of the COMPLEX.

Hydrogen bonds, which were established between each RNA-strand and streptomycin, are highlighted with a blue background (Figure 4.7). Those nucleotides 11, 12, 16, 17 and 109 - 111 were known from the crystal structure and confirmed by our simulations (highlighted with bold letters in Figure 4.7b). Beside these nucleotides, the simulations indicated also a possible formation of hydrogen bonds between the streptomycin molecule and the nucleotides 6, 8, 15 and 107 and 108. In particular nucleotide 107 and 108 together contributed with ≈ 1.5 hydrogen bonds. The sum of all additional hydrogen bonds (≈ 10) was identical to the sum of hydrogen bonds estimated by the crystal structure, although partially other nucleotides were identified by the MD simulations. In summary, either the presence of 10 additional hydrogen bonds between streptomycin and the aptamer or the three additional hydrogen bonds between the RNA-strands in the COMPLEX led to the increase in aptamer-stability upon streptomycin binding.

4.4.1.1 Bell-Evans-Fit

As explained in chapter 3, experiments at different retract velocities (25 - 1600 nm/s) allow the calculation of the natural off-rate. The histograms of the measurements, performed in buffer solution (Figure 4.8) and in buffer solution containing 50 μM streptomycin (Figure 4.9) revealed an increase in the most probable rupture force with increasing retract velocity.

The Bell-Evans model was applied in order to calculate the natural off-rate and the potential width (Figure 4.10). The linear fit revealed a natural off-rate of $k_{\text{off-Aptamer}} = 0.49 \pm 0.11 \text{ s}^{-1}$ for the system without streptomycin. The potential width corresponds to a value of $x_{\beta\text{-Aptamer}} = 0.75 \pm 0.03 \text{ nm}$. The off-rate decreased to $k_{\text{off-Complex}} = 0.22 \pm 0.16 \text{ s}^{-1}$ for the streptomycin containing system. The potential width increased to a value of $x_{\beta\text{-Complex}} = 0.68 \pm 0.10 \text{ nm}$. This result supports the assumption of an aptamer-stabilization, driven by a bound streptomycin molecule.

4. Split-RNA-Aptamer, Capable of Streptomycin-Binding

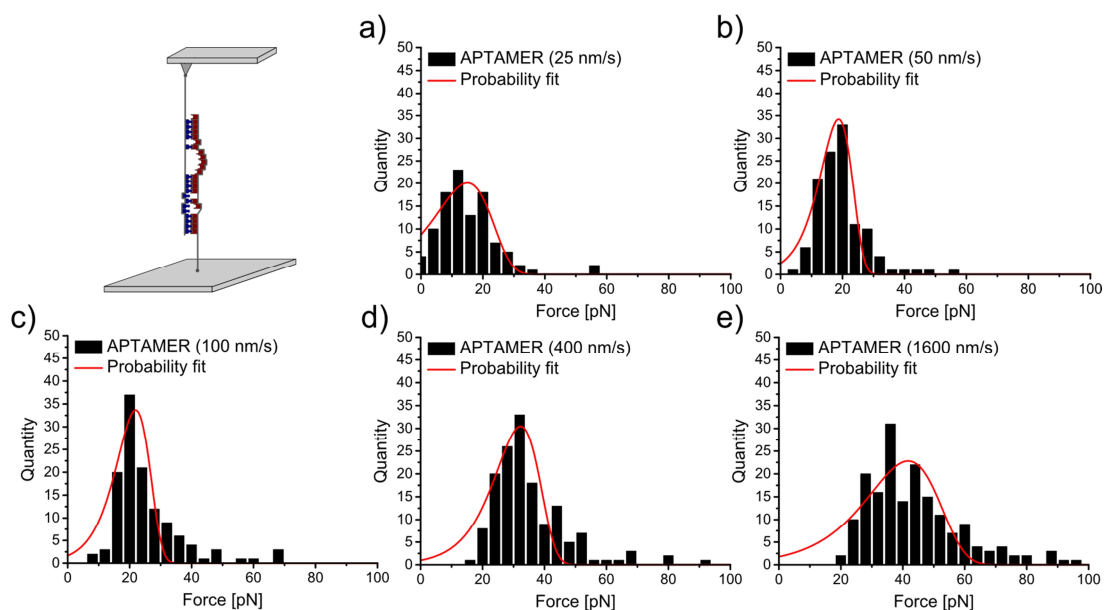


Figure 4.8: Histograms of rupture forces of the streptomycin-aptamer, recorded in buffer. Retract velocities ranging from 25 nm/s to 1600 nm/s were used. Approximately 10 - 15 % of the collected F-D curves showed a rupture event that was plotted in the histograms (bin size: 4 pN). The same tip was used for this set of experiments. The probability fit of the histograms was applied to estimate the most probable rupture force.

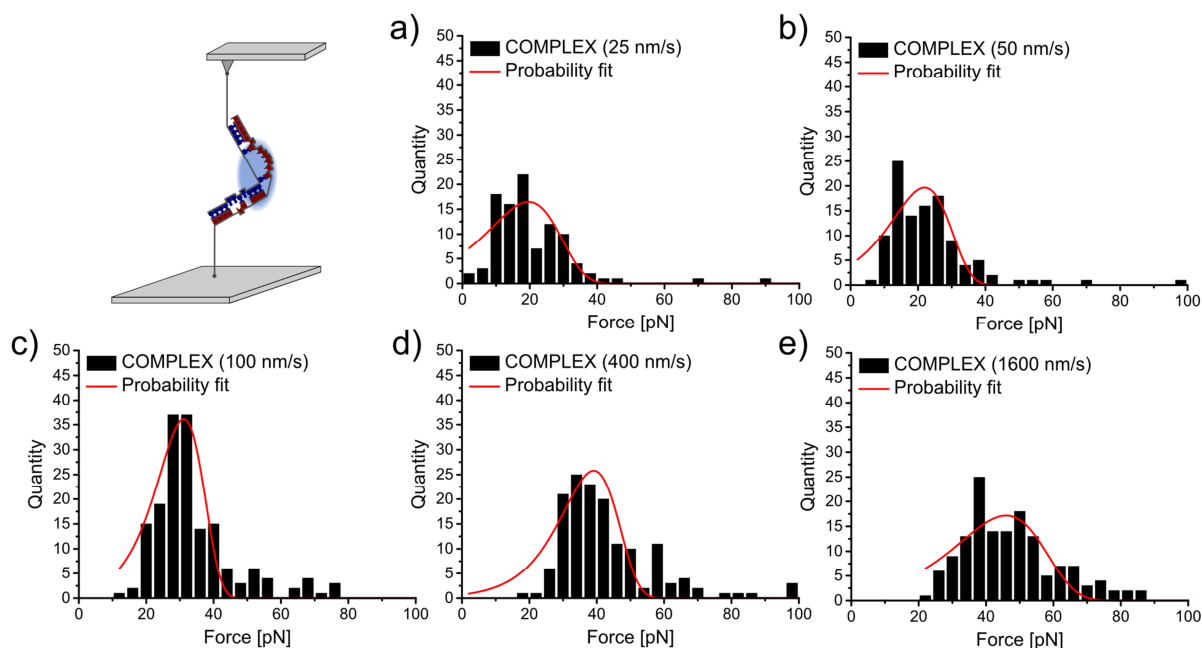


Figure 4.9: Histograms of rupture forces of the streptomycin-aptamer, recorded in buffer containing 50 μM streptomycin. Retract velocities ranging from 25 nm/s to 1600 nm/s were applied. Approximately 10 - 15 % of the collected F-D curves showed a rupture event that was plotted in the histograms (bin size: 4 pN). The same tip was used for this set of experiments. The probability fit of the histograms was applied to estimate the most probable rupture force. The most probable rupture forces were utilized for the Bell-Evans-fit.

As control experiment a fully complementary 18 nt RNA oligonucleotide was investigated (the histograms were shown in chapter 3.6.3. The most probable rupture forces (Figure 4.10) were

approximately 5–10 pN higher than the most probable rupture forces of the aptamer-streptomycin-complex. The calculated off-rate was $k_{\text{off-cRNA}} = 0.02 \pm 0.01 \text{ s}^{-1}$ and the potential width $x_{\beta\text{-cRNA}} = 0.78 \pm 0.06 \text{ nm}$. The result indicates an even more stable complex for the complementary RNA in comparison to the aptamer-streptomycin-complex. Binding of streptomycin leads to ≈ 10 additional hydrogen bonds and the complementary RNA to ≈ 17 additional hydrogen bonds in comparison to the aptamer-structure. The differences in the most probable rupture forces as well as the off-rate are in accordance with literature. This work additionally corroborates previously presented investigations for short, bulge carrying RNA-sequences. [43] One can conclude that a bulge may have a destabilizing effect on the RNA-structure for sequences with four to six neighboring nucleotides at the aptamer ends.

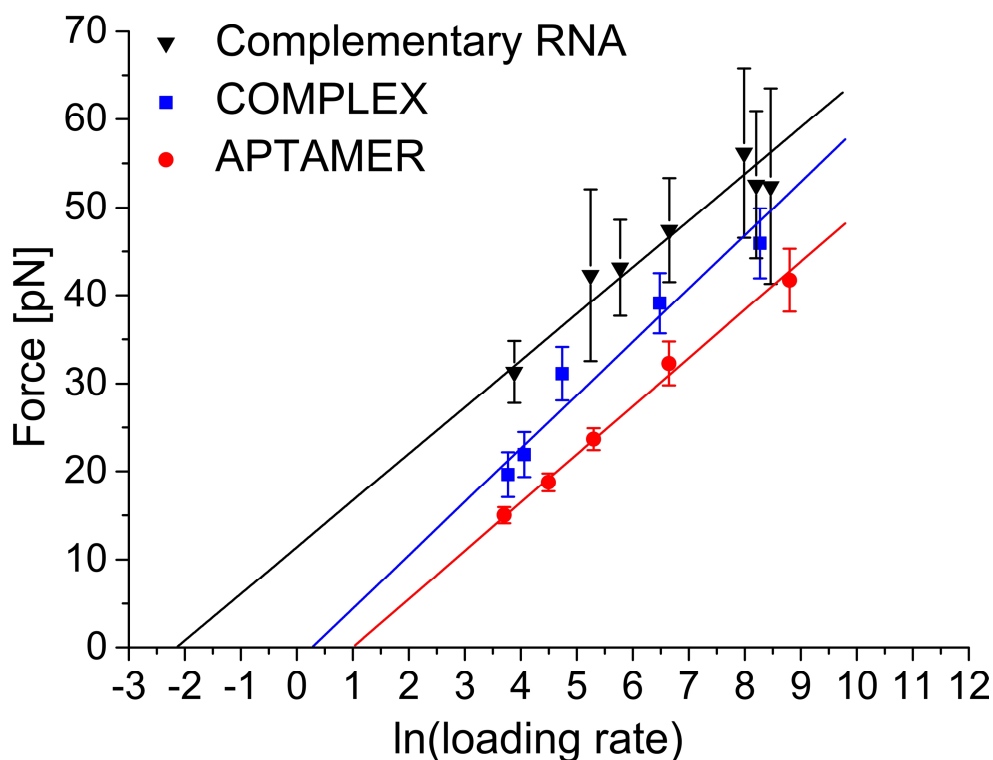


Figure 4.10: Most probable rupture forces, plotted as a function of the natural logarithm of the loading rate. The data sets were fitted with the Bell-Evans model for the APTAMER (red line), for the COMPLEX (blue line) and as control for two complementary RNA-strands (black line). Reprinted with permission from (Nick, Thomas Alexander, et al. "Stability of a Split-RNA-Aptamer, Capable of Streptomycin Binding." *The Journal of Physical Chemistry B* (2016)). Copyright (2016) American Chemical Society.

The change in the Gibbs free energy for the aptamer as well as for the aptamer-streptomycin-complex can be calculated according to:

$$\Delta G^{sheer} = -RT \ln \left(\frac{k_{\text{off}h}}{k_{\text{B}}T} \right) \quad (4.1)$$

with the gas constant (R) and the Planck constant (h) [96, 99, 100]. The Gibbs free energy of the aptamer system corresponds to $\Delta G_{APTAMER}^{sheer} = 75.1 \pm 0.5 \text{ kJ mol}^{-1}$ and of the aptamer-streptomycin-system to $\Delta G_{COMPLEX}^{sheer} = 78.5 \pm 1.7 \text{ kJ mol}^{-1}$. Thus, the change in ΔG upon streptomycin-binding ($\Delta\Delta G$) is $\approx 3.4 \text{ kJ mol}^{-1}$.

Breslauer et al. calculated the interaction between different base pairs of two complementary DNA strands. [125] These calculations revealed a Gibbs free energy ($\Delta\Delta G$) between 6 and 12 kJ per base pair upon separation, depending on the involved base pairs. De Silva et al. investigated binding forces of complementary DNA sequences by force-induced remnant magnetization spectroscopy. [126] The implementation of one single nucleotide mismatch in a 12-bp strand resulted in a decrease in the rupture force of $\approx 12 \text{ pN}$. Based on these measurements an increase in the Gibbs free energy of $\approx 9.7 \text{ kJ mol}^{-1}$ was calculated. Thus, the difference between $\Delta G_{APTAMER}^{sheer}$ and $\Delta G_{COMPLEX}^{sheer}$ of the streptomycin-aptamer measurements is in agreement with one additional base pair. [127] The result leads to the conclusion that mainly the additional hydrogen bonds, formed between the RNA strands contributed to the increase in stability. Especially the nucleotides between the bases 12 and 109 would build the additional link between the RNA strands. Consequently, only an increase in the stability of the aptamer upon analyte-binding can be measured by means of SMFS, when the additional hydrogen bonds are intact at the rupture-step.

4.4.2 Control measurements

Several measurements were performed for control reasons. One of these was to check, whether unspecific binding of streptomycin to the oligonucleotides increases the most probable rupture force. As control measurement, the glass sample was exchanged with a sample containing ssDNA strands with the sequence: 5'-HS-A20-GAG CCU AAA ACA UAC CAG AGA-3'. In order to compare the results with the streptomycin-aptamer, the same functionalized cantilever was used as in chapter 4.4.1 (Figure 4.11). The oligonucleotide-folding program *mfold* helped to predict the hybridization of the DNA-strand (sample) with the RNA-strand (cantilever). A similar amount of Watson-Crick base pairs, as present in the streptomycin-aptamer, was calculated. In contrast to the streptomycin aptamer, **no binding pocket** was formed for streptomycin binding. The measured most probable rupture forces were $21.9 \pm 0.3 \text{ pN}$ in buffer (Figure 4.11a) and $22.3 \pm 0.6 \text{ pN}$ in buffer, containing $50 \mu\text{M}$ streptomycin (Figure 4.11b). Thus, no significant increase in the most probable rupture force could be observed in this negative control.

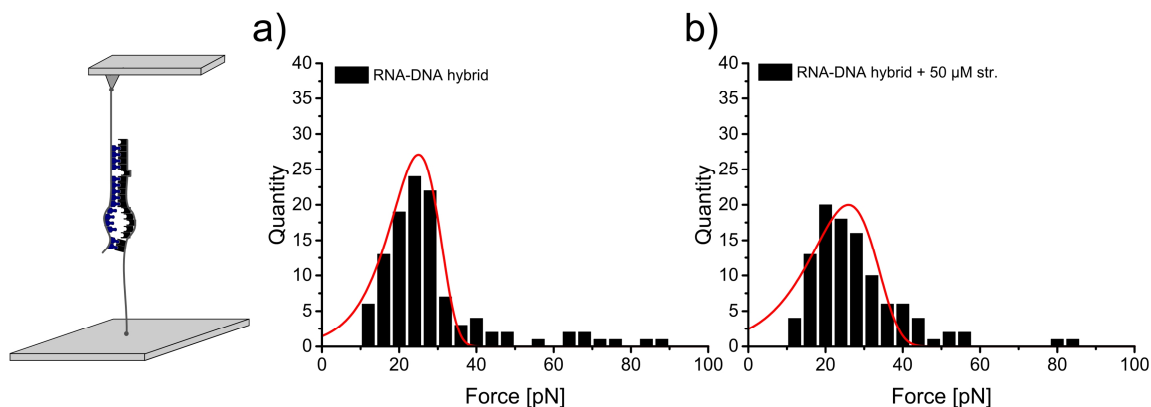


Figure 4.11: Histograms of rupture forces in shear-geometry, recorded at a retract velocity of 100 nm/s. The rupture forces were plotted in histograms with a bin size of 4 pN. The first histogram (a) represents the measurement of a RNA-DNA hybrid in buffer. The second histogram (b) represents the measurement of a RNA-DNA hybrid in the presence of streptomycin (50 μ M). This control system does not have a binding pocket for streptomycin. The most probable rupture force is practically unchanged in buffer (21.9 ± 0.3 pN) and in buffer containing 50 μ M streptomycin (22.3 ± 0.6 pN).

As **retest** of the APTAMER and COMPLEX measurements, independent samples were prepared and analyzed according to the previously described aptamer investigation (Figure 4.12). The most probable rupture forces and the resulting natural off-rates are in good agreement with the previously shown results. The linear fit revealed a natural off-rate of $k_{\text{off-APTAMER}} = 0.41 \pm 0.11$ s $^{-1}$ for the system without streptomycin. The off-rate was reduced to a value of $k_{\text{off-COMPLEX}} = 0.23 \pm 0.16$ s $^{-1}$ for the streptomycin containing system.

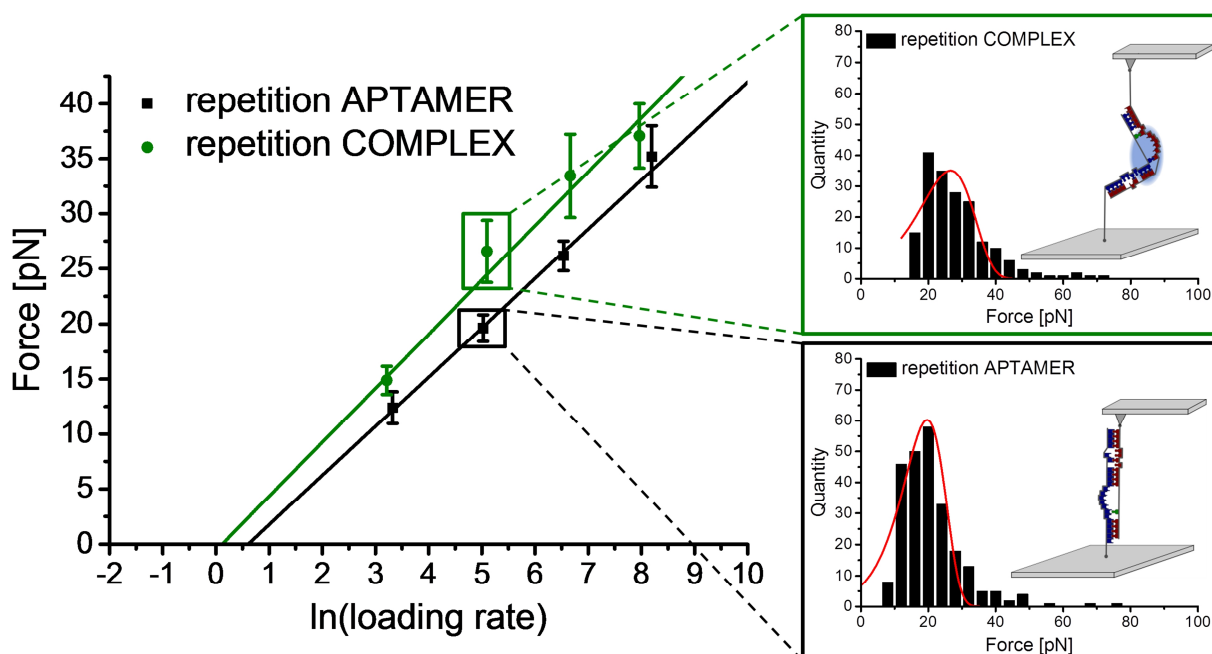


Figure 4.12: Independent control measurements of the streptomycin aptamer were carried out. The rupture forces were measured for the retract velocities 25 – 1600 nm/s. The probability function (equation 3.34) was used to receive the most probable rupture force. The presence of streptomycin increased the rupture force by approximately 6 pN. The applied Bell-Evans fit provided the natural off-rates.

Additionally, reference experiments were carried out with the first and the second oligonucleotide strand immobilized on the cantilever and substrate, respectively (Figure 4.13). In those measurements the oligonucleotides were connected to the surfaces with their 3'-thiols and consequently had an **inversed orientation**.

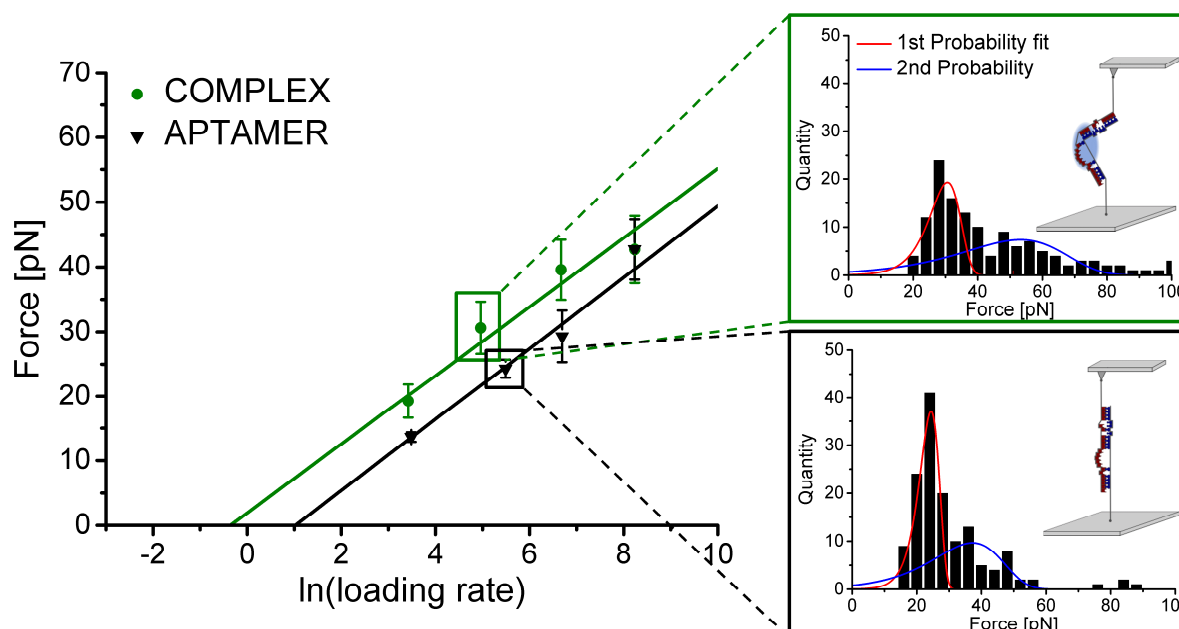


Figure 4.13: Control experiments with the first and the second oligonucleotide strand immobilized on the cantilever and substrate with their 3'-thiols. In those measurements the oligonucleotides were connected in the inversed orientation. The rupture forces were measured for the retract velocities 25 – 1600 nm/s.

While most histograms exhibited two peaks of rupture forces. I attribute the first peak to the rupture of single RNA strands and the second peak to the simultaneous rupture of several RNA strands. [128-132] Those histograms with two peaks, were fitted with the sum of two probability density functions $\rho_{1st}(F) + \rho_{2nd}(F)$, where $\rho_{1st}(F)$ corresponds to the probability density for a single RNA-aptamer rupture event and $\rho_{2nd}(F)$ to an event, where more than one RNA strand was involved. Consequently, the maximum value of $\rho_{1st}(F)$ corresponds to the most probable rupture force of a single RNA rupture event. The analysis of the rupture forces was carried out, as described for the previously presented aptamer-investigation. The determined natural off-rates of $k_{off-Aptamer} = 0.50 \pm 0.14 \text{ s}^{-1}$ and $k_{off-Complex} = 0.13 \pm 0.09 \text{ s}^{-1}$, were in good agreement with the results obtained by oligonucleotides attached with their 5'-thiols to the surface (Table 4.1). Nevertheless, the linear Bell-Evans fit of the COMPLEX in the inversed oligonucleotide functionalization revealed a $\approx 20\%$ smaller slope compared to the previous experiments. The reason is that the last data point of the measurement with streptomycin (Figure 4.13) is relatively low and causes a linear fit with a smaller slope.

Table 4.1: Summary of the results obtained for the streptomycin-aptamer and the complementary RNA.

	System	k_{off} [s^{-1}]
shear 5'/5' orientation	APTAMER	0.49 ± 0.11
	COMPLEX	0.22 ± 0.16
	18 nt complementary	0.02 ± 0.01
	retest APTAMER	0.41 ± 0.11
	retest COMPLEX	0.23 ± 0.16
shear 3'/3' orientation	APTAMER	0.50 ± 0.14
	COMPLEX	0.13 ± 0.09

4.4.3 Zipper-Geometry

Rupture measurements were also carried out in zipper-geometry, with the complementary RNA strand 5'-HS-cgg cac cac ggu cgg auc-3' attached to the glass sample. The experimental approach allowed the measurement in the zipper- and shear-geometry with the same cantilever, by simply exchanging the functionalized glass samples. This facilitated a comparison between the rupture-geometries. When the tip approached the surface, both RNA strands hybridized and upon retraction the strands were separated in zipper-geometry (Figure 4.14).

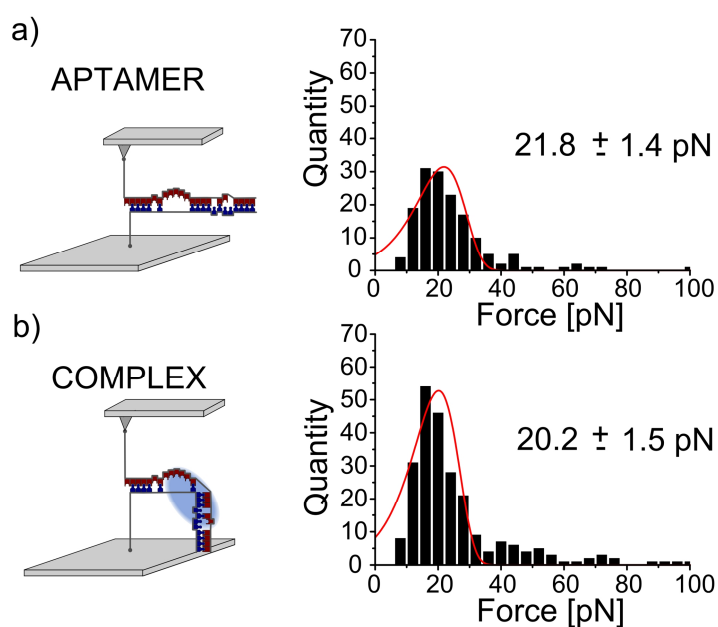


Figure 4.14: Exemplary histograms of rupture forces in zipper-geometry, recorded at a loading rate of 980 pN/s. Approximately 10-15 % of the collected F-D curves showed a rupture event that was plotted in the histograms (bin size: 4 pN). (a) Measurement in 50 μM streptomycin buffer-solution. (b) As control, streptomycin was washed away with buffer-solution. The same tip was used for this set of experiments. No shift in the most probable rupture force is observable.

In buffer, containing the target molecule, I obtained a histogram exhibiting a peak between 8 and 25 pN (Figure 4.14a). After washing streptomycin away with pure buffer solution, the peak remained unchanged within the precision of the experiment (Figure 4.14b). The amount of specific rupture events increased by 55% in the presence of streptomycin, which might be caused by a preferred hybridization of the oligonucleotide strands in the presence of streptomycin. In pure buffer solution, the most probable rupture forces corresponded to 21.8 ± 1.4 pN (Figure 4.14a). The measurement with 50 μ M streptomycin target molecule in buffer, revealed a peak value of 20.2 ± 1.5 pN (Figure 4.14b). In contrast to the measurements carried out in shear geometry, there was no increase in the most probable rupture force observable upon streptomycin binding. Also for the zipper geometry, speed dependent measurements were carried out. The measurements were carried out at the retract velocities 25 nm/s – 1600 nm/s with and without streptomycin. In three out of four cases, the most probable rupture force in buffer, containing streptomycin molecules, was even slightly less than for the measurements in buffer solution (red data points in Figure 4.15). No increase in the rupture force was observed. The aptamer strands were probably separated nucleotide by nucleotide like a zipper. Consequently, the binding pocket was disrupted during the rupture process and no cooperative rupture can be assumed.

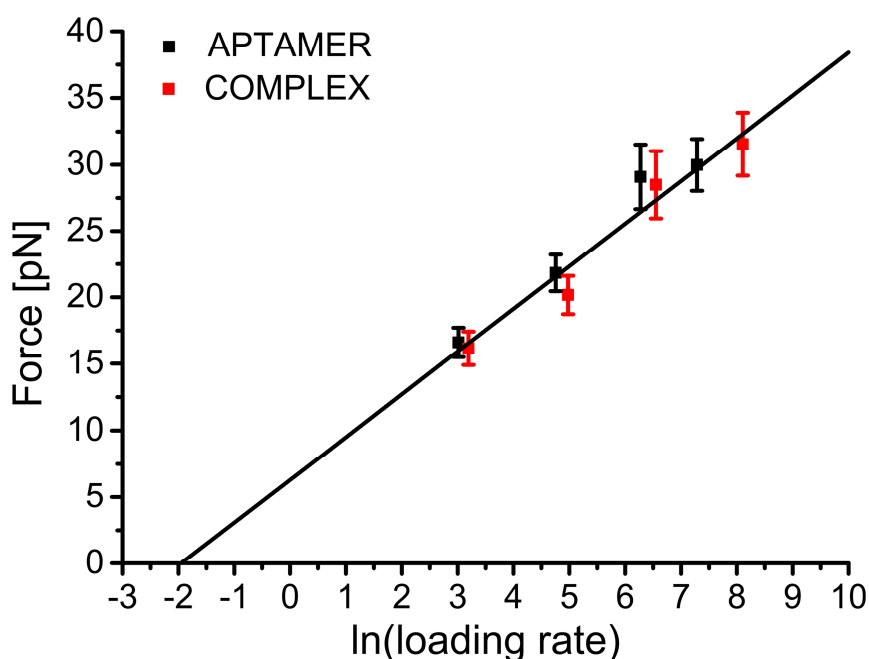


Figure 4.15: Most probable rupture forces measured in zipper-geometry and plotted as a function of the logarithmical loading rate. The data sets for the APTAMER and COMPLEX were fitted together with the Bell-Evans model (black line).

The most probable rupture forces were fitted logarithmically versus the loading rate according to equation 3.34. As no changes in the rupture force could be observed in the presence of streptomycin, the most probable rupture forces of all measurements were plotted and fitted linearly (Figure 4.15). The measurement revealed an off-rate of $k_{\text{off}} = 0.04 \pm 0.02 \text{ s}^{-1}$ for the system in zipper-geometry with a potential width of $x_{\beta} = 1.29 \pm 0.11 \text{ nm}$.

In the zipper geometry, both RNA strands were separated in a step-wise rupture process, which resulted in a lower force compared to experiments performed in shear geometry. This structural condition was reportedly used in the so called “cut-and-paste surface assembly”, which allows the picking-up of DNA-strands and a selective deposition. [133] The absence of a force shift is in accordance with the experimental results, presented by Sengupta and coauthors. They claimed that the pulling force is primarily acting on the first 5 base pairs and the following bases open like a zipper. [33] The first 5 neighboring bases, which stabilize the structure for a binding pocket are then supposed to rupture in one step and the rest of the aptamer follows stepwise. The previously discussed 90° kink could not be detected in the zipper-geometry. I assume that there is either no prominent kink or it is opened easily.

4.5 Summary and Conclusion

My single-molecule force spectroscopy results of the streptomycin-aptamer were in agreement with literature. Experimentally, binding of streptomycin to the aptamer resulted in an increase in the rupture force between both RNA-strands, compared to an empty binding pocket. However, the rupture force of a fully complementary RNA strand was almost reached with the split-streptomycin-aptamer. Single-molecule force spectroscopy, performed at different loading rates, revealed an off-rate of the aptamer-streptomycin complex of $k_{\text{off-Complex}} = 0.22 \pm 0.16 \text{ s}^{-1}$. The off-rate for a system with a flexible bulge increased to $k_{\text{off-Aptamer}} = 0.49 \pm 0.11 \text{ s}^{-1}$. The natural off-rate for the fully complementary RNA-strands corresponded to $k_{\text{off-cRNA}} = 0.89 \pm 0.16 \text{ s}^{-1}$, which was not reached with the aptamer-streptomycin complex.

The determined change in the free energy ($\Delta\Delta G^{\text{sheer}} \approx 3.4 \text{ kJ mol}^{-1}$) is in agreement with the stabilization of an oligonucleotide with one additional base pair. MD simulations, performed by Paulo Netz, revealed that three additional hydrogen bonds are built upon streptomycin-binding. This led to the conclusion that the three additional hydrogen bonds between both RNA strands mainly contribute to the increase in rupture force of the aptamer system studied. Therefore other hydrogen bonds between the RNA strands and the streptomycin do not seem to play a major role in the measured rupture force increase. This suggests that upon pulling on one strand, the binding pocket of the aptamer is stretched and partially hydrogen bonds are broken even before the rupture of the

COMPLEX occurs. Thus, finally only hydrogen bonds between the RNA strands contribute to the final cooperative rupture process. Consequently, our results suggest that the choice of split-aptamer systems, accessible for single-molecule force spectroscopy in shear geometry, might be limited to split aptamers, which build hydrogen bonds between the aptamer strands upon analyte-binding. Only in those cases, a final cooperative rupture event might be present. The latter was also the case for a split adenosine monophosphate (AMP) aptamer system studied by Nguyen and coauthors. [18] In that aptamer system, binding of the AMP analyte molecule led to additional hydrogen bonds between both DNA strands by forming a G-quadruplex.

In zipper-geometry the stability stayed unaffected by the target molecule streptomycin ($k_{\text{off-Aptamer}} = 0.04 \pm 0.02 \text{ s}^{-1}$). Thus, this work confirms the reported structural condition that unzipping RNA requires less force than rupturing RNA in shear-geometry. [33, 134, 135] The streptomycin aptamer has a complicated and asymmetrical structure, built by two internal loops. Thus, the change of the streptomycin molecule, to be bound inside the binding pocket, while zipping the aptamer-strands apart, is small. I conclude that the rupture geometry, which is suitable for investigating a stabilizing effect of analytes, is the shear-geometry.

5. Combination of Analyte-Binding-Oligonucleotides

In this chapter the dissociation of oligonucleotides by means of temperature dependent UV/Vis-absorbance measurements is elucidated. The interaction of analytes with oligonucleotides can lead to a thermal stabilization of the oligonucleotide structure or a substructure, which is indicated by an increase in the melting temperature. [57, 136] Those analytes can be ions [56, 58, 137, 138], small molecules like aminoglycosides [54, 139-143] or macromolecules like proteins [144]. In particular oligonucleotides are of interest, which show an increased thermal stability upon binding of a specific analyte. The shift in the melting temperature is a measure of stabilization, which suggests favored analyte-binding. Consequently, analyte-binding is typically characterized by a decreased ΔG° , which indicates a favored reaction.

In what follows, theory will first be applied to a single aptamer, then the other binding-site and finally the combination of both will be addressed. According to literature, the neomycin-aptamer and the Hg^{2+} -binding DNA are promising candidates.

The questions I address here are: 1) Do the oligonucleotides keep their function in the same buffer (20 mM phosphate buffer, 100 mM NaCl, pH 7)? 2) Is there a crosstalk between the positively charged analytes and the other binding-site? 3) At which position can the neomycin-aptamer be split, without losing the functionality of the neomycin-binding-site?

5.1 Temperature Dependent UV/Vis-Absorbance Measurements

Oligonucleotides contain purines and pyrimidines as chromophores, which have a characteristic ultraviolet absorbance spectrum with a peak maximum at 260 nm. [145] Consequently, oligonucleotides are good candidates for the investigation by means of UV/Vis-absorbance measurements. In this biophysical technique the ultraviolet- (UV) and visible-light (Vis) absorbance of molecules is measured. In UV/Vis-measurements the excitation of valence electrons is restricted to chromophores with low electron excitation energies. The wavelength, used to promote an electron from the highest occupied molecule orbital (HOMO) to the lowest unoccupied molecule orbital (LUMO) is in the range between 200 and 700 nm. The characteristic absorbance band of a molecule is the combination of overlapping electronic transitions. The measured absorbance (A) can be used to calculate the total oligonucleotide strand concentration for homogeneously distributed oligonucleotides in solution according to Lambert-Beer's law:

$$A = \epsilon c l \quad (5.1)$$

with the material-specific extinction coefficient (ϵ in $\text{Lcm}^{-1}\text{mmol}^{-1}$), the concentration (c in mmol/L) and the path length of the beam of light through the material sample (l in cm). The extinction

coefficients of the nucleotides in the particular RNA or DNA (at 260 nm, 25 °C, 0.1 ionic strength and pH 7) are: $pA = 15.34 \text{ Lcm}^{-1}\text{mmol}^{-1}$, $pC = 7.6 \text{ Lcm}^{-1}\text{mmol}^{-1}$, $pG = 12.16 \text{ Lcm}^{-1}\text{mmol}^{-1}$, $pU = 10.21 \text{ Lcm}^{-1}\text{mmol}^{-1}$, $pT = 8.7 \text{ Lcm}^{-1}\text{mol}^{-1}$. [146] Changing the measurement conditions results in different extinction coefficients.

The UV/Vis-spectroscopy is frequently used for the determination of concentrations of molecules in solution or for the detection of changes in absorbance caused by temperature. The latter is applied to observe the change of oligonucleotides from the native, hybridized state to the denaturated, disordered state. In the disordered state, the absorbance of the oligonucleotide is the sum of the nucleotide absorbance. As an example, one strand of the original Hg^{2+} -binding DNA (5'-CCG CGT TCT CCG-3') has an extinction coefficient of $108 \text{ Lcm}^{-1}\text{mmol}^{-1}$ ($= 6 \cdot 7.6 \text{ Lcm}^{-1}\text{mmol}^{-1} + 3 \cdot 12.6 \text{ Lcm}^{-1}\text{mmol}^{-1} + 3 \cdot 8.7 \text{ Lcm}^{-1}\text{mmol}^{-1}$). The basis for the investigation of oligonucleotides by means of temperature dependent UV/Vis-absorbance measurements is a 15 - 20 % lower absorbance of native oligonucleotides, compared to denaturated oligonucleotides. [52] This effect, known as hyperchromicity, is caused by the hydrophobic environment inside a helix formed by π - π stacked rings of nucleotides. Consequently, the extinction coefficient of denaturated oligonucleotides is larger than that of native oligonucleotides. The maximal effect of hyperchromicity of A-T and G-C base pairs is observed at a wavelength of 240 nm and 280 nm, respectively. [147, 148]

A common way to denaturate oligonucleotides is by increasing the temperature. This process is referred to as melting, which is the result of breaking the non-covalent, intermolecular interactions between hybridized oligonucleotides and the change of the ion-hydration environment. In the temperature-driven process, the melting temperature (T_m) is defined as the temperature, at which the fractions of native and denaturated oligonucleotide strands are equal. The melting temperature is a measure of strand stability and depends on the strength of intermolecular forces. Thus, for example, oligonucleotides with poly G-C base pairs have higher melting temperatures than poly A-T oligonucleotides. For complementary oligonucleotides two states are present: the native and the denaturated state (Figure 5.1). The melting of a stretch of complementary nucleotides is considered a cooperative process, because denaturated oligonucleotides favor the dissociation of neighboring nucleotides. Oligonucleotides with a length below 30 bp will typically denaturate either on one end alone or from two ends simultaneously (Figure 5.1a and b). In nucleotides with a length of more than 30 bp, in nucleotides with base mismatches or in A-T rich regions the denaturation might additionally start within the sequence (Figure 5.1c). [149] In those regions of oligonucleotides, where mismatches are present or where analytes bind, the denaturation process can be non-cooperative.

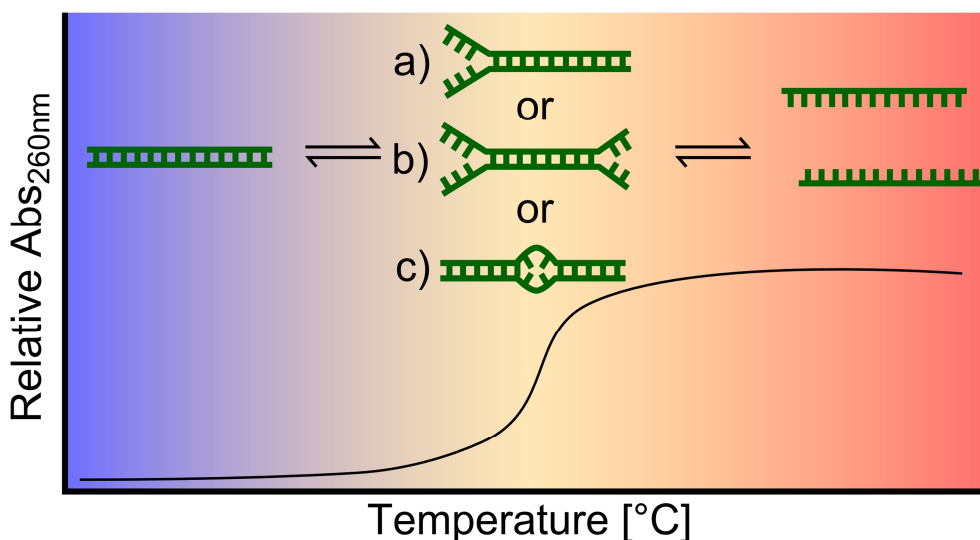


Figure 5.1: Schematic of the two-state melting process with possible intermediate structures of fully complementary oligonucleotides. The denaturation process can start: a) from one end, b) from both ends or c) from the center of the double helix.

The presence of salt and therefore of cations, increases the melting temperature because of shielding of the negatively charged phosphate-backbone. Temperature dependent UV/Vis-absorbance measurements do not only provide the melting temperature but can also be used to estimate the thermodynamic parameter ΔH° , ΔS° and ΔG° of oligonucleotides. Measurements can be performed in one day and are inexpensive, since only small amounts of oligonucleotides (150 - 1500 pmol) are needed. A functional binding-site is indicated by an increase in the melting temperature upon analyte-binding. In the following, the results of the temperature dependent UV/Vis-absorbance measurements for a neomycin-aptamer and a Hg^{2+} -binding-DNA are discussed.

5.2 Neomycin-Aptamer

5.2.1 Structure of a Neomycin-Aptamer

Neomycin ($\text{C}_{23}\text{H}_{46}\text{N}_6\text{O}_{13}$), like streptomycin, belongs to the group of aminoglycoside antibiotics. It has been shown that neomycin binds to various RNA-structures, including the decoding site of 16S rRNA ($K_d = 0.32 \pm 0.03 \mu\text{M}$ measured by surface plasmon resonance) [150, 151] and the Rev-responsive element in HIV-1 ($K_d = 0.25 \pm 0.05 \mu\text{M}$ measured by stopped-flow kinetic measurements) [152, 153]. Complex-formation between the RNA and neomycin leads to a loss of its physiological function. The antibacterial effect against gram-positive and gram-negative organisms is caused by a blocked bacterial protein synthesis after binding to the 16S rRNA.

Wallis et al. have identified an RNA-aptamer in vitro, which is capable of neomycin binding. Depending on the buffer conditions, dissociation constants in the range of $0.1 \mu\text{M} - 7 \mu\text{M}$ were

reported. [54, 154-156] Jiang and colleagues have investigated this truncated 23mer aptamer by means of NMR in solution. [157] In accordance with literature the numbering of the 23mer aptamer is maintained. Thus, the aptamer sequence starts with the guanosine 4 and ends with the cytosine 26 (Figure 5.2).

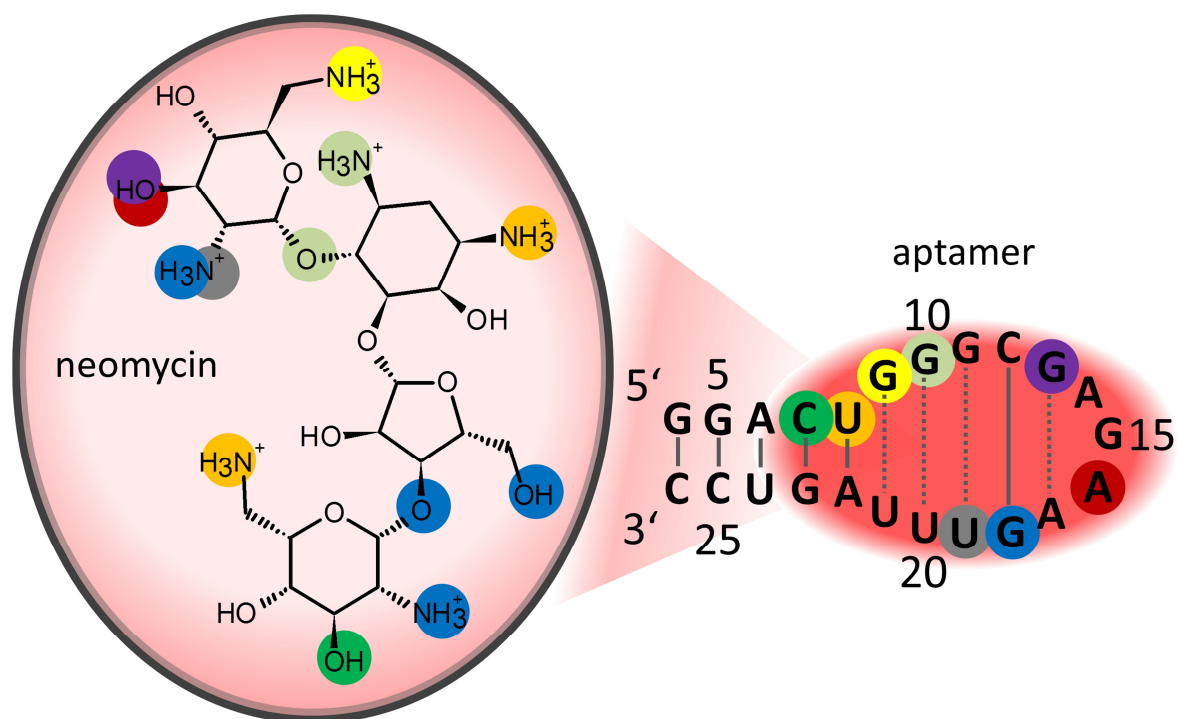


Figure 5.2: Scheme of the neomycin-aptamer. The picture was adapted from Jiang and colleagues. [157] The aptamer consists of one strand, which forms a binding pocket for neomycin. The magnifying glass gives an insight into the chemical groups of the neomycin molecule, involved in the formation of hydrogen bonds. The color code indicates the location of hydrogen bonds between the neomycin molecule and the binding pocket.

The neomycin molecule is a polycationic molecule with a charge of +5 at neutral pH. In the complex with the aptamer, the neomycin molecule stays fully protonated (charge +6) up to a pH of 9. [158] Binding of the neomycin molecule to the RNA-aptamer is facilitated by the formation of a binding pocket. The binding pocket is the strong binding-site, whereas the stem loop region is a weaker binding-site for a secondary binding neomycin molecule. [54] Only the structural investigation of the strong binding-site was supported by NMR investigations. Neomycin builds 16 hydrogen bonds to the binding pocket, which explains the increase in the melting temperature upon analyte-binding compared to the aptamer itself. [157] The scaffold structure of the aptamer is built by the flanking Watson-Crick nucleotides G4 to U8 and their complementary counterparts. The binding pocket consists of different structural elements enabling neomycin binding. The base pairs G9 - U21 and G10 - U20 are building two hydrogen bonds, each as wobble alignment. The G11 - U19 mismatch and the G13 - A14 - G15 - A17 hairpin loop do not form bonds of the Watson-Crick type. This hairpin loop is a classical GNRA tetraloop type, stabilized by base stacking, G-A base pairs and 2' OH-base hydrogen bonds. [159] The Watson-Crick pair G18-C12 stabilizes the middle of the binding pocket,

whereas the A16 is flipped out of the sequence and over the bound neomycin molecule. The phosphate backbone of guanine 9 binds to the $-\text{CH}_2\text{-NH}_3^+$ -group of the pyranose ring 1. The N1 and the NH_2 of guanine 13 bind to the C3 carbonyl of the pyranose ring 1. One hydrogen bond is formed between the phosphate backbone of adenine 16 and the C3 carbonyl of the pyranose ring 1. Guanine 18 builds two hydrogen bonds: One with the C6 carbonyl and the other with the N7 to NH_2 . One hydrogen bond is formed between the C4 carbonyl and NH_2 . Uracil at position 8 builds one hydrogen bond with the C6 carbonyl to the NH_3^+ at the position C3 in the 2-deoxystreptamine ring. The N7 of guanine 10 forms a hydrogen bond to the C1- NH_3^+ of the non-sugar 2-deoxystreptamine ring. The C6 carbonyl builds one hydrogen bond to the glycosidic ring that connects the non-sugar 2-deoxystreptamine ring and the pyranose ring 1. Two hydrogen bonds are formed by guanine 18. One with the phosphate backbone to the glycosidic bond that connects the furanose ring and the pyranose ring 4. Another hydrogen bond is formed between the N7 and the C2 carbonyl. The phosphate backbone of cytosine 7 builds one hydrogen bond to the C4 carbonyl of the neosamine ring. The phosphate backbone of uracil 8 builds one hydrogen bond to the $-\text{CH}_2\text{-NH}_3^+$. The phosphate backbone of guanine 18 forms two hydrogen bonds to the $-\text{NH}_3^+$ -group.

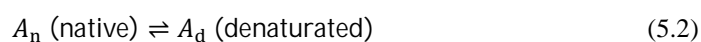
The melting temperature increased, according to Stampfl et al., by $\approx 10^\circ\text{C}$ in a cacodylate buffer containing 80 mM NaCl and 5 μM neomycin. [54] Their steady state fluorescence studies revealed a K_d of 0.2 μM at a 10 mM NaCl concentration and a K_d of 7 μM at a 100 mM NaCl concentration. The analyte-binding property, measured in different buffers with different techniques was reported as follows:

1. 10 mM phosphate buffer solution at pH 6.1; $K_d \approx 0.1 \mu\text{M}$, determined by NMR [157]
2. 80 mM cacodylate, 80 mM KCl, 200 mM NH_4Cl , 5mM MgCl_2 at pH 7.4; $K_d \approx 1.9 \mu\text{M}$, determined by 2-aminopurine steady state fluorescence studies [160] 0.2
3. 35 mM HEPES, 10-320 mM NaCl, pH 7, $K_{d-10} \approx 0.7 \mu\text{M}$ and $K_{d-320} \approx 303 \mu\text{M}$, determined by isothermal titration calorimetry [156]

In summary, the neomycin-aptamer is a robust aptamer that binds neomycin under various buffer conditions. The presence of the functional aptamer-binding pocket is indicated by an increased melting temperature upon neomycin-binding. Thus, neomycin is a suitable candidate for aptamer engineering.

5.2.2 Determination of the Melting Temperature

Due to the SELEX-process, aptamers usually consist of one oligonucleotide strand. The denaturation of the oligonucleotide induces a change within the structure, which was described by a monomolecular reaction type:



The temperature dependent transition from the native to the denatured state is observed by the change in absorbance at 260 nm, which is represented by a characteristic sigmoidal curve progression (Figure 5.3). The optimal absorbance for the measurement of melting temperatures is ≈ 0.4 a.u., which corresponds to an oligonucleotide concentration in the low micromolar range. [161] In the following, one forward and the corresponding reverse cycle of the temperature dependent UV/Vis-absorbance measurements is shown.

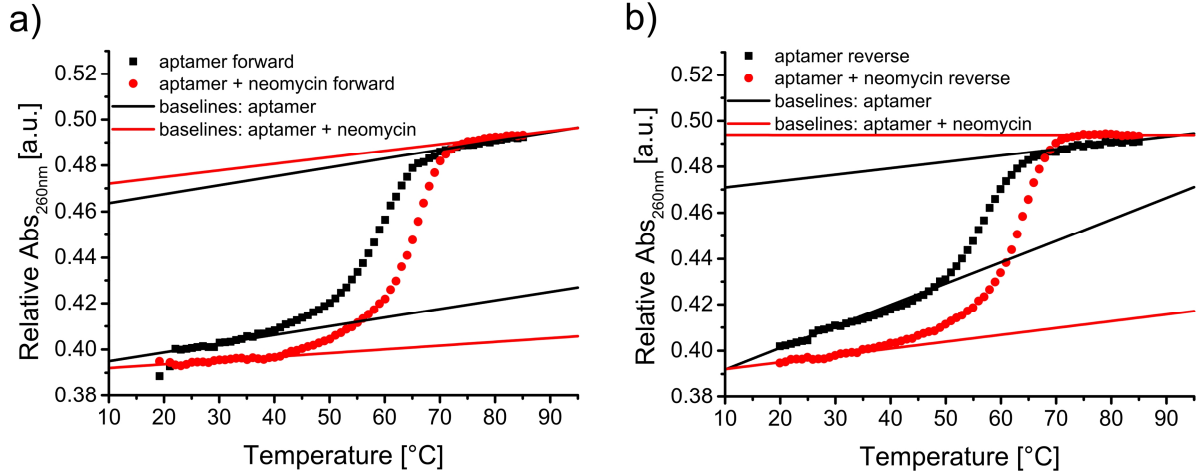


Figure 5.3: Relative absorbance of the neomycin-aptamer at 260 nm versus the temperature. The data of one measurement is shown for the forward (a) and the reverse cycle (b) for the aptamer (black squares) and the aptamer with neomycin (red dots). The baselines define the areas, which represent the native and the denatured state.

Assuming a two-state model, composed of only a native and a denatured state, the absorbance melting-curve can be transformed into a fraction folded versus temperature plot. [162] The temperature dependent transition from a native to a denatured oligonucleotide can be described by the following equation:

$$A(T) = (1 - \alpha(T))A_n(T) + \alpha A_d(T) \quad (5.3)$$

with the fraction folded ($\alpha(T)$), the UV absorbance ($A(T)$) and the absorbance values of the native- ($A_n(T)$) and denatured ($A_d(T)$) property. In order to obtain the values of $A_n(T)$ and $A_d(T)$, the lower (native oligonucleotide) and upper baseline (denatured oligonucleotide) were determined by a linear fit:

$$A_d(T) = A_d^0 + m_d T \quad (5.4)$$

$$A_n(T) = A_n^0 + m_n T \quad (5.5)$$

with the y-axis intercepts A_d^0 and A_n^0 , the slope of the lines m_d and m_n and the temperature T (Figure 5.3). The insertion of equations 5.4 and 5.5 into equation 5.3 results in the following equation:

$$\alpha = \frac{A(T) - A_n^0 + m_n T}{A_d^0 + m_d T - A_n^0 + m_n T} \quad (5.6)$$

The melting temperature is per definition the temperature at a fraction folded of $\alpha = 0.5$. To access the melting point, the fraction folded versus temperature plot is fitted with a sigmoidal function:

$$y = \frac{A_1 - A_2}{1 + e^{\frac{(T-T_m)}{d}}} + A_2 \quad (5.7)$$

with the initial value ($A_1 = 1$), the final value ($A_2 = 0$), the temperature (T) melting temperature (T_m) and a parameter that is a measure of the slope of the transition regime (d).

The fit provided a melting temperature (with standard deviation) of the aptamer of 58.0 ± 0.2 °C (forward) and 57.6 ± 0.1 °C (reverse). The melting temperature was increased to 64.1 ± 0.2 °C (forward) and 62.7 ± 0.1 °C (reverse) for the aptamer at a neomycin concentration of $10 \mu\text{M}$ (Figure 5.4). The results showed an increase in the melting temperature of ≈ 6 °C upon neomycin-binding. This temperature shift is in the order of magnitude of the results published by Stampfl and coauthors. At a NaCl concentration of 80 mM, they recorded a temperature shift of ≈ 10 °C and they could not observe a temperature shift at a NaCl concentration of 120 mM. [54] Most likely the melting temperature at a NaCl concentration of 100 mM is between the melting temperature, measured at the NaCl concentrations of 80 and 120 mM.

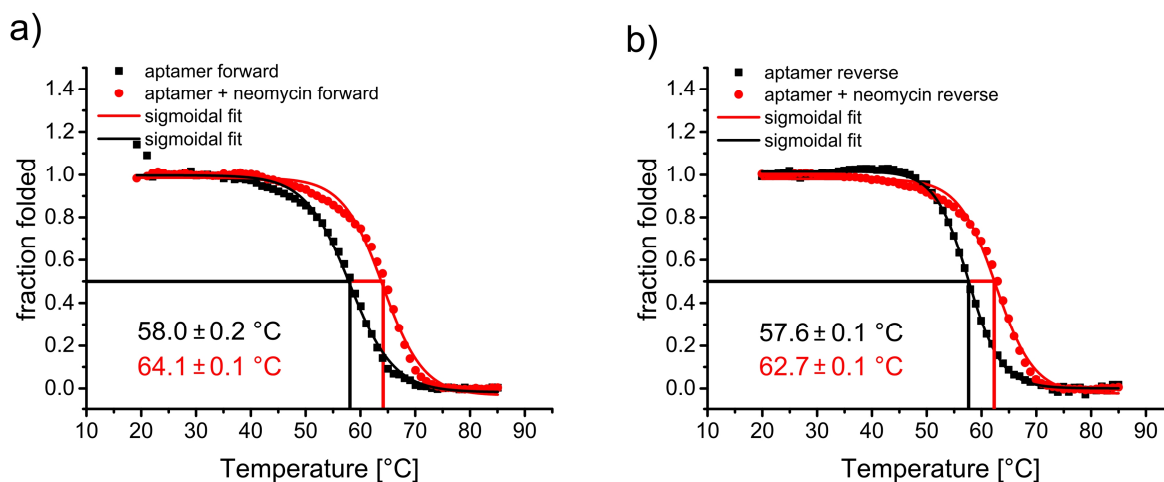


Figure 5.4: Fraction folded versus temperature plot: a) for the aptamer and b) the aptamer with added neomycin ($10 \mu\text{M}$). The sigmoidal fit provides the melting temperature (T_m).

The mean value of three independent measurements is a melting temperature of 57.7 ± 0.9 °C without neomycin and of 63.5 ± 0.9 °C with added neomycin. Thus, the melting temperature is a robust measure, which indicates successful neomycin-binding. The reported error of the melting temperature is in the range of 1-2 °C. [161]

5.2.3 Van't Hoff Analysis

In order to access information about the standard entropy (ΔS°), standard enthalpy (ΔH°) and free Gibbs enthalpy (ΔG°) of the aptamer, a van't Hoff analysis can be performed. At constant temperature, the change in free energy (ΔG°) can be related to the enthalpy and entropy changes:

$$\Delta G^\circ = \Delta H^\circ - T\Delta S^\circ \quad (5.8)$$

with the temperature (T in K), the standard enthalpy of the reaction (ΔH° in kJ mol^{-1}) and the standard entropy (ΔS° in kJ mol^{-1}). The relation of the free energy with the association constant (K_a) is given by the following equation:

$$\Delta G^\circ = -RT \ln \frac{K_a}{c^\circ} \quad (5.9)$$

with the standard reference concentration ($c^\circ = 1 \text{ mol/L}$) and the molar gas constant (R in $\text{J mol}^{-1} \text{ K}^{-1}$). In case the temperature is varied, as in temperature dependent UV/Vis-absorbance experiments, the change in free energy can be written:

$$\frac{\partial}{\partial T} \left(\frac{\Delta G^\circ}{T} \right) = -R \left(\frac{\partial \ln \frac{K_a}{c^\circ}}{\partial T} \right) \quad (5.10)$$

Assuming that ΔH° is independent of temperature, equation 5.9 can be rewritten:

$$\frac{\partial}{\partial T} \left(\frac{\Delta G^\circ}{T} \right) = \frac{-\Delta H^\circ}{T^2} \quad (5.11)$$

The combination of the equations 5.10 and 5.11 gives the van't Hoff equation:

$$\Delta H^\circ = RT^2 \left[\frac{\partial \ln \frac{K_a}{c^\circ}}{\partial T} \right] \quad (5.12)$$

The calculation provides estimates of the standard entropy, the standard enthalpy and the free Gibbs energy.

The reaction-type of the oligonucleotide-denaturation has a strong influence on the calculated values of the standard entropy (ΔS°), the standard enthalpy (ΔH°) and the free Gibbs enthalpy (ΔG°) of the aptamer. For the van't Hoff calculations, reaction-types are used, which consist of one reaction step. The latter is characterized by two possible states of oligonucleotide conformations: the native and the denaturated state. According to literature, the two-state assumption is only valid for oligonucleotides that do not form intermediates or alternative hybridization constructs during the melting process. [54, 146, 161, 163] Additionally it has been reported that sequences with more than 12 bp usually do not follow the two state assumption. [164]

A way to validate, whether intermediates are built, is to estimate the thermodynamic parameter ΔH° by two routes that are both based on the van't Hoff analysis. ΔH° values determined by both methods with a difference of less than 15 % indicate the absence of intermediates. [54, 146]

Melting processes, starting at the oligonucleotide ends or at the internal loop (Figure 5.5a) cause intermediates. Additionally, the presence of fully or partially bound analytes (Figure 5.5c and d) increases the possible number of intermediates and thereby the width of the melting transition. Thus, it is conceivable that the two-state assumption may not account for aptamers.

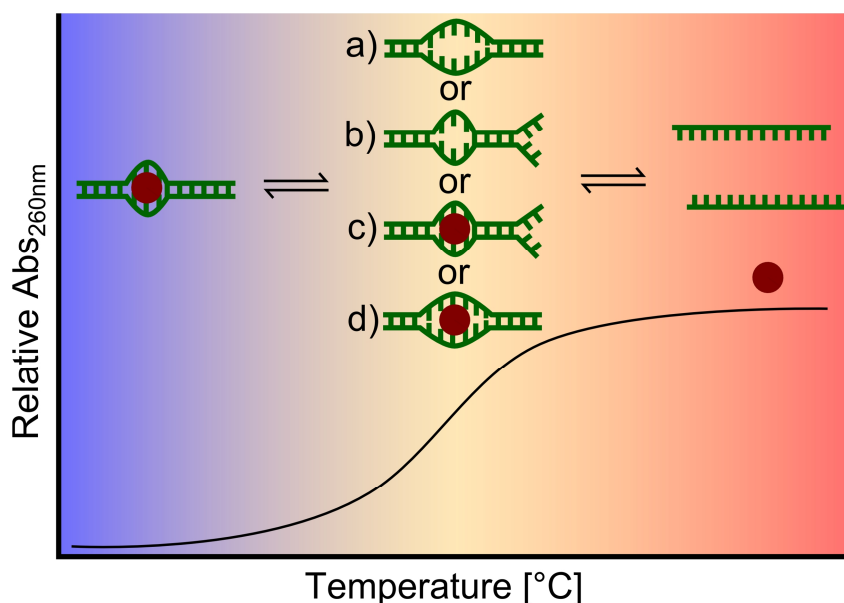


Figure 5.5: Schematic of the two-state melting process with possible intermediate structures of oligonucleotides, exhibiting a binding-site for one analyte (a-d).

5.2.3.1 Slope-based van't Hoff analysis

One route allows the calculation of ΔH° by the slope of the fraction folded form at the melting temperature. The slope can be calculated by the first derivative of equation 5.7: [52, 165]

$$\frac{d\alpha(T)}{dT} = \frac{(A_2 - A_1) e^{\frac{(T-T_m)}{d}}}{d \left(e^{\frac{(T-T_m)}{d}} + 1 \right)^2} \quad (5.13)$$

The slope ($d\alpha/dT$) of the melting transition (Figure 5.4) is calculated for $T = T_m$:

$$\frac{d\alpha(T)}{dT} = \frac{(A_2 - A_1) e^{\frac{(T-T_m)}{d}}}{d \left(e^{\frac{(T-T_m)}{d}} + 1 \right)^2} = \frac{(A_2 - A_1)}{4d} \quad (5.14)$$

The association constant (K_a) can be described in terms of the folded fraction:

$$K_a = \frac{[A_d]}{[A_n]} = \frac{\alpha}{(1 - \alpha)} \quad (5.15)$$

The substitution into the van't Hoff equation gives:

$$\Delta H^\circ = RT^2 \frac{\partial}{\partial T} \left[\ln \left(\frac{\alpha}{1 - \alpha} \right) \right] = RT^2 \left(\frac{2}{1 - \alpha} \right) \frac{\partial \alpha}{\partial T} \quad (5.16)$$

At the melting temperature, ΔH° is:

$$\Delta H^\circ = 4RT_m^2 \left(\frac{\partial \alpha(T)}{\partial T} \right)_{T=T_m} \quad (5.17)$$

The error of ΔH° was calculated by means of a propagation of uncertainty:

$$\Delta(\Delta H^\circ) = \sqrt{\left(8 \left(\frac{\partial \alpha(T)}{\partial T} \right) RT \Delta T \right)^2 + \left(4RT^2 \Delta \left(\frac{\partial \alpha(T)}{\partial T} \right) \right)^2} \quad (5.18)$$

The results of the forward cycle indicated a decrease of the free enthalpy from -225.3 ± 9.6 kJ/mol to -256.0 ± 11.1 kJ/mol (Table 5.1). In contrast, the free enthalpy increased in the reverse cycle from -299.6 ± 6.4 kJ/mol to -270.4 ± 10.3 kJ/mol, which was caused by a narrower melting transition of the aptamer system (Figure 5.4b). The difference between the forward and the reverse cycle was the denaturation- and hybridization-time. The forward cycle was performed with oligonucleotides, which were denaturated for 3 minutes at 90 °C and hybridized for 60 minutes at 20 °C. In the melting experiment, these oligonucleotides were denaturated with a rate of 1 °C per minute. The reverse cycle started with denaturated oligonucleotides at 80°C with a cooling rate of 1 °C per minute. Possibly, the structures of the oligonucleotides in the transition regime were slightly different. An explanation for the narrower melting transition could be a smaller number of intermediate structures compared to the results of the forward cycle or inhomogeneities of the melting curves.

Table 5.1: Thermodynamic parameter calculated according to the slope-based van't Hoff analysis.

	forward				reverse			
	aptamer		Aptamer + neomycin		aptamer		Aptamer + neomycin	
ΔH°	-225.3 ± 9.6	kJ/mol	-256.0 ± 11.1	kJ/mol	-299.6 ± 6.4	kJ/mol	-270.4 ± 10.3	kJ/mol
ΔS°	-680.3 ± 29.0	J/mol	-759.1 ± 33.1	J/mol	-906.0 ± 19.4	J/mol	-805.4 ± 30.7	J/mol
ΔG°	-14.3 ± 0.6	kJ/mol	-20.6 ± 0.9	kJ/mol	-18.6 ± 0.4	kJ/mol	-20.7 ± 0.8	kJ/mol

The obtained ΔH° can be used to estimate ΔS° and ΔG° at the temperature of interest. Usually the physiological most relevant temperature of 37 °C (= 310.15 K) is chosen. The Gibbs free energy is calculated according to $\Delta G_{37}^\circ = \Delta H^\circ - (310.15 \Delta S^\circ)$ with $\Delta S^\circ = \Delta H^\circ / T_m$. The same trend as for the calculation of ΔH° holds true for the calculated entropy of the forward and reverse cycle. A decrease in

the entropy may be the result of a neomycin molecule inside the binding pocket, which restricts fluctuations within the nucleotides of the aptamer. An increase in the entropy could be the result of the water molecules, which were released upon neomycin binding. [166] In contrast to the ΔH° and ΔS° values, the ΔG° values decreased for both measurements with added neomycin. However, the difference in ΔG° caused by neomycin, which was calculated according to equation 5.19, is smaller in the reverse cycle ($\Delta G_{\text{reverse}}^\circ \approx 2.1$ kJ/mol) compared to the forward cycle ($\Delta G_{\text{forward}}^\circ \approx 6.3$ kJ/mol).

$$\Delta\Delta G_{37}^\circ = \Delta G_{\text{neomycin}}^\circ - \Delta G_{\text{aptamer}}^\circ \quad (5.19)$$

Furthermore, the choice of the upper and lower baseline has an influence on the calculated parameters ΔH° , ΔS° and ΔG° . To compensate for inhomogeneities of the melting curves and corresponding outliers of the calculated parameters, the mean values of three measurements including the forward and the reverse cycles were calculated. The stabilization of the aptamer upon analyte-binding was confirmed by a decrease of ΔH° , ΔS° and ΔG° (Table 5.2).

Table 5.2: Mean thermodynamic values of three measurements, determined by the slope based van't Hoff analysis.

	aptamer		aptamer + neomycin	
ΔH°	-250.5 ± 25.4	kJ/mol	-275.2 ± 9.7	kJ/mol
ΔS°	-757.1 ± 77.5	J/mol	-817.6 ± 29.4	J/mol
ΔG°	-15.7 ± 1.5	kJ/mol	-21.7 ± 1.0	kJ/mol

5.2.3.2 Linear van't Hoff Fit

In order to verify, whether melting followed a two-state model, another approach for the calculation of the thermodynamic parameter ΔH° , ΔS° and ΔG° was chosen. The Gibbs free energy is written according to equations 5.8 and 5.9. Following, the natural logarithm of the affinity constant ($\ln(K_a)$) is plotted against the reciprocal of the temperature ($1/T$), which is referred to as van't Hoff plot (Figure 5.6):

$$\ln\left(\frac{K_a}{c^\circ}\right) = -\frac{\Delta H^\circ}{R} \left[\frac{1}{T} + \frac{\Delta S^\circ}{R} \right] \quad (5.20)$$

In the analyzed interval of data points ($0.15 < \alpha < 0.85$), the van't Hoff plot ideally follows a linear dependency. The linear fit provides the slope ($m = -\Delta H^\circ/R$) and the Y-axis intercept ($b = \Delta S^\circ/R$). According to literature, the interval $0.15 < \alpha < 0.85$ is most precise, because it covers the transition melting regime. [146]

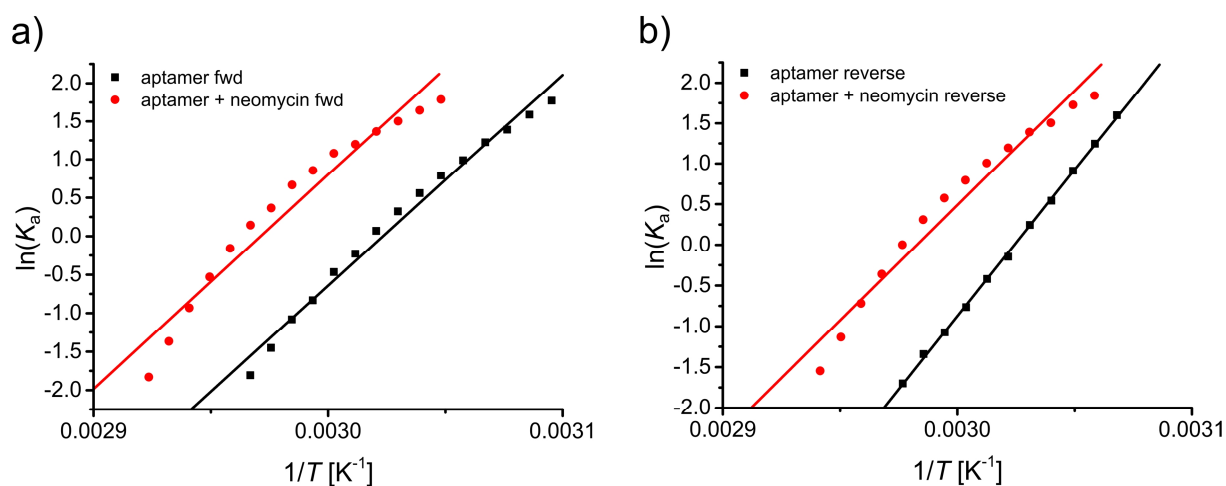


Figure 5.6: The plot of the natural logarithm of the association constant versus the reciprocal of the temperature ideally gives a linear dependency. The van't Hoff plot of the aptamer (black squares) and the aptamer with added neomycin (red dots) of the forward (a) and the reverse (b) cycle are shown.

Table 5.3: Thermodynamic parameters of the aptamer and the aptamer with neomycin, for the forward and the reverse cycle.

	forward		reverse	
	aptamer	aptamer + neomycin	aptamer	aptamer + neomycin
ΔH°	-228.7 ± 7.4 kJ/mol	-231.7 ± 14.7 kJ/mol	-299.0 ± 2.5 kJ/mol	-235.3 ± 13.1 kJ/mol
ΔS°	-691.5 ± 22.4 J/mol	-688.5 ± 43.9 J/mol	-904.2 ± 7.7 J/mol	-701.9 ± 39.3 J/mol
ΔG°	-14.2 ± 0.9 kJ/mol	-18.2 ± 0.9 kJ/mol	-18.5 ± 0.3 kJ/mol	-17.6 ± 2.0 kJ/mol

In this example of melting curves, only the data points of the reverse aptamer measurement followed a linear dependency (Figure 5.6b). The other data points had a curved shape (Figure 5.6). Consequently, the ΔH° value of the forward aptamer measurement was with -228.7 ± 7.4 kJ/mol smaller than for the reverse measurement with -299.0 ± 2.5 kJ/mol (Table 5.3 line three). The ΔH° values for the forward and the reverse cycle of the measurement at a neomycin concentration of 10 μ M differed by 1.5 % (Figure 5.6).

The mean values of three independent measurements for the ΔH° value were calculated (Table 5.4). In comparison to the results of the previously presented forward and reverse measurement, the mean value of three measurements at the presence of neomycin differed by ≈ 6 %. The mean ΔH° value of three measurements without neomycin differed by ≈ 9 % and ≈ 19 % from the result of the forward and the reverse cycle, respectively. The mean ΔS° value of the measurement with aptamer differed by ≈ 9 % and ≈ 19 % from the result of the forward and the reverse cycle, respectively. The mean ΔS° value differed by 9 % and 5 % for the measurement with added neomycin for the forward and the reverse measurement.

Table 5.4: Mean thermodynamic values of three measurements, determined by the linear van't Hoff plot.

	aptamer		aptamer + neomycin	
ΔH°	-251.3 ± 24.3	kJ/mol	-247.1 ± 11.0	kJ/mol
ΔS°	-760.5 ± 73.9	J/mol	-735.4 ± 33.1	J/mol
ΔG°	-15.5 ± 1.5	kJ/mol	-19.1 ± 1.0	kJ/mol

A parameter, which is a measure of stability is ΔG_{37}° . Equation 5.19 was applied to calculate the $\Delta\Delta G_{37}^\circ$ value, which describes the change in the Gibbs energy upon binding of neomycin to the aptamer. For the forward reaction, $\Delta\Delta G_{37}^\circ$ decreased by ≈ 4 kJ/mol and increased by ≈ 1 kJ/mol for the reverse reaction. The mean value of three independent measurements for the thermodynamic parameter ΔG_{37}° revealed a decrease from -15.5 ± 1.5 kJ/mol to -19.1 ± 1.0 kJ/mol upon neomycin-binding (Table 5.4). The $\Delta\Delta G_{37}^\circ$ of ≈ 3.6 kJ/mol would correspond to a K_d value of 250 mM. Assuming the K_d value of 1 μ M, which is reported in literature, a change in $\Delta\Delta G_{37}^\circ$ of 35.7 kJ/mol would have been expected according to the equation:

$$\Delta G_{37}^\circ = RT \ln(K_d/c^\circ) = 8.319 \text{ J/molK} * 310.15 \text{ K} * \ln(1\text{E-}6\text{M}/1\text{M})$$

A comparison of the $\Delta\Delta G_{37}^\circ$ values with literature is partly possible, because Stampfl et al. reported the thermodynamic parameter only for the buffer containing 10 mM NaCl. In those buffer conditions, the shift in the melting temperature was ≈ 29 °C at a neomycin concentration of 5 μ M. The larger temperature shift upon neomycin-binding in buffer, containing 10 mM NaCl, might be explained by a favored binding of neomycin. In the latter buffer, a smaller amount of positively charged Na^+ -ions shield the negatively charged phosphate backbone compared to measurements in buffer, containing 100 mM NaCl. The negatively charged phosphate backbone is part of the binding pocket, which attracts the positively charged neomycin molecule. Stampfl et al. reported a $\Delta\Delta G_{37}^\circ$ value of 34.3 kJ/mol for the measurement at a Na^+ -ion concentration, which corresponded to a K_d of 1.7 μ M. The authors did not mention the $\Delta\Delta G_{37}^\circ$ at a Na^+ -ion concentration of 100 mM. As their measured melting temperatures at 80 mM NaCl were similar to the melting temperature measured in this study, also a similar $\Delta\Delta G_{37}^\circ$ could be assumed. The dissociation constant is dependent on the concentration of mono- and divalent-ions. For the neomycin-aptamer, a dissociation constant of ≈ 7 μ M is reported at a NaCl concentration of 100 mM. Additionally, two low-affinity binding-sites for neomycin were reported in literature, with dissociation constants of ≈ 70 μ M and ≈ 90 μ M. A reason for the discrepancy between the calculated and expected $\Delta\Delta G_{37}^\circ$ values could be an improper assumption of the two-state model.

5.2.3.3 Comparison of Both van't Hoff Calculations

In order to verify, whether melting followed a two-state model, the results of both approaches for the calculation of the thermodynamic parameter ΔH° , ΔS° and ΔG° were compared. The calculated ΔH° values for the aptamer in absence of neomycin were similar within up to $\approx 1.5\%$ deviation, regardless of the slope-based (Table 5.1) or the linear van't Hoff plot (Table 5.3). This accounted for the single forward- and reverse cycle as well as for the mean value of three measurements. The result consolidated the assumption of a two-state transition from the native to the denaturated state. The calculated ΔH° values for the measurements with added neomycin were up to $\approx 15\%$ lower in the case of the linear van't Hoff plot, compared to the slope-based van't Hoff analysis. Thus, the difference in ΔH° values might indicate the presence of intermediates.

In literature, analyte-binding oligonucleotides were reported, which show the same shift in the melting temperature regardless the NaCl concentration (in a certain range). For example, temperature dependent UV/Vis-absorbance measurements were performed with a DNA in the presence and the absence of the antibiotic analyte chartreusin. The shift in the melting temperature upon binding of chartreusin was $\approx 3.5^\circ\text{C}$ at NaCl concentrations from 8 mM to 120 mM. Chartreusin is, in contrast to neomycin, not positively charged and the binding-process includes intercalation and minor groove binding. [167] Oligonucleotides are negatively charged macromolecules with one negatively charged phosphate-group per nucleotide. The condensation of counter ions onto the oligonucleotide is important for the formation of the structure. [149] It was shown that the melting temperature of oligonucleotides depends linearly on the logarithm of the Na^+ -ion concentration. [168] The binding process of ligands is entropically supported by the release of counter ions:



A larger number of positively charged groups and a larger size of the analyte, favors binding at the phosphate backbone, which leads to the release of a larger number (n) of counter ions (M^+). The counter ion release is consequently smaller in the case of chartreusin-binding compared to neomycin-binding. This explains why the shift in the melting temperature upon neomycin-binding is depending on the NaCl concentration. Additionally, the positively charged neomycin might bind to the single-stranded oligonucleotides or at a different binding-site of the native aptamer. [54, 169]

In summary, a two-state assumption cannot be considered for oligonucleotides with a binding-site for analytes. Thus, the calculation of the thermodynamic parameter ΔH° , ΔS° and ΔG° from the results of temperature dependent UV/Vis-absorbance measurements is not precise. Nevertheless, the measurements presented in this work, were performed at a neomycin concentration of 10 μM . At this concentration, a shift in the melting temperature was observed, which proved the functionality of the binding pocket.

5.2.3.4 Errors and Assumptions

The previously described calculations contain additional assumptions that might have had influenced the calculated data. [170] The choice of baselines is often mentioned as error source. [164] In principle the choice of the baseline might be problematic, in case the melting temperature is close to the starting- or the end-temperature of a melting curve. In those cases there are only a few data-points available for the definition of the baselines, which occurred for the aptamer measurement in this work. Furthermore, the temperature dependencies of ΔH° and ΔS° were ignored.

$$\Delta H^\circ(T) = \Delta H_{T_0}^\circ - \Delta C_p^0 (T - T_0) \quad (5.22)$$

$$\Delta S^\circ(T) = \Delta S_{T_0}^\circ - \Delta C_p^0 \ln(T/T_0) \quad (5.23)$$

The heat capacity (ΔC_p^0) was not zero as assumed, because of π - π stacking interactions between the nucleotides. Accurate values for ΔC_p^0 could be calculated with calorimetric methods. It has been shown that the error arising by neglecting ΔC_p^0 , is rather small compared to the systematic errors arising by fitting the melting curves. Schroeder et al. claimed that still a reliable value for ΔG° can be extrapolated. [161]

In summary, the estimation of ΔH° , ΔS° and ΔG° values by means of UV/Vis melting experiments is possible for complementary oligonucleotides. Nevertheless, only a qualitative comparison is advisable and the results should be handled with caution. Therefore, the calculation of the thermodynamic parameters ΔH° , ΔS° and ΔG° is not justified for the aptamer featuring an internal loop as binding-site for neomycin. Nevertheless, the results suggest that neomycin-binding is indicated by an increased melting temperature in the chosen buffer (20 mM phosphate, pH of 7, 100 mM NaCl). This makes the melting temperature to the most reliable value, extracted from temperature dependent UV/Vis-absorbance measurements. Thus, for the combined oligonucleotides, only the melting temperatures were compared.

5.3 Hg²⁺-Binding DNA

5.3.1 Structure of the Hg²⁺-Binding DNA

The Hg²⁺-binding DNA consists of two DNA-strands that are complementary, except for a thymine-thymine mismatch. The latter is the binding-site for one Hg²⁺-ion. The binding-site can be multiplied within the DNA-strand neighboring or randomly distributed, which results in a larger difference in the thermal stability from the unbound to the analyte bound state. The Hg²⁺-binding DNA used here has two T-T-mismatches, which led to a shift in the melting temperature of 29 °C at a Hg²⁺-concentration of 2 μ M, in accordance with literature (Figure 5.7).

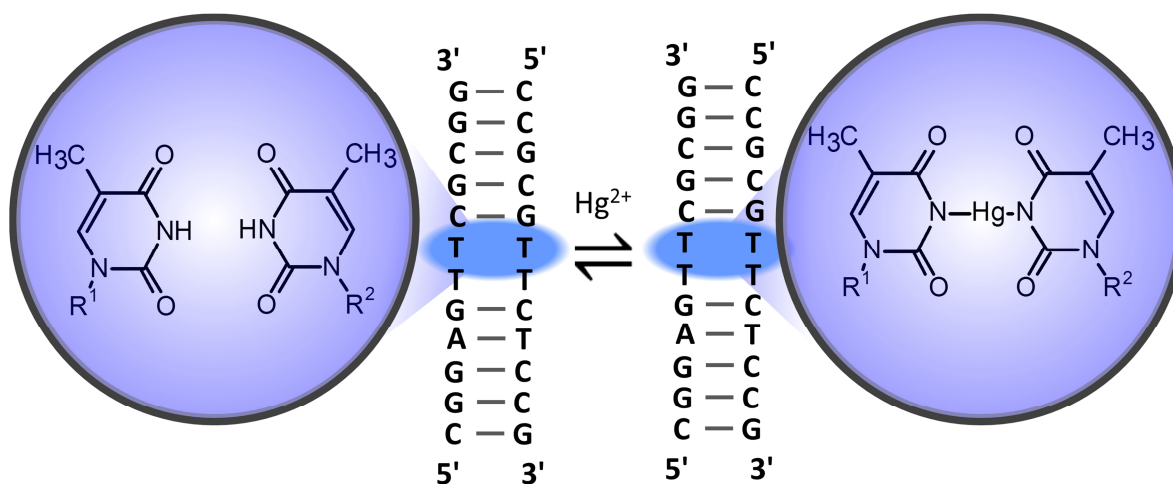


Figure 5.7: Schematic of the Hg^{2+} -binding DNA. The Hg^{2+} -ion is bound inside a thymine-thymine mismatch. The presented sequence features two binding-sites (two T-T mismatches).

The detection of Hg^{2+} is of great importance, because Hg^{2+} -ions are highly toxic. [171] Especially the damaging effect of Hg^{2+} -ions on DNA has been reported. It is known that a neutral metallo-base pair is formed, consisting of one Hg^{2+} -ion and a thymine-thymine-mismatch. [172, 173] It has been reported that the T- Hg^{2+} -T bonds are thermally more stable than a Watson-Crick base pair, because the bond has both covalent and ionic character. [55, 174] The thymine-thymine mismatch can be considered as the binding-site with high selectivity for Hg^{2+} -ions. The specificity is given by the size of the mercury-ion, which fits exactly between the thymine bases with a N3-Hg(II) bond length of 2.04 Å and a N3-Hg(II)-N3-bond angle of 180°. [55] Other divalent ions like Cu^{2+} , Ni^{2+} , Pb^{2+} , Mg^{2+} , Ca^{2+} , do not bind to the binding pocket between the T-T-mismatch. The reported dissociation constants of a single binding-site of the Hg^{2+} -binding DNA are in the range of 1 μM – 2.4 μM .

1. 10 mM sodium-cacodylate buffer, 100 mM NaClO_4 , pH 6.8, 25 °C; $K_d \approx 2.4 \mu\text{M}$, determined by isothermal titration calorimetry (ITC) [55]
2. 10 mM sodium-cacodylate buffer, 100 mM NaClO_4 , pH 6.8, $K_d \approx 1 \mu\text{M}$, determined by isothermal titration calorimetry (ITC) [175]

Furthermore, the Hg^{2+} -binding-site was embedded in different DNA oligonucleotides as multiple binding-sites, and the ΔT_m values upon addition of Hg^{2+} -ions were reported:

3. 10 mM sodium cacodylate, 100 mM NaNO_3 , 10 mM $\text{Mg}(\text{NO}_3)_2$, Hg^{2+} 0 - 48 μM , pH 4-6; ΔT_m determined, but no K_d [176]
4. 10 mM sodium-cacodylate buffer and 100 mM NaClO_4 , 0 - 12 μM $\text{Hg}(\text{ClO}_4)_2$, pH 6.0; ΔT_m determined, but no K_d [58]

In summary, the Hg^{2+} -binding-DNA already exists in the split form and binds Hg^{2+} -ions under similar buffer conditions as the neomycin-aptamer binds neomycin. Furthermore, the presence of the

functional binding-site is indicated by an increased melting temperature upon Hg^{2+} -binding, which indicates a suitable candidate for the experimental approach presented in this work.

5.3.2 Determination of the Melting Temperature

Split-aptamers as well as the Hg^{2+} -binding DNA consist of two oligonucleotide strands and thus ideally follow a bimolecular reaction type with non-self-complementary oligonucleotides.



In analogy to monomolecular reactions, the thermodynamic parameter ΔH° , ΔS° and ΔG° can be calculated. For this reaction type, the total strand concentration (C_T) has to be determined from the absorbance of the denaturated oligonucleotides by means of Lambert-Beer's law. The extinction coefficient of the oligonucleotide is given by the supplier of the oligonucleotides. In analogy to the unimolecular reactions, the bimolecular reaction type is described by the following equations: [177]

$$K_a = \frac{\alpha \left(\frac{C_T}{2}\right)}{\left((1-\alpha) \left(\frac{C_T}{2}\right)\right)^2} = \frac{2\alpha}{C_T(1-\alpha)^2} \quad (5.25)$$

$$C_T = [A_1] + [A_2] + 2[A_3] \quad (5.26)$$

$$\Delta H^\circ = RT^2 \left(\frac{(1+\alpha)}{\alpha(1-\alpha)} \right) \frac{\partial \alpha}{\partial T} \quad (5.27)$$

$$\Delta H^\circ = 6RT_m^2 \left(\frac{d\alpha}{dT} \right)_{T=T_m} \quad (5.28)$$

The investigated Hg^{2+} -binding DNA sequence had two T-T-mismatches and consequently two Hg^{2+} -ions could bind to the binding-sites. The fraction folded versus temperature plot revealed an increase in the melting temperature upon Hg^{2+} -binding of 22 °C (Figure 5.8a). This temperature shift is in accordance with the results presented in literature for the same oligonucleotide. [58] The mean value of three measurements is a melting temperature of 39.2 ± 1.5 °C for the Hg^{2+} -binding-DNA, which was increased to 61.4 ± 1.0 °C upon Hg^{2+} -binding.

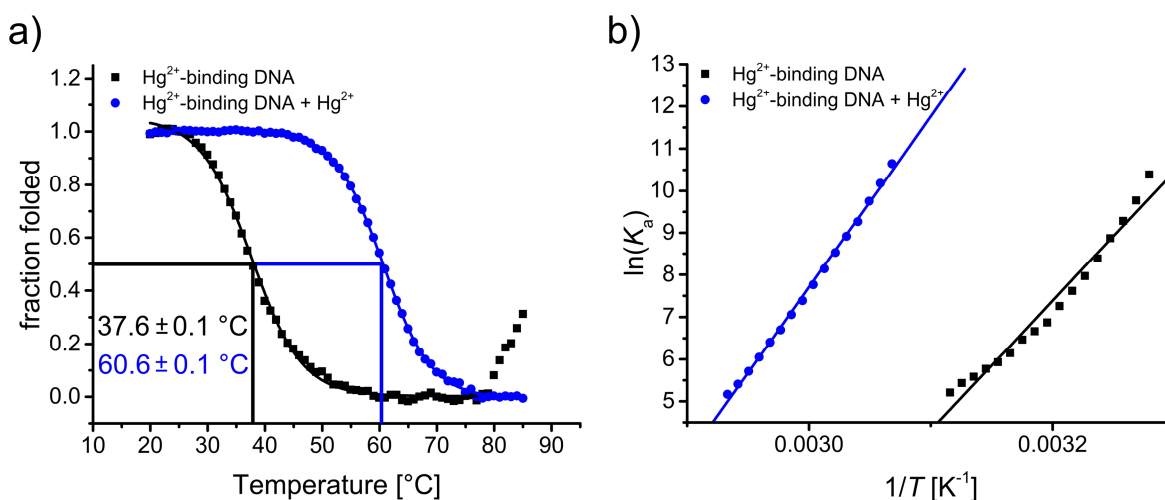


Figure 5.8: a) Fraction folded versus temperature plot of the original Hg^{2+} -binding DNA. b) Van't Hoff plot of the Hg^{2+} -binding DNA and the Hg^{2+} -binding DNA with added Hg^{2+} .

In order to test, whether the presence of intermediates also accounts for the Hg^{2+} -binding DNA, the ΔH° values obtained by both van't Hoff approaches were compared. The ΔH° values, calculated by means of the slope-based van't Hoff approach (Table 5.5) were only up to $\approx 7\%$ different from the values calculated by the linear van't Hoff fit (Figure 5.8b), which indicates the absence of intermediates.

Table 5.5: Thermodynamic data calculated for the Hg^{2+} -binding DNA

	Linear van't Hoff		Slope based van't Hoff	
	Hg^{2+} -binding DNA	Hg^{2+} -binding DNA + Hg^{2+}	Hg^{2+} -binding DNA	Hg^{2+} -binding DNA + Hg^{2+}
ΔH°	-255.2 ± 11.6 kJ/mol	-337.3 ± 4.6 kJ/mol	-272.7 ± 8.6 kJ/mol	-329.3 ± 2.9 kJ/mol

The mean value of ΔH° , given by three measurements, differed by $\approx 7\%$ depending, whether the linear van't Hoff or the slope-based approach was used (Table 5.6). Both approaches have in common that ΔH° , ΔS° and ΔG_{37}° decrease upon Hg^{2+} -binding. Here the $\Delta\Delta G_{37}^\circ$ values are with ≈ 22.9 kJ/mol and ≈ 23.9 kJ/mol closer to the expected value of 33.9 kJ/mol, which is calculated for a K_d of 2 μM . Also in this example, a reliable calculation of the thermodynamic parameters by means of the van't Hoff approaches was not conclusive. Nevertheless, Hg^{2+} -binding was detected at the buffer conditions by means of temperature dependent UV/Vis-absorbance measurements.

Table 5.6: Thermodynamic mean values calculated for the Hg²⁺-binding DNA by three measurements.

	Linear van't Hoff		Slope based van't Hoff		
	Hg ²⁺ -binding DNA	Hg ²⁺ -binding DNA + Hg ²⁺	Hg ²⁺ -binding DNA	Hg ²⁺ -binding DNA + Hg ²⁺	
ΔH°	-224.3 ± 35.8	-349.8 ± 13.5	-230.6 ± 43.5	-351.9 ± 18.9	kJ/mol
ΔS°	-652.1 ± 114.4	-983.2 ± 38.1	-681.1 ± 137.9	-994.8 ± 53.9	J/mol
ΔG°	-22.0 ± 1.1	-44.9 ± 1.8	-19.4 ± 1.4	-43.3 ± 2.3	kJ/mol

5.1 Theoretical Consideration for the Combination of two Different Binding-Sites

In order to see, which absorbance would be measured for a combination of the neomycin-aptamer with the Hg²⁺-binding DNA, the absorbance of one measurement of the neomycin-aptamer and the Hg²⁺-binding DNA were normalized, the sum was calculated and transferred into the fraction folded versus temperature plot. This calculated sum shows different fraction folded versus temperature profiles for the absorbance of the oligonucleotides with added analytes (Figure 5.9).

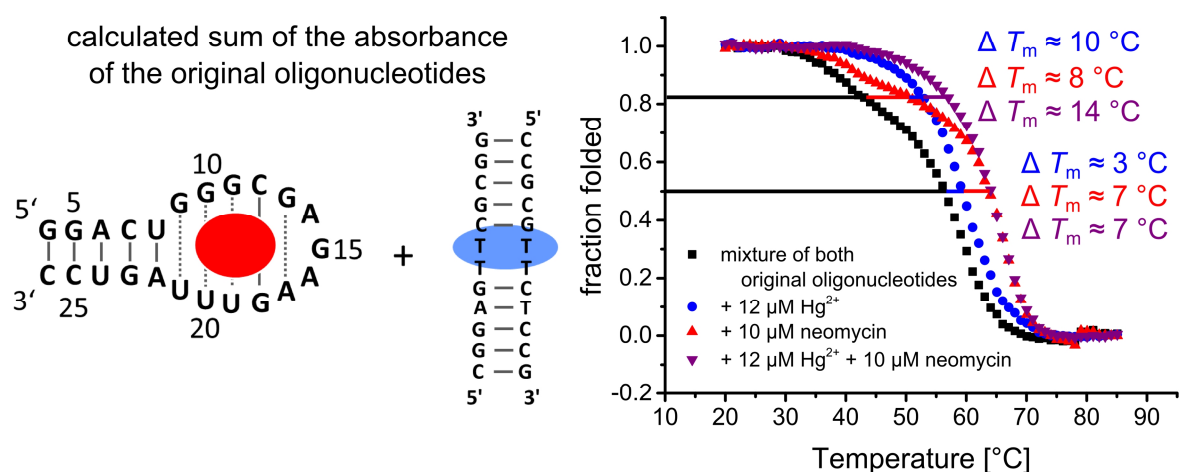


Figure 5.9: Theoretical consideration for the combination of the Hg²⁺-binding-DNA with the neomycin-aptamer. The absorbances of separated measurements, which were performed with the original aptamers, were added to estimate the outcome of an experiment with combined oligonucleotides.

The melting curve of the mixture of the original oligonucleotides shows a sigmoidal curve progression with an additional step at ≈ 42 °C, where ≈ 0.81 of the oligonucleotides are folded. The curve, resulting from the measurement with Hg²⁺-ions does not contain the additional step. The shifts in the melting temperatures for $\alpha = 0.81$ and $\alpha = 0.5$ were 10 °C and 3 °C, respectively. The curve, resulting from the measurement with neomycin does contain the additional step at $\alpha \approx 0.81$. The shifts in the melting temperatures for $\alpha = 0.81$ and $\alpha = 0.5$ were 8 °C and 7 °C, respectively. The curve

progression of the melting curves with added Hg^{2+} -ions and neomycin did not show the step at $\alpha \approx 0.81$. The shifts in the melting temperatures for $\alpha = 0.81$ and $\alpha = 0.5$ were $8\text{ }^\circ\text{C}$ and $7\text{ }^\circ\text{C}$, respectively. The shift in the melting temperature of $22\text{ }^\circ\text{C}$ of the original Hg^{2+} -binding-DNA was not reached, because the absorbance of the 12 nt long DNA is by a factor of two smaller. This is the result of an extinction coefficient, which is by a factor of two smaller. Thus, the absorbance of the neomycin-aptamer, covers the absorbance of the Hg^{2+} -binding-DNA. In summary, both analytes cause a shift in the melting temperature. In a combined aptamer, it is expected that every analyte contributes to the increase in the stability and no absorbance is covered. That is, because both strands are added at the same concentration. Before I elucidate the combination of both oligonucleotides in one construct, I discuss necessary control experiments to exclude crosstalk between the oligonucleotide-systems.

5.2 Control Experiments

5.2.1 Crosstalk: Unspecific Binding of Neomycin to the Hg^{2+} -Binding DNA.

In order to prove that binding of the positively charged analyte neomycin does not occur randomly on the negatively charged backbone of the Hg^{2+} -binding DNA, the effect of $10\text{ }\mu\text{M}$ neomycin on the melting temperature of the Hg^{2+} -binding DNA was investigated (Figure 5.10). For all control measurements, the previously described buffer composition was chosen (20 mM phosphate buffer, 100 mM NaCl, pH 7).

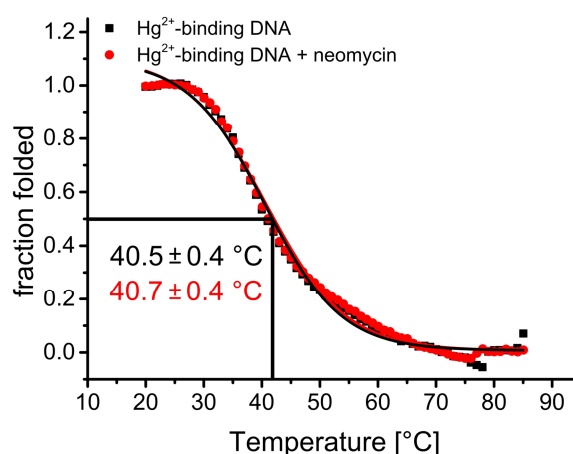


Figure 5.10: Fraction folded versus temperature plot of the Hg^{2+} -binding DNA, without and with neomycin ($10\text{ }\mu\text{M}$). The mean data points of three measurements were plotted.

The melting temperatures of the Hg^{2+} -binding DNA with and without added neomycin were both about $41\text{ }^\circ\text{C}$. Thus, no unspecific binding of neomycin to the Hg^{2+} -binding DNA could be detected by temperature dependent UV/Vis-absorbance measurements.

5.2.2 Does Splitting of the Neomycin-Aptamer Change its Functionality?

The use of the neomycin-aptamer in aptamer-engineering requires that the function of the binding pocket not be significantly affected upon splitting of the aptamer (Figure 5.11a). The structural information of the neomycin-aptamer, resolved by NMR, facilitated the identification of a splitting-position within the aptamer. The position between the bases A14 and G15 of the neomycin-aptamer was chosen, because both nucleotides are, according to literature, not involved in analyte binding. These bases build the terminal loop and do not stack with the neighboring bases. Then the split aptamer was connected to a fully complementary DNA 9mer, which had the sequence of the Hg^{2+} -binding-DNA without the T-T-mismatches (referred to as mutated Hg^{2+} -binding-DNA).

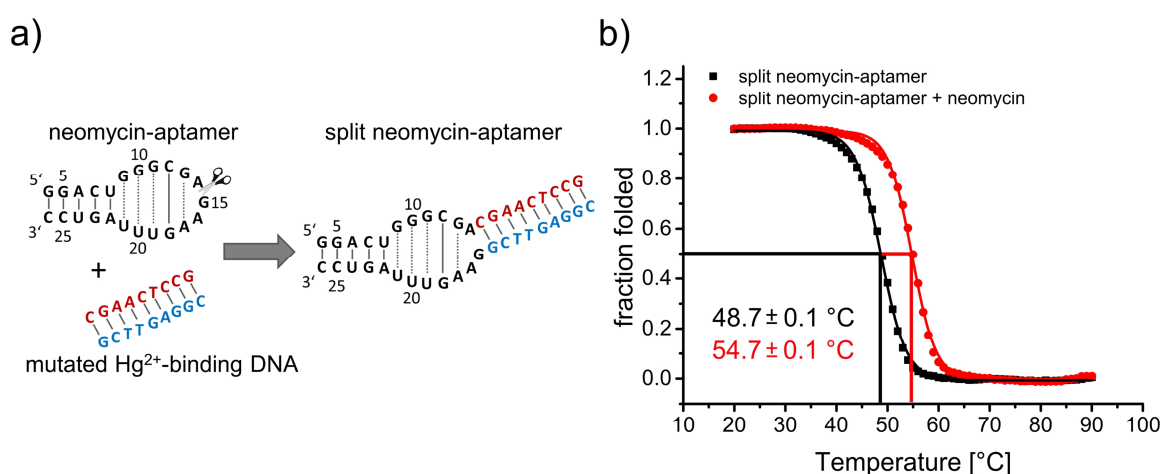


Figure 5.11: a) Scheme of the combination of the neomycin-aptamer with a complementary DNA (= mutated Hg^{2+} -binding-DNA). b) Fraction folded versus temperature plot of the split-neomycin-aptamer without and with added neomycin. The mean data points of three measurements were plotted.

The functionality of the split neomycin-aptamer was tested by means of temperature dependent UV/Vis-absorbance measurements (Figure 5.11b). The resulting melting temperatures were 48.7 ± 0.1 °C for the split aptamer and 54.7 ± 0.1 °C for the aptamer with added neomycin. Splitting of the aptamer resulted in a still functional neomycin-aptamer, which exhibited the same shift in T_m (= 6 °C) as the original neomycin-aptamer.

5.2.3 Crosstalk: Unspecific Binding of Hg^{2+} to the Split-Neomycin-Aptamer.

In order to verify that the positively charged Hg^{2+} -ions do not increase the melting temperature of the split neomycin-aptamer, temperature dependent UV/Vis-absorbance measurement were performed in the buffer: 20 mM phosphate buffer, 100 mM NaCl, pH 7. The melting temperature of the split neomycin aptamer was compared to the melting temperature of the split neomycin-aptamer at a concentration of 12 μM Hg^{2+} -ions. The plot of the fraction folded form versus temperature indicated a ≈ 1 °C lower melting temperature at the presence of 10 μM Hg^{2+} -ions (Figure 5.12). This shift is

caused by a broader melting transition, which could be the result of the adsorption of Hg^{2+} -ions on the negatively charged RNA. Possibly, some Hg^{2+} -ions replaced adsorbed Na^{+} -ions on the backbone of the oligonucleotide. The exchange of the ions might have caused the broader melting transition. The result confirmed that Hg^{2+} -ions do not increase the melting temperature of the split neomycin-aptamer, as would be the case for the addition of neomycin (Figure 5.12).

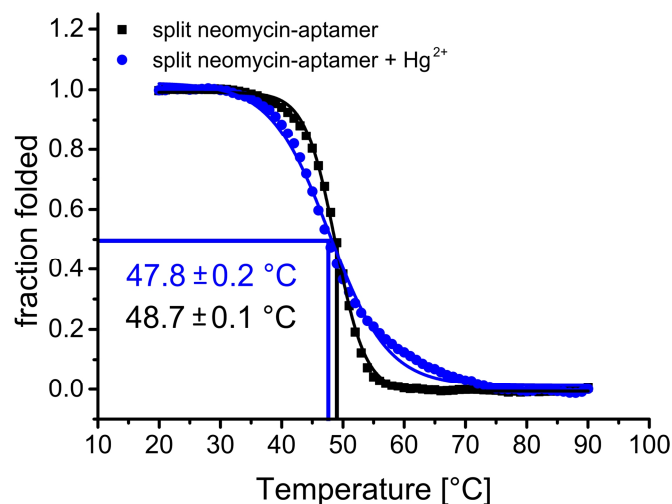


Figure 5.12: Fraction folded versus temperature plot of the split neomycin-aptamer with and without added Hg^{2+} -ions. The mean data points of three measurements were plotted.

5.3 Summary and Conclusion

The neomycin-aptamer and the Hg^{2+} -binding DNA were chosen as candidates for a combined construct. The functionality of the oligonucleotides was tested by means of temperature-dependent UV/Vis-absorbance measurements. As readout for a successful analyte-binding, an increase in the melting temperature was observed. Binding of neomycin was indicated by an increase in the melting temperature of 6 °C at a neomycin concentration of 10 μM . The Hg^{2+} -binding DNA had two T-T-mismatches and was characterized by an increase in the melting temperature of 23 °C at a Hg^{2+} -concentration of 12 μM . The results confirmed the functionality of both binding-sites in the same buffer: 20 mM phosphate buffer, 100 mM NaCl, pH 7. The difference in the ΔH° values, calculated by two van't Hoff approaches revealed that the dissociation of the neomycin-aptamer with added neomycin did not follow a two-state approach. Thus, unprecise thermodynamic parameter ΔH° , ΔS° and ΔG° were calculated. Consequently, the melting temperature, as robust parameter, was chosen as indicator to prove the functionality of the binding-sites.

It has been proposed to regard the dissociation of an analyte as a two-step process. [169] An increase in the melting temperature can be measured, in case the intermolecular interaction between the analyte and the binding-site are broken cooperatively with the other nucleotides (Figure 5.13a). Here analyte release and oligonucleotide-strand dissociation occur at the same time. It can be assumed

that this is the case, when the $\Delta G_{\text{analyte}}$ value, derived from the K_d of analyte-binding, is in agreement with the $\Delta\Delta G_{\text{oligo}}$ value, derived from the shift in the melting curve.

It is reasonable to presume that analytes do not necessarily leave the binding-sites cooperatively at the melting temperature of the oligonucleotides (Figure 5.13b). There, intermolecular interactions between the analytes and the oligonucleotides might brake step by step, resulting in a smaller or no shift in the melting temperature upon analyte-binding. In the case that the $\Delta G_{\text{analyte}}$ value and the $\Delta\Delta G_{\text{oligo}}$ value do not agree, the shift in the melting temperature cannot be correlated to the K_d of analyte-binding. This would explain, why only a few aptamers were reported in literature, which have an increased melting temperature upon analyte-binding.

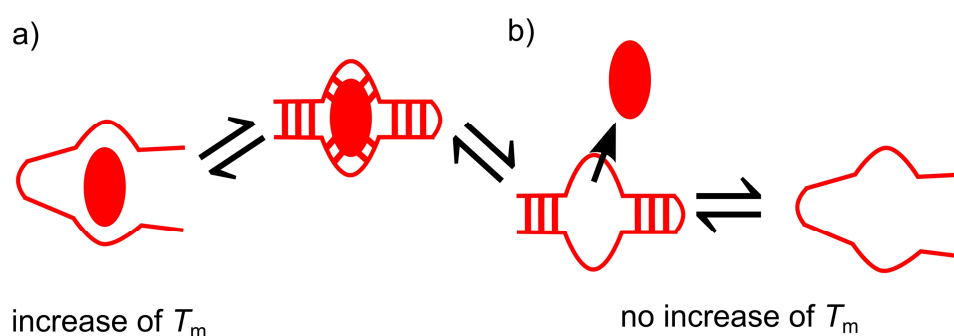


Figure 5.13: Schematic of two possible dissociation processes of the analyte from the binding-site in temperature dependent UV/Vis-absorbance measurements. a) The intermolecular interactions (red lines) between the analyte and binding-site as well as between the nucleotides are broken cooperatively. b) First the analyte is released and then the aptamer denatures.

A splitting position of the neomycin aptamer between the nucleotides A14 and G15 was identified. The disruption of the aptamer does not influence the neomycin-binding capability, which is indicated by an increase of $\approx 6^\circ\text{C}$ upon neomycin-binding. Consequently, the aptamer will be extended at A14 and G15 with DNA-sequences that facilitates Hg^{2+} -binding. The combined oligonucleotide will possibly increase the formation of intermediates, because the bulges are separated by less than 3 base pairs. In case no analytes are bound, the presence of one large internal loop is likely. The addition of one analyte or the other will lead to different intermediates. Depending on the temperature, at which the analytes dissociate, even more intermediates are possible. Thus, only the melting temperatures will be used as a measure of strand stability. In the following chapter I present the behavior of the combined oligonucleotides and elucidate the communication between both binding-sites.

6. Communication Between Binding-Sites

In this chapter the combination of oligonucleotides, which consist of a split neomycin-aptamer and a Hg^{2+} -ion binding DNA, is elucidated (Figure 6.1). Therefore, the neomycin-aptamer was split between the nucleotides 14 and 15 and three base pairs of the Hg^{2+} -binding DNA were removed (gray nucleotides in Figure 6.1). The nucleotides, which are located between the binding-sites, are referred to as communication module (green nucleotides in Figure 6.1). In a combined oligonucleotide, the melting temperature is strongly depending on the number of nucleotides on both ends of the oligonucleotide. I have designed one oligonucleotide, which fulfills this requirement with 5 bp on each end. This symmetrical frame of base pairs is necessary, because it ensures the stabilization of the binding-sites. Thus, it allows to determine the effect of the communication module on the binding-sites.

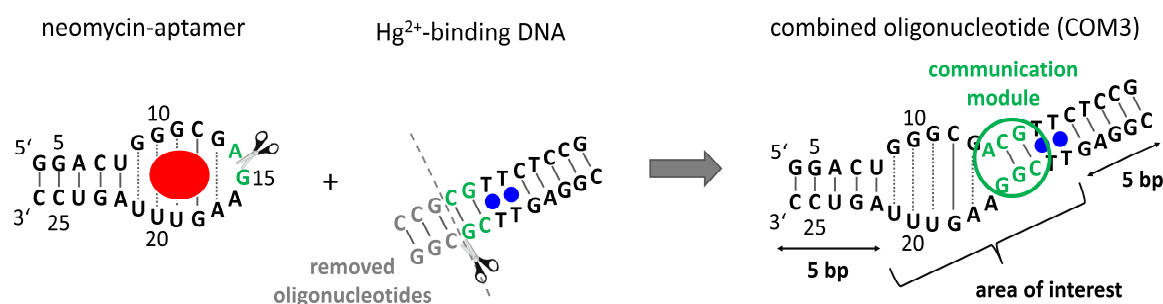


Figure 6.1: Schematic of the combination of the neomycin-aptamer with the Hg^{2+} -binding DNA to the COM3 construct.

I addressed the questions: Is the functionality of each binding-site affected in a combined structure with a communication module of 3 nt? Therefore, the functionality of the binding-sites was tested by means of temperature dependent UV/Vis-absorbance experiments in the presence of only neomycin molecules, only Hg^{2+} -ions and both analytes. In the following I tested, whether the construct can be characterized by allostery. Does binding of the first analyte influence binding of the second analyte? In order to maximize the allosteric effect, the length of the communication module was truncated from 3 to 1 nucleotide (Figure 6.2). The constructs are abbreviated with COM3 (3 nt), COM2 (2 nt) and COM1 (1 nt).

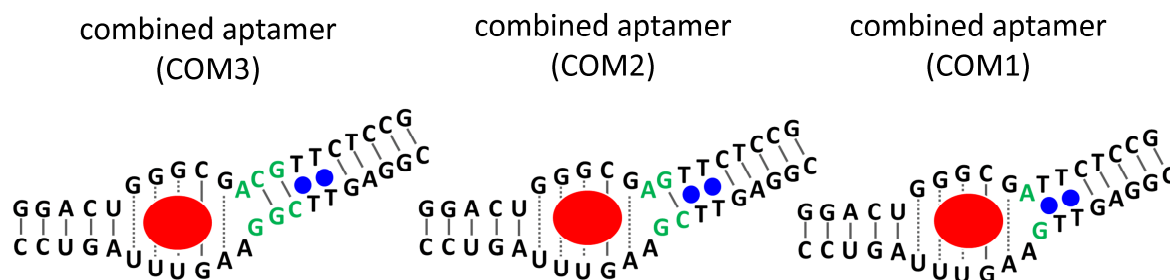


Figure 6.2: Investigated combined oligonucleotide structures. The communication module is highlighted in green.

6.1 Combined Split-Neomycin-Aptamer with a Hg^{2+} -Binding DNA

In order to calculate the melting temperature of the combined aptamers, the absorbance versus temperature profile was transformed into the percentage folded fraction versus temperature. Exemplarily, one forward and the corresponding reverse cycle of COM3 are shown, to highlight the effect of the analytes neomycin and Hg^{2+} on the thermal stability of the oligonucleotide (Figure 6.3).

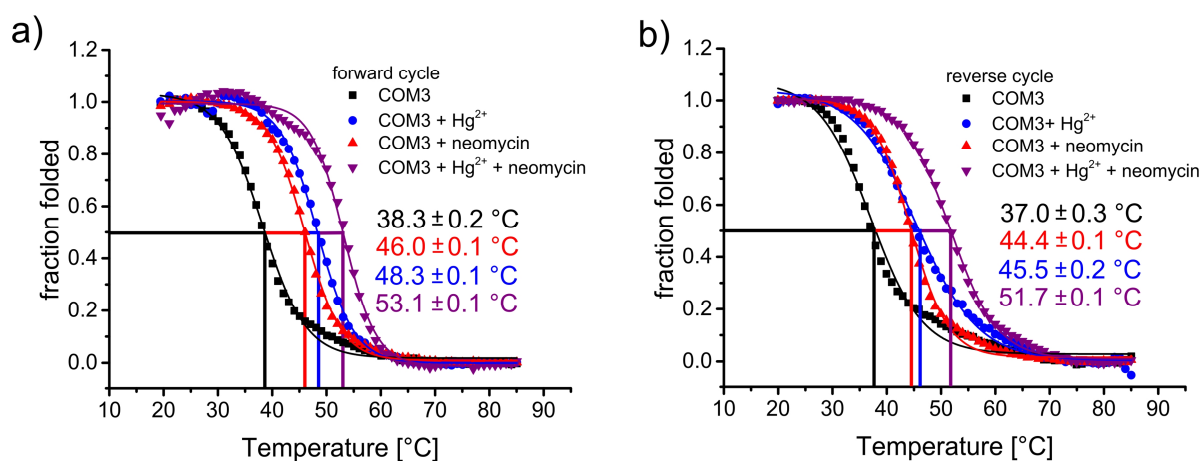


Figure 6.3: Fraction folded oligonucleotide versus temperature plot of COM3. The melting temperatures were determined by a sigmoidal fit.

At first I discuss the results of the forward cycle of the COM3 oligonucleotide. The fraction folded versus temperature plot revealed a melting temperature of 38.3 ± 0.2 °C for the aptamer without added analytes. At a Hg^{2+} concentration of 12 μM , the melting temperature increased by ≈ 10 °C. The shift in the melting temperature upon addition of Hg^{2+} -ions was approximately 2.3 times higher in the original Hg^{2+} -binding DNA than in the combined aptamer COM3. The truncation of the original Hg^{2+} -binding DNA duplex from 5 bp to 3 nucleotides in the combined aptamer COM3 could have reduced the effect of Hg^{2+} on the melting temperature. Possibly, binding of Hg^{2+} -ions to the binding-site requires further stabilization of the surrounding nucleotides. This hypothesis is in agreement with the

reported sensitivity of the Hg^{2+} -binding-site to the type of nucleotides flanking the binding-site. This so called nearest neighbor effect is based on the neighboring and stacking nucleotides. [58]

The addition of 10 μM neomycin increased the melting temperature to 46.0 ± 0.1 °C. This shift in the melting temperature is in accordance with the results of the original neomycin-aptamer. In order to test, whether binding of neomycin could lead to a stabilization of the Hg^{2+} -binding-site, first neomycin and then Hg^{2+} -ions were added to COM3. The presence of both analytes increased the melting temperature to 53.1 ± 0.1 °C, which is just ≈ 3 °C smaller than the sum of the single shifts in the melting temperature of the analytes. As control experiment, first Hg^{2+} -ions and then neomycin molecules were added. The melting curves revealed that the chronology of adding one or the other analyte first, did not change the shift in T_m . In the forward cycle, the analytes were added at a temperature, at which both strands were hybridized.

However, the temperature-shift of the original Hg^{2+} -binding DNA (≈ 23 °C) upon addition of Hg^{2+} -ions was not reached. A reason for that could be that the Hg^{2+} -binding-site is not as stabilized in the construct COM3 compared to the original Hg^{2+} -binding DNA. Another plausible explanation could be that the binding pocket is structurally changed before the oligonucleotides were fully denaturated. Thermally increased fluctuation of the nucleotides that build the binding pocket could lead to a dissociation of the analytes. The dissociation of the neomycin molecule and the two Hg^{2+} -ions could have taken place step by step. Thus, intermediate states were very likely and the aptamer denaturation did not occur cooperatively. Nevertheless, the results confirmed a functional neomycin-aptamer and a functional Hg^{2+} -binding DNA unit at the chosen buffer-conditions.

The results of the reverse cycle of COM3 are similar to the forward cycle with two exceptions: The melting temperatures were ≈ 1.5 to 3 °C smaller and the melting transition of COM3 + Hg^{2+} -ions was broader. The differences between the forward and the reverse cycle are similar, as already explained for the original neomycin-aptamer. Possibly, the structures of the oligonucleotides in the transition regime were slightly different. This result also supports the hypothesis that binding of Hg^{2+} -ions to the T-T mismatch is favored, in case the nucleotides, flanking the binding-site are stabilized first.

The melting profiles have a smooth transition from the native to the denaturated state. The combined aptamer has two internal loops, but the melting profiles do not reveal an additional step within the melting profiles (Figure 6.3). I assume that the bulge of the T-T mismatch is too small to be visible at a step in the melting experiments at a heating/ cooling-rate of 0.5 °C. The G-U nucleotides in the internal loop of the neomycin-aptamer can form hydrogen bonds to the other strand, which leads to a smaller internal loop.

In the forward cycle, not necessarily the thermodynamic most stable structure, but also metastable structures might be present. In the reverse cycle, the annealing of the oligonucleotide strands is performed in the presence of the analytes, which can be assumed to result in the thermodynamically most stable structures.

6.1.1 Length of the Communication Module

In order to destabilize the binding-sites of the combined aptamer even further, I truncated the length of the communication module from 3 to 1 nucleotides (nt) (Figure 6.4). For the comparison of the constructs, the mean melting temperatures of three measurements were plotted versus the length of the communication module (Figure 6.4).

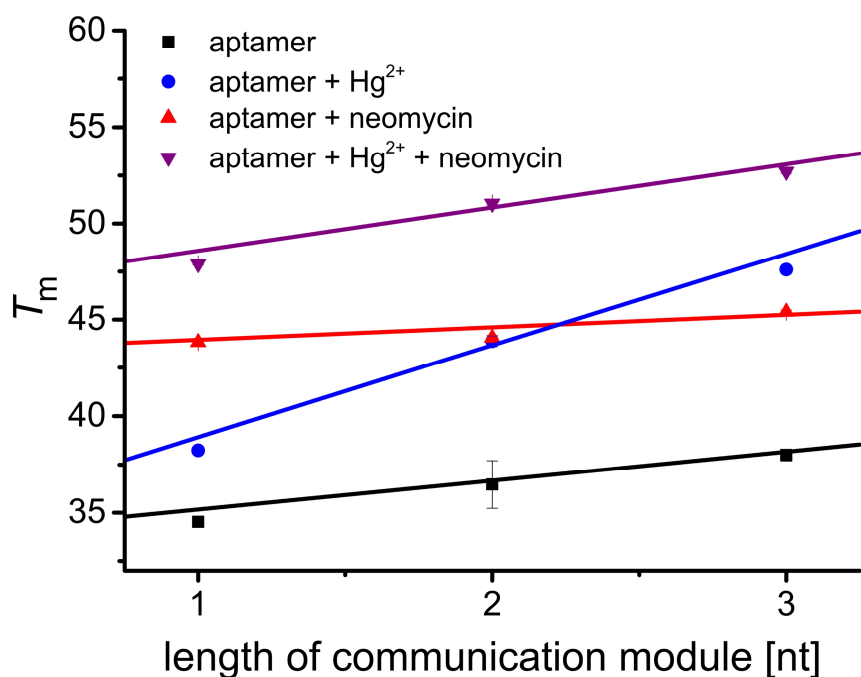


Figure 6.4: Plot of the melting temperatures versus the length of the communication modules for the combined aptamers with and without added analytes. Average values of three independent measurements are plotted. In some cases the error bars are hidden behind the symbols.

The melting temperatures of the constructs COM1 to COM3 without added analytes increased from 34.5 ± 0.1 °C to 38.0 ± 0.3 °C. This can be explained by a different number of oligonucleotides in a critical region of the construct, which contribute to the stability (Figure 6.4). In order to visualize this trend, linear fits were applied to guide the eye.

The melting temperatures upon addition of neomycin almost stayed at a temperature of ≈ 44 °C for the three constructs. Thus, no decrease in the melting temperature upon truncation of the

communication module was observed and it can be concluded that the structure of the neomycin binding pocket seemed to be rarely changed in the construct COM1.

The melting temperatures for the constructs COM1 to COM3 with added Hg^{2+} increased from 38.2 ± 0.1 °C to 47.6 ± 0.1 °C. This increase indicates that the binding-site for Hg^{2+} -ions was further destabilized by the truncation of the communication module. Possibly, the ions bound less likely or left the binding pocket before the cooperative melting process of the oligonucleotide. Adding to this, in the construct COM1, the nucleotides flanking the Hg^{2+} -binding-site changed from a G-C base pair to an A and G. The latter two nucleotides might maximally form two hydrogen bonds, which lead to a further destabilization.

Thus the combined structure consists of two unequal partners, the neomycin binding-pocket is structurally stable and the Hg^{2+} -binding-site is structurally unstable. In order to test, whether the stabilization of the neomycin-binding pocket by neomycin, transduced the stability towards the Hg^{2+} -binding-site, both analytes were added to the oligonucleotide constructs. The melting temperature of COM1 to COM3 increased upon addition of both analytes 47.8 ± 0.1 °C to 52.7 ± 0.1 °C. The reason is that neomycin stabilized the neomycin-aptamer and the stabilization was transduced via the communication module towards the binding-site of the Hg^{2+} -binding DNA. Thus, the construct COM1 is a combined oligonucleotide with positive allostery.

6.1.2 Controls

6.1.2.1 Does Neomycin Bind to a Mutated Split-Aptamer?

In order to check, whether the efficiency of neomycin-binding could be reduced, the binding-pocket was mutated. The nucleotides guanine 10 and guanine 13 were replaced with adenine and uracil, respectively (Figure 6.5a). The mutation should prevent the formation of 4 hydrogen bonds between neomycin and the binding pocket. In the original aptamer, the N7 of guanine 10 builds a hydrogen bond to the C1- NH_3^+ of the non-sugar 2-deoxystreptamine ring. The C6 carbonyl builds one hydrogen bond to the glycosidic ring that connects the non-sugar 2-deoxystreptamine ring and the pyranose ring 1. The N1 and the NH_2 of guanine 13 bind to the C3 carbonyl of the pyranose ring 1. [157] Adenine and uracil were chosen as nucleotides to replace guanine 10 and guanine 13, because these nucleotides are complementary to the nucleotides on the opposite oligonucleotide strand. This should result in the formation of base pairs between the oligonucleotide strands, which should block the binding pocket for an efficient neomycin-binding.

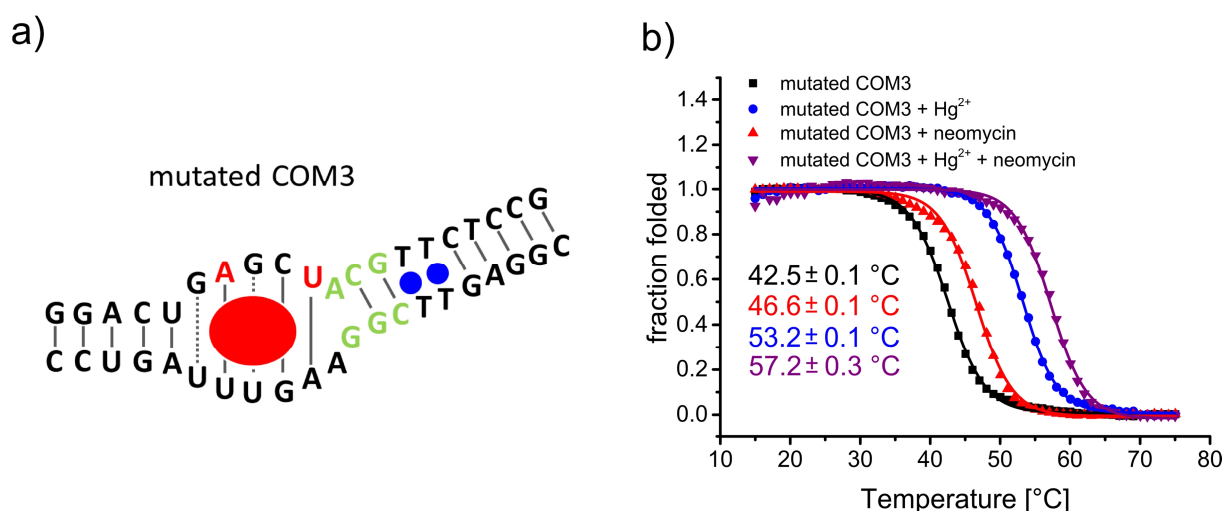


Figure 6.5: Fraction folded versus temperature plot of the mutated COM3 construct. The mean data points of three measurements were plotted. a) The mutated nucleotides are highlighted in red. b) The fraction folded versus temperature plot is shown.

The melting temperature without added analytes was with 42.5 ± 0.1 °C, due to two more base pairs, ≈ 3.5 °C larger compared to the unmutated COM3 (Figure 6.5b). The shift in the melting temperature, which was caused by the addition of neomycin was ≈ 4 °C for the mutated aptamer. This result is in good agreement, because the original aptamer formed 16 hydrogen bonds to neomycin and the shift in the melting temperature was ≈ 6 °C. The mutated aptamer could just build 12 hydrogen bonds to the neomycin molecule.

The shift in T_m caused by Hg²⁺ was ≈ 11 °C for the mutated COM3 and thus $\approx 1 - 2$ °C higher, compared to COM3. Possibly, the neomycin-binding pocket was more stabilized in the mutated COM3 due to the formed base pairs A10-U20 and U13-A17. The stabilization could have affected the stability of the Hg²⁺-binding-site. All in all, the neomycin aptamer turned out to have a robust binding pocket, because neomycin even bound to the mutated split aptamer.

6.1.2.2 What is the Effect of the Analyte Concentration on the Melting Temperature?

At a neomycin concentration of 100 μ M the melting temperature of COM1 was increased by 12.8 °C (from 34.9 ± 0.1 °C to 47.3 ± 0.1 °C) compared to the measurement without neomycin (Figure 6.6). This increase in the melting temperature is twofold the shift in T_m at a neomycin concentration of 10 μ M. In both cases the measurements were performed above the assumed K_d . There are two conceivable scenarios:

1.) At a neomycin concentration of 100 μ M, neomycin might tend to bind, due to the positive charges, unspecifically at other binding-sites, which could have increased the melting temperature. [54]

2.) The binding-pockets of the aptamers in the sample solution were not saturated with neomycin. The reported K_d values of the neomycin aptamer range from 0.1 to 7 μM . [54, 154-156] Assuming the largest reported value of 7 μM , 59 % of the binding-pockets would have been saturated at a concentration of 10 μM according to equation 3.16. A saturation of 94 % of the binding pockets would be given at a concentration of 100 μM . A possible way to distinguish between the cases would be a titration of the aptamer with neomycin. A plot of the melting temperatures versus the neomycin concentrations could be analyzed by a Hill-fit to determine the number of binding-sites.

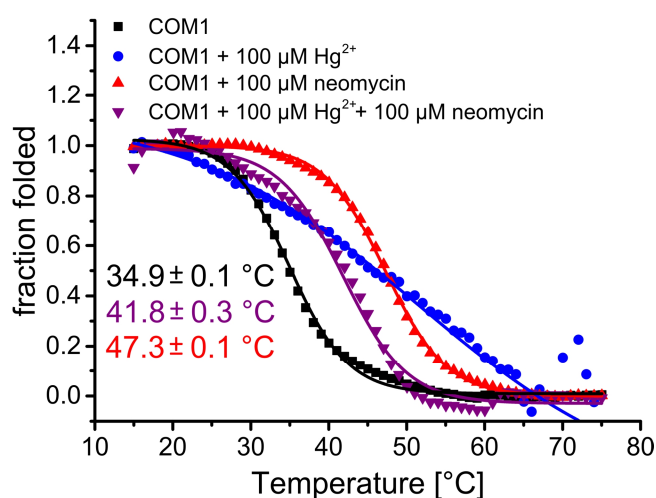


Figure 6.6: Fraction folded versus temperature plot of COM1 with 100 μM neomycin and 100 μM Hg^{2+} -ions.

The melting temperature of COM1 could not be determined at a Hg^{2+} -concentration of 100 μM , because the melting curve lacked a sigmoidal shape. This phenomenon was even partly observed as a broadening of the melting transition at a Hg^{2+} -concentration of 12 μM (Figure 5.12). Liu et al. investigated different Hg^{2+} -binding DNA at Hg^{2+} -ion concentrations of up to 48 μM and did not observe this strong broadening of the melting curve. [176] Possibly, this phenomenon did not occur, because they measured at heating rates of 0.1 $^{\circ}\text{C}/\text{min}$. As proposed by Miyake et al. the presence of intermediate binding states could be eliminated at slow temperature ramps (0.1 $^{\circ}\text{C}/\text{min}$). [55] A mechanism for binding and unbinding of Hg^{2+} -ions from the T-T mismatch could be influenced by a connection between the thymines and $\text{Hg}(\text{II})$ that is longer stable than the flanking nucleotides (Figure 6.7).

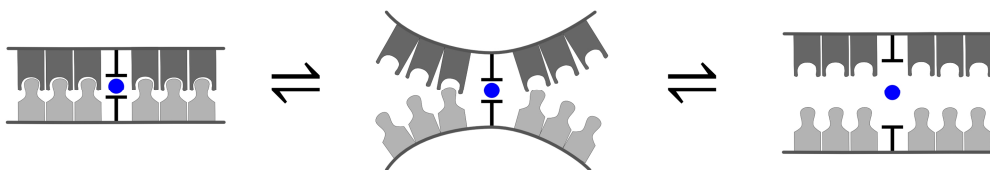


Figure 6.7. Proposed mechanism for Hg^{2+} -ion binding and unbinding by Miyake and coauthors. The oligonucleotide strands are depicted in light- and dark gray, respectively. The thymine-thymine mismatch binds the Hg^{2+} -ion (blue filled circle). Figure modified from Miyake et al. [55]

The melting temperature of COM1 with both analytes was with 41.8 ± 0.3 °C smaller than the construct with just added neomycin. Possibly, the Hg^{2+} -ions shield the negatively charged phosphate-backbone and prevent a sufficient binding of the positively charged neomycin molecule. Thus, the experimental approach does not work for Hg^{2+} -ion concentrations of 100 μM and possibly higher.

6.2 Summary and Conclusion

In this chapter, I elucidated the combination of a split neomycin-aptamer and a Hg^{2+} -ion-binding DNA. It has been shown in literature that suitable communication modules usually consist of less than 7 loosely bound nucleotides. In order to destabilize the chosen binding-sites, a communication module of 3 nt length was chosen. The shift in the melting temperature upon addition of Hg^{2+} -ions turned out to be 2.3 times smaller compared to the original Hg^{2+} -binding DNA. Possibly, the binding-site required a sufficient stabilization that was given by the surrounding nucleotides in the original Hg^{2+} -binding DNA. This assumption is supported by experiments, in which the communication module was truncated from 3 nt stepwise to 1 nt. Here, the shift in the melting temperature upon addition of Hg^{2+} -ions decreased from ≈ 10 °C to ≈ 4 °C. On the other hand, the stabilization of the neomycin-binding pocket transduced the stability to the Hg^{2+} -binding DNA, which was indicated by an increase in the melting temperature upon addition of neomycin and Hg^{2+} -ions. The results of the temperature dependent UV/Vis-absorbance measurements point to the mechanism that the association of Hg^{2+} is favored, in case the Hg^{2+} -binding-site is structurally stabilized by the flanking nucleotides.

It can be assumed that the Hg^{2+} -binding DNA is a candidate for the creation of constructs with positive cooperativity, because the binding-site can be stabilized by another aptamer-unit. Furthermore, the results suggest that the Hg^{2+} -binding-site works best in case the binding-site is framed by 5 (or more) strongly bound base pairs. Consequently, a multiplication of the binding-site should be performed in the following way: 5bp-binding-site-5bp-binding-site-5bp. Unfortunately, the detection of Hg^{2+} -ions by means of temperature dependent UV/Vis melting experiments was not possible at a concentration of 100 μM , which restricts this approach to lower concentrations.

It turned out that the neomycin binding-pocket was very robust, because the truncation of the communication module did not decrease the binding efficiency measured by the shift in the melting

temperature. Even the mutation of two nucleotides in the binding pocket that are supposed to be involved in analyte binding, just decreased the shift in the melting temperature by 2 °C compared to the unmutated oligonucleotide. The neomycin-aptamer was not affected by destabilizations, which were introduced by nucleotides, flanking the binding pocket at the site of the former loop-region. Thus, it is not an aptamer, whose efficiency can be switched by a neighboring binding-site.

7. Summary and Conclusion

I investigated the stability of oligonucleotides by means of single-molecule force spectroscopy and temperature dependent UV/Vis-absorbance measurements. In order to increase the efficiency of the SMFS data analysis, I performed an evaluation of a probability density fit. I could show that the model is very sensitive to the FWHM of the probability density fit. An increase in the FWHM at a constant most probable rupture force, resulted in an increased k_{off} . My analysis suggests that for measurements at loading rates < 1000 pN/s, the FWHM is reasonable low and not broadened by effects like: (a) overlap of the single rupture events with multiple rupture events, (b) rebinding of molecules, (c) conformational changes within the molecule and (d) noise of the instrument. I recommend the probability fit method, in those cases, where the number of tested loading rates has to be minimized. Sensitive samples could be investigated at one loading rate and the data analysis would provide a good estimate for the k_{off} value.

As model aptamer, I tested the stability of a split RNA-streptomycin aptamer. An increased stability of the aptamer upon streptomycin-binding was indicated by an increased most probable rupture force of ≈ 6 pN. By applying the Bell-Evans model, I calculated the k_{off} values of the aptamer with and without bound streptomycin. Here, the aptamer with bound streptomycin had a lower k_{off} value, which is a measure for stability (0.22 ± 0.16 s $^{-1}$ compared to 0.49 ± 0.11 s $^{-1}$). Thus, the single-molecule force spectroscopy measurements revealed an analyte-induced stabilization of $\Delta\Delta G^{\text{sheer}} \approx 3.4$ kJ mol $^{-1}$. The latter value is in the range of magnitude of increased binding energy caused by one base pair. Supported by the results from molecular dynamics simulations, performed by Paulo Netz, I attributed the change in ΔG^{sheer} to the change in the aptamer-structure upon streptomycin-binding. In particular, the base pair 12 and 109 seemed to have contributed to the increase in stability of the split-aptamer. The results led to my conclusion that in SMFS measurements the intermolecular interactions between the aptamer-strands primarily contribute to the stability of the aptamer rather than interactions between the analyte and the binding pocket. Consequently, for the investigation by means of SMFS, aptamers should be chosen that lead to an additional connection between the oligonucleotide strands (black like in Figure 7.1). My results suggest that split-aptamer systems, accessible for single-molecule force spectroscopy in shear geometry, should be those split-aptamers, which build hydrogen bindings between the aptamer strands upon analyte-binding.

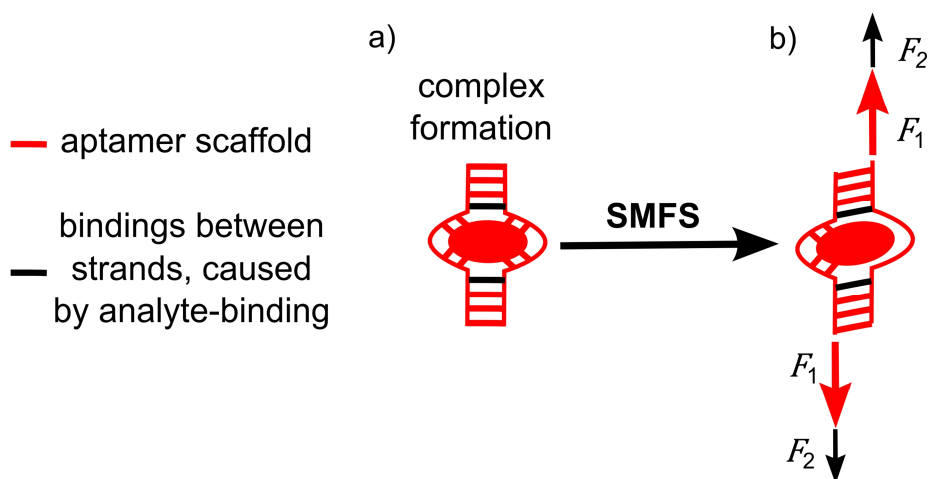


Figure 7.1: Possible explanation for the increase in the rupture force (F_1+F_2) of split-apoptamers, caused by analyte-binding. During the separation process, only the bindings between the two oligonucleotide strands contribute to the stability. The deformation of the binding-pocket might break intermolecular bonds between the analyte and the binding pocket.

In the second part of my thesis, I investigated the combination of aptamers, which is an important topic in the field of aptamer-engineering. Especially, the development of allosteric oligonucleotides, which have binding-sites for different analytes, is of great interest. In my work, I combined the binding-sites of a neomycin-aptamer and a Hg^{2+} -binding-DNA. Between both binding-sites, I inserted a communication module with a length of one to three nucleotides. I have chosen the Hg^{2+} -binding-DNA, because the shift in the melting temperature reportedly depends on the nucleotides flanking the binding-site. This property is crucial for the design of allosteric oligonucleotides. In my experiments, a shift in the melting temperature upon addition of the analyte, indicated a functional binding-site. In case the shift in the melting temperature of the combined and the original oligonucleotide were identical, the functionality of the binding-site was confirmed. My results indicated that the functionality of both oligonucleotides was maintained at the same buffer conditions. Thus, both are suitable candidates for a combined aptamer structure. Additionally, splitting of the neomycin-aptamer between the nucleotides A14 and G15, did not alter the shift in the melting temperature upon neomycin-binding. This example illustrates clearly that a splitting position can be identified, in case the binding pocket is known in detail. Thus, the investigation of binding-sites is highly important in the field of aptamer-research.

I found out that the truncation of the communication module changed the binding efficiency of the Hg^{2+} -binding DNA. The Hg^{2+} -binding-site revealed a pronounced sensitivity to the surrounding nucleotides and furthermore to the neighboring binding-pocket. At a communication module of 1 nt (COM1), the Hg^{2+} -binding efficiency was by a factor of 3 smaller compared to a communication module of 3 nt (COM3). The simultaneous presence of neomycin molecules compensated the

destabilization. Thus, upon binding of neomycin, the affinity of COM1 to Hg^{2+} was equal to COM3 (Figure 7.2). Consequently, I found an oligonucleotide with positive allosterity.

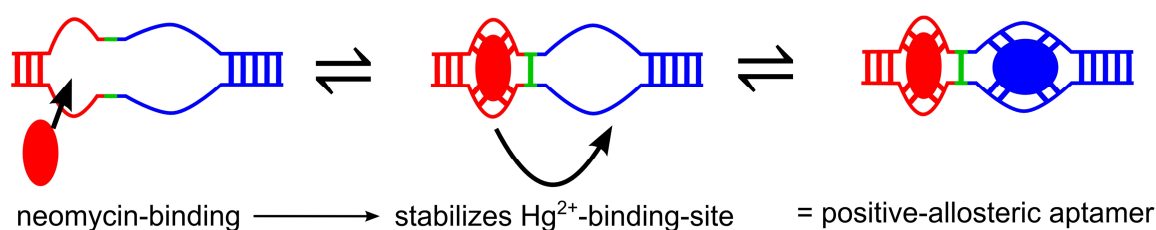


Figure 7.2: Scheme of the allosteric aptamer, consisting of neomycin- and Hg^{2+} -binding-site. Without any analytes, the binding-sites most probably merge to a large internal loop. Binding of neomycin stabilizes one binding-site, which increases the efficiency of Hg^{2+} -binding.

Thus, the Hg^{2+} -binding-site is a suitable unit for the development of allosteric aptamers, when connected to another binding-site by a short communication module (1 nt). In contrast to that, the neomycin-aptamer is a robust aptamer that was not affected by the truncation of the communication module. The neomycin-aptamer is perfectly suitable as “on-off-switch” and thereby as stabilizing part of allosteric oligonucleotides. Based on my results, I recommend less robust binding-sites for the construction of combined oligonucleotides with a negative allosterity. Binding-sites, which pass through an induced fit would be promising, because their binding-sites are less preformed and more influenced by the flanking nucleotides. In these constructs, the communication module would have a larger effect on the overall structure.

In general, analyte-binding is accompanied by a decrease in ΔG° . A plausible explanation, why only some aptamers show reportedly a shift in the melting temperature upon analyte-binding, is that the analytes leave the binding pocket before the melting temperature is reached. Thus, only in the cases where the analyte is bound to the binding-site during the cooperative dissociation process of the aptamer-strands, a shift in the melting temperature is detected.

In future experiments, the neomycin and the Hg^{2+} -binding DNA could be analyzed by means of SMFS experiments to see, whether an increase in the rupture force can be correlated to an increase in the melting temperature. [178] As the dissociation of the oligonucleotides is performed within seconds by means of SMFS, the chance to dissociate the complex at once might be larger compared to temperature dependent UV/Vis-absorbance measurements. The extension to allosteric aptamers would be highly interesting, because one analyte could be saturated and the other analyte could be titrated. A similar sequential addition of analytes could also be performed with ITC (isothermal titration calorimetry). There, the measurements would be performed at temperatures below the melting point, which would reveal the K_d , ΔH° , ΔS° and ΔG° . Furthermore, metastable and allosteric constructs could be detected.

In summary, the temperature dependent UV/Vis absorbance measurements offer an exceptional opportunity to find allosteric oligonucleotides, which could be used in RNA-switching units.

8. Bibliography

1. Chandola, C., et al., *Application of aptamers in diagnostics, drug-delivery and imaging*. J Biosci, 2016. 41(3): p. 535-61.
2. Breaker, R.R. and G.F. Joyce, *Inventing and improving ribozyme function: rational design versus iterative selection methods*. Trends Biotechnol, 1994. 12(7): p. 268-75.
3. Hermann, T. and D.J. Patel, *Adaptive Recognition by Nucleic Acid Aptamers*. Science, 2000. 287(5454): p. 820-825.
4. Poniková, S., et al., *The circular dichroism and differential scanning calorimetry study of the properties of DNA aptamer dimers*. Biophysical Chemistry, 2011. 155(1): p. 29-35.
5. Wilson, D.S. and J.W. Szostak, *In vitro selection of functional nucleic acids*. Annu Rev Biochem, 1999. 68(1): p. 611-47.
6. Li, Y. and Y. Lu, *Functional nucleic acids for analytical applications*. 2009: Springer.
7. Ellington, A.D. and J.W. Szostak, *In vitro selection of RNA molecules that bind specific ligands*. Nature, 1990. 346(6287): p. 818-822.
8. Breaker, R.R., *Natural and engineered nucleic acids as tools to explore biology*. Nature, 2004. 432(7019): p. 838-845.
9. Winkler, W., A. Nahvi, and R.R. Breaker, *Thiamine Derivatives Bind Messenger RNAs Directly to Regulate Bacterial Gene Expression*. Nature, 2002. 419(6910): p. 952-956.
10. Zhang, J., M.W. Lau, and A.R. Ferre-D'Amare, *Ribozymes and riboswitches: modulation of RNA function by small molecules*. Biochemistry, 2010. 49(43): p. 9123-31.
11. Hanson, S., et al., *Tetracycline-aptamer-mediated translational regulation in yeast*. Molecular Microbiology, 2003. 49(6): p. 1627-1637.
12. Leulliot, N. and G. Varani, *Current Topics in RNA-Protein Recognition: Control of Specificity and Biological Function through Induced Fit and Conformational Capture*. Biochemistry, 2001. 40(27): p. 7947-7956.
13. Forster, U., et al., *Conformational dynamics of the tetracycline-binding aptamer*. Nucleic Acids Res, 2012. 40(4): p. 1807-17.
14. Zhang, S., J. Xia, and X. Li, *Electrochemical Biosensor for Detection of Adenosine Based on Structure-Switching Aptamer and Amplification with Reporter Probe DNA Modified Au Nanoparticles*. Analytical Chemistry, 2008. 80(22): p. 8382-8388.
15. Liu, J. and Y. Lu, *Fast Colorimetric Sensing of Adenosine and Cocaine Based on a General Sensor Design Involving Aptamers and Nanoparticles*. Angewandte Chemie International Edition, 2006. 45(1): p. 90-94.
16. Seemann, I.T., et al., *Small-Molecule-Triggered Manipulation of DNA Three-Way Junctions*. Journal of the American Chemical Society, 2011. 133(13): p. 4706-4709.
17. Kent, A.D., N.G. Spiropoulos, and J.M. Heemstra, *General Approach for Engineering Small-Molecule-Binding DNA Split Aptamers*. Analytical Chemistry, 2013. 85(20): p. 9916-9923.
18. Nguyen, T.-H., et al., *Measuring Single Small Molecule Binding via Rupture Forces of a Split Aptamer*. Journal of the American Chemical Society, 2011. 133(7): p. 2025-2027.
19. Stojanovic, M.N., P. de Prada, and D.W. Landry, *Fluorescent sensors based on aptamer self-assembly*. Journal of the American Chemical Society, 2000. 122(46): p. 11547-11548.

20. Melaine, F., Y. Roupioz, and A. Buhot, *Gold Nanoparticles Surface Plasmon Resonance Enhanced Signal for the Detection of Small Molecules on Split-Aptamer Microarrays (Small Molecules Detection from Split-Aptamers)*. *Microarrays*, 2015. 4(1): p. 41.
21. Zeidan, E., et al., *Nano-SPRi Aptasensor for the Detection of Progesterone in Buffer*. *Scientific reports*, 2016. 6.
22. Lin, Z., et al., *Signal-on electrochemiluminescence biosensor for thrombin based on target-induced conjunction of split aptamer fragments*. *Chemical Communications*, 2010. 46(30): p. 5563-5565.
23. Yu, H., et al., *A cooperative-binding split aptamer assay for rapid, specific and ultra-sensitive fluorescence detection of cocaine in saliva*. *Chemical Science*, 2016.
24. Sharma, A.K., A.D. Kent, and J.M. Heemstra, *Enzyme-Linked Small-Molecule Detection Using Split Aptamer Ligation*. *Analytical Chemistry*, 2012. 84(14): p. 6104-6109.
25. Kolpashchikov, D.M., *Binary Malachite Green Aptamer for Fluorescent Detection of Nucleic Acids*. *Journal of the American Chemical Society*, 2005. 127(36): p. 12442-12443.
26. Liu, J., et al., *Highly sensitive colorimetric detection of 17 β -estradiol using split DNA aptamers immobilized on unmodified gold nanoparticles*. *Scientific Reports*, 2014. 4: p. 7571.
27. Du, Y., et al., *Target-induced conjunction of split aptamer as new chiral selector for oligopeptide on graphene-mesoporous silica-gold nanoparticle hybrids modified sensing platform*. *Chemical Communications*, 2012. 48(6): p. 799-801.
28. Jiang, H., et al., *Theophylline detection in serum using a self-assembling RNA aptamer-based gold nanoparticle sensor*. *Biosensors and Bioelectronics*, 2015. 70: p. 299-303.
29. Piganeau, N. and R. Schroeder, *Aptamer Structures: A Preview into Regulatory Pathways?* *Chem. Biol.*, 2003. 10(2): p. 103-104.
30. Neuman, K.C. and A. Nagy, *Single-molecule force spectroscopy: optical tweezers, magnetic tweezers and atomic force microscopy*. *Nature Methods*, 2008. 5(6): p. 491-505.
31. Lee, G., L. Chrisey, and R. Colton, *Direct Measurement of the Forces Between Complementary Strands of DNA*. *Science*, 1994. 266(5186): p. 771-773.
32. Ritzefeld, M., et al., *Analysis of DNA Interactions Using Single-Molecule Force Spectroscopy*. *Amino Acids*, 2013. 44(6): p. 1457-1475.
33. Sengupta, E., et al., *Dynamic Force Spectroscopy of Photoswitch-Modified DNA*. *ACS Nano*, 2014. 8(3): p. 2625-2631.
34. Anna Rita, B., *Biological Applications of Dynamic Force Spectroscopy*, in *Dynamic Force Spectroscopy and Biomolecular Recognition*. 2012, CRC Press. p. 163-192.
35. Woodbury, C.P., *Introduction to Macromolecular Binding Equilibria*. 2007: CRC Press.
36. Rief, M., et al., *Single Molecule Force Spectroscopy on Polysaccharides by Atomic Force Microscopy*. *Science*, 1997. 275(5304): p. 1295-1297.
37. Aubin-Tam, M.-E., et al., *Adhesion Through Single Peptide Aptamers*. *J. Phys. Chem. A*, 2010. 115(16): p. 3657-3664.
38. Basnar, B., R. Elnathan, and I. Willner, *Following Aptamer-Thrombin Binding by Force Measurements*. *Analytical Chemistry*, 2006. 78(11): p. 3638-3642.
39. Strunz, T., et al., *Dynamic force spectroscopy of single DNA molecules*. *Proceedings of the National Academy of Sciences*, 1999. 96(20): p. 11277-11282.

-
40. Strackharn, M., et al., *Functional Assembly of Aptamer Binding Sites by Single-Molecule Cut-and-Paste*. Nano Letters, 2012. 12(5): p. 2425-2428.
 41. Gaub, B.M., et al., *Switching the mechanics of dsDNA by Cu salicylic aldehyde complexation*. Nanotechnology, 2009. 20(43): p. 434002.
 42. Heus, H.A., et al., *Atomic Force Microscope-Based Single-Molecule Force Spectroscopy of RNA Unfolding*. Analytical Biochemistry, 2011. 414(1): p. 1-6.
 43. Green, N.H., et al., *Single-Molecule Investigations of RNA Dissociation*. Biophysical Journal, 2004. 86(6): p. 3811-3821.
 44. Motlagh, H.N., et al., *The ensemble nature of allostery*. Nature, 2014. 508(7496): p. 331-9.
 45. Soukup, G.A. and R.R. Breaker, *Engineering precision RNA molecular switches*. Proc Natl Acad Sci U S A, 1999. 96(7): p. 3584-9.
 46. Tang, J. and R.R. Breaker, *Rational design of allosteric ribozymes*. Chemistry & Biology, 1997. 4(6): p. 453-459.
 47. Stojanovic, M.N. and D.M. Kolpashchikov, *Modular Aptameric Sensors*. Journal of the American Chemical Society, 2004. 126(30): p. 9266-9270.
 48. Soukup, G.A. and R.R. Breaker, *Allosteric nucleic acid catalysts*. Current Opinion in Structural Biology, 2000. 10(3): p. 318-325.
 49. Roth, A. and R.R. Breaker, *An amino acid as a cofactor for a catalytic polynucleotide*. Proceedings of the National Academy of Sciences of the United States of America, 1998. 95(11): p. 6027-6031.
 50. Helm, M., et al., *Allosterically Activated Diels–Alder Catalysis by a Ribozyme*. Journal of the American Chemical Society, 2005. 127(30): p. 10492-10493.
 51. Win, M.N. and C.D. Smolke, *A modular and extensible RNA-based gene-regulatory platform for engineering cellular function*. Proceedings of the National Academy of Sciences of the United States of America, 2007. 104(36): p. 14283-14288.
 52. Marky, L.A. and K.J. Breslauer, *Calculating thermodynamic data for transitions of any molecularity from equilibrium melting curves*. Biopolymers, 1987. 26(9): p. 1601-1620.
 53. Lee, Y.-J., et al., *Single-channel multiplexing without melting curve analysis in real-time PCR*. Scientific Reports, 2014. 4: p. 7439.
 54. Stampfl, S., et al., *Monovalent Ion Dependence of Neomycin B Binding to an RNA Aptamer Characterized by Spectroscopic Methods*. ChemBioChem, 2007. 8(10): p. 1137-1145.
 55. Miyake, Y., et al., *MercuryII-Mediated Formation of Thymine–HgII–Thymine Base Pairs in DNA Duplexes*. Journal of the American Chemical Society, 2006. 128(7): p. 2172-2173.
 56. Kankia, B.I. and L.A. Marky, *Folding of the Thrombin Aptamer into a G-Quadruplex with Sr²⁺: Stability, Heat, and Hydration*. Journal of the American Chemical Society, 2001. 123(44): p. 10799-10804.
 57. Sengupta, A., et al., *Role of Mg²⁺ ions in flavin recognition by RNA aptamer*. Journal of Photochemistry and Photobiology B: Biology, 2014. 140: p. 240-248.
 58. Yamaguchi, H., et al., *The structure of metallo-DNA with consecutive thymine–HgII–thymine base pairs explains positive entropy for the metallo base pair formation*. Nucleic Acids Research, 2014. 42(6): p. 4094-4099.

-
59. Butt, H.-J. and M. Jaschke, *Calculation of Thermal Noise in Atomic Force Microscopy*. Nanotechnology, 1995. 6(1): p. 1.
 60. Rico, F. and V.T. Moy, *Energy Landscape Roughness of the Streptavidin–Biotin Interaction*. J. Mol. Recognit., 2007. 20(6): p. 495-501.
 61. Schumakovitch, I., et al., *Temperature Dependence of Unbinding Forces between Complementary DNA Strands*. Biophysical Journal, 2002. 82(1 Pt 1): p. 517-521.
 62. Wallace, S.T. and R. Schroeder, *In Vitro Selection and Characterization of Streptomycin-Binding RNAs: Recognition Discrimination Between Antibiotics*. RNA, 1998. 4(1): p. 112-123.
 63. Windbichler, N. and R. Schroeder, *Isolation of Specific RNA-Binding Proteins Using the Streptomycin-Binding RNA Aptamer*. Nat. Protocols, 2006. 1(2): p. 637-640.
 64. Taninaka, A., et al., *Force Measurement Enabling Precise Analysis by Dynamic Force Spectroscopy*. Int. J. Mol. Sci., 2011. 13(1): p. 453-465.
 65. Claudia, F., et al., *Dynamic Single-Molecule Force Spectroscopy: Bond Rupture Analysis with Variable Spacer Length*. Journal of Physics: Condensed Matter, 2003. 15(18): p. S1709.
 66. Kurzynski, J.A.T.a.M., *Structures of Biomolecules*, in *Introduction to Molecular Biophysics*. 2003, CRC Press. p. 23-94.
 67. Chin, K., et al., *Calculating the electrostatic properties of RNA provides new insights into molecular interactions and function*. Nat Struct Mol Biol, 1999. 6(11): p. 1055-1061.
 68. Berg, J.M., L. Stryer, and J.L. Tymoczko, *Stryer Biochemie*. 2015: Springer-Verlag.
 69. Yakushevich, L.V., *Nonlinear Physics of DNA, 2nd Edition*. June 2004.
 70. Elias, M., et al., *The molecular basis of phosphate discrimination in arsenate-rich environments*. Nature, 2012. 491(7422): p. 134-137.
 71. Jeremy M. Berg, J.L.T., Lubert Stryer *Stryer Biochemie*. 2013.
 72. Binnig, G., C.F. Quate, and C. Gerber, *Atomic Force Microscope*. Physical Review Letters, 1986. 56(9): p. 930-933.
 73. Meyer, G. and N.M. Amer, *Novel optical approach to atomic force microscopy*. Applied Physics Letters, 1988. 53(12): p. 1045-1047.
 74. Moreno-Herrero, F. and J. Gomez-Herrero, *AFM: Basic Concepts*, in *Atomic Force Microscopy in Liquid*. 2012, Wiley-VCH Verlag GmbH & Co. KGaA. p. 1-34.
 75. Lennard-Jones, J.E., *Cohesion*. Proceedings of the Physical Society, 1931. 43(5): p. 461.
 76. Hutter, J.L. and J. Bechhoefer, *Calibration of atomic-force microscope tips*. Review of Scientific Instruments, 1993. 64(7): p. 1868-1873.
 77. Butt, H.-J., B. Cappella, and M. Kappl, *Force measurements with the atomic force microscope: Technique, interpretation and applications*. Surface Science Reports, 2005. 59(1–6): p. 1-152.
 78. Butt, H.-J. and M. Kappl, *Surface and interfacial forces*. 2009: John Wiley & Sons.
 79. JPK, *NanoWizard®3 AFM User Manual 4.2*. 2012.
 80. Walters, D.A., et al., *Short cantilevers for atomic force microscopy*. Review of Scientific Instruments, 1996. 67(10): p. 3583-3590.
 81. Stark, R.W., T. Drobek, and W.M. Heckl, *Thermomechanical noise of a free v-shaped cantilever for atomic-force microscopy*. Ultramicroscopy, 2001. 86(1–2): p. 207-215.

-
82. García, R. and R. Pérez, *Dynamic atomic force microscopy methods*. Surface Science Reports, 2002. 47(6–8): p. 197-301.
 83. Cook, S.M., et al., *Practical implementation of dynamic methods for measuring atomic force microscope cantilever spring constants*. Nanotechnology, 2006. 17(9): p. 2135.
 84. Noy, A., *Force Spectroscopy 101: How to Design, Perform, and Analyze an AFM-Based Single Molecule Force Spectroscopy Experiment*. Current Opinion in Chemical Biology, 2011. 15(5): p. 710-718.
 85. Neundlinger, I., et al., *Characterization of Enhanced Monovalent and Bivalent Thrombin DNA Aptamer Binding Using Single Molecule Force Spectroscopy*. Biophysical Journal, 2011. 101(7): p. 1781-1787.
 86. Grandbois, M., et al., *How Strong Is a Covalent Bond?* Science, 1999. 283(5408): p. 1727-1730.
 87. Hinterdorfer, P. and Y.F. Dufrene, *Detection and localization of single molecular recognition events using atomic force microscopy*. Nat Meth, 2006. 3(5): p. 347-355.
 88. Franz, C.M. and A. Taubenberger, *AFM-Based Single-Cell Force Spectroscopy*, in *Atomic Force Microscopy in Liquid*. 2012, Wiley-VCH Verlag GmbH & Co. KGaA. p. 307-330.
 89. Kenworthy, A.K., S.A. Simon, and T.J. McIntosh, *Structure and phase behavior of lipid suspensions containing phospholipids with covalently attached poly(ethylene glycol)*. Biophysical Journal, 1995. 68(5): p. 1903-1920.
 90. Alsteens, D., et al., *Imaging G protein-coupled receptors while quantifying their ligand-binding free-energy landscape*. Nat Meth, 2015. 12(9): p. 845-851.
 91. Raymond, W.F., *Theoretical Models in Force Spectroscopy*, in *Dynamic Force Spectroscopy and Biomolecular Recognition*. 2012, CRC Press. p. 51-91.
 92. Eyring, H., *Viscosity, plasticity, and diffusion as examples of absolute reaction rates*. The Journal of chemical physics, 1936. 4(4): p. 283-291.
 93. Tobolsky, A. and H. Eyring, *Mechanical properties of polymeric materials*. The Journal of Chemical Physics, 1943. 11(3): p. 125-134.
 94. Kramers, H.A., *Brownian Motion in a Field of Force and the Diffusion Model of Chemical Reactions*. Physica, 1940. 7(4): p. 284-304.
 95. Bell, G., *Models for the Specific Adhesion of Cells to Cells*. Science, 1978. 200(4342): p. 618-627.
 96. Evans, E. and K. Ritchie, *Dynamic Strength of Molecular Adhesion Bonds*. Biophysical Journal, 1997. 72(4): p. 1541-1555.
 97. Evans, E., *Probing the Relation Between Force-Lifetime-and Chemistry in Single Molecular Bonds*. Annu Rev Biophys Biomol Struct, 2001. 30(1): p. 105-28.
 98. Bullerjahn, J.T., S. Sturm, and K. Kroy, *Theory of rapid force spectroscopy*. Nat Commun, 2014. 5: p. 4463.
 99. Lv, Z., et al., *Mechanism of Amyloid [bgr]-Protein Dimerization Determined using Single-Molecule AFM Force Spectroscopy*. Sci. Rep., 2013. 3.
 100. Hane, F.T., S.J. Attwood, and Z. Leonenko, *Comparison of Three Competing Dynamic Force Spectroscopy Models to Study Binding Forces of Amyloid-[small beta] (1-42)*. Soft Matter, 2014. 10(12): p. 1924-1930.

101. Friddle, R.W., A. Noy, and J.J. De Yoreo, *Interpreting the widespread nonlinear force spectra of intermolecular bonds*. Proceedings of the National Academy of Sciences of the United States of America, 2012. 109(34): p. 13573-13578.
102. Florin, E.-L., V.T. Moy, and H.E. Gaub, *Adhesion forces between individual ligand-receptor pairs*. Science, 1994. 264(5157): p. 415-417.
103. Zhang, X. and V.K. Yadavalli, *Molecular interaction studies of vascular endothelial growth factor with RNA aptamers*. Analyst, 2010. 135(8): p. 2014-2021.
104. Tuerk, C. and L. Gold, *Systematic evolution of ligands by exponential enrichment: RNA ligands to bacteriophage T4 DNA polymerase*. Science, 1990. 249(4968): p. 505-510.
105. Joyce, G.F., *Amplification, mutation and selection of catalytic RNA*. Gene, 1989. 82(1): p. 83-87.
106. Blank, M. and M. Blind, *Aptamers as Tools for Target Validation*. Current Opinion in Chemical Biology, 2005. 9(4): p. 336-342.
107. Serganov, A. and E. Nudler, *A Decade of Riboswitches*. Cell, 2013. 152(1-2): p. 17-24.
108. Hermann, T. and D.J. Patel, *RNA Bulges as Architectural and Recognition Motifs*. Struct. Fold. Des., 2000. 8(3): p. 47-54.
109. Pagano, B., et al., *Stability and Binding Properties of a Modified Thrombin Binding Aptamer*. Biophysical Journal, 2008. 94(2): p. 562-569.
110. Arnaut, V., M. Langecker, and Friedrich C. Simmel, *Nanopore Force Spectroscopy of Aptamer-Ligand Complexes*. Biophysical Journal, 2013. 105(5): p. 1199-1207.
111. Batey, R.T., R.P. Rambo, and J.A. Doudna, *Tertiary motifs in RNA structure and folding*. Angewandte Chemie International Edition, 1999. 38(16): p. 2326-2343.
112. Stoltenburg, R., C. Reinemann, and B. Strehlitz, *SELEX—A (r)evolutionary method to generate high-affinity nucleic acid ligands*. Biomolecular Engineering, 2007. 24(4): p. 381-403.
113. Jing, M. and M.T. Bowser, *Methods for measuring aptamer-protein equilibria: A review*. Analytica Chimica Acta, 2011. 686(1-2): p. 9-18.
114. Blind, M. and M. Blank, *Aptamer Selection Technology and Recent Advances*. Mol Ther Nucleic Acids, 2015. 4: p. e223.
115. Demirci, H., et al., *A Structural Basis for Streptomycin-Induced Misreading of the Genetic Code*. Nat. Commun., 2013. 4: p. 1355.
116. Baxter, G.A., et al., *Detection of Streptomycin Residues in Whole Milk Using an Optical Immunobiosensor*. Journal of Agricultural and Food Chemistry, 2001. 49(7): p. 3204-3207.
117. Cho, E.J., J.-W. Lee, and A.D. Ellington, *Applications of Aptamers as Sensors*. Annu. Rev. Anal. Chem., 2009. 2(1): p. 241-264.
118. Rice, P.A., et al., *Crystal Structure of an IHF-DNA Complex: A Protein-Induced DNA U-Turn*. Cell, 1996. 87(7): p. 1295-1306.
119. Tereshko, V., E. Skripkin, and D.J. Patel, *Encapsulating Streptomycin within a Small 40-mer RNA*. Chemistry & Biology, 2003. 10(2): p. 175-187.
120. Nick, T.A., et al., *Stability of a Split Streptomycin Binding Aptamer*. The Journal of Physical Chemistry B, 2016.
121. Longfellow, C.E., R. Kierzek, and D.H. Turner, *Thermodynamic and Spectroscopic Study of Bulge Loops in Oligoribonucleotides*. Biochemistry, 1990. 29(1): p. 278-285.

-
122. Cocco, S. and R. Monasson, *Statistical Mechanics of Torque Induced Denaturation of DNA*. Physical Review Letters, 1999. 83(24): p. 5178-5181.
 123. Cocco, S., R. Monasson, and J.F. Marko, *Unzipping dynamics of long DNAs*. Physical Review E, 2002. 66(5): p. 051914.
 124. Tereshko, V., E. Skripkin, and D.J. Patel, *Encapsulating streptomycin within a small 40-mer RNA*. Chem. Biol., 2003. 10(2): p. 175-87.
 125. Lavery, R., et al., *Structure and Mechanics of Single Biomolecules: Experiment and Simulation*. J. Phys-Condens. Mat., 2002. 14(14): p. R383-R414.
 126. De Silva, L., et al., *Well-Defined and Sequence-Specific Noncovalent Binding Forces of DNA*. J. Phys. Chem. B, 2013. 117(25): p. 7554-7558.
 127. SantaLucia, J., *A Unified View of Polymer, Dumbbell, and Oligonucleotide DNA Nearest-Neighbor Thermodynamics*. P. Natl. A. Sci., 1998. 95(4): p. 1460-1465.
 128. Block, S., et al., *Characterization of Bonds Formed Between Platelet Factor 4 and Negatively Charged Drugs Using Single Molecule Force Spectroscopy*. Soft Matter, 2014. 10(16): p. 2775-2784.
 129. Ling, L., H.-J. Butt, and R. Berger, *Rupture Force between the Third Strand and the Double Strand within a Triplex DNA*. Journal of the American Chemical Society, 2004. 126(43): p. 13992-13997.
 130. Getfert, S. and P. Reimann, *Hidden Multiple Bond Effects in Dynamic Force Spectroscopy*. Biophysical Journal, 2012. 102(5): p. 1184-1193.
 131. Guo, S., et al., *Effects of Multiple-Bond Ruptures on Kinetic Parameters Extracted from Force Spectroscopy Measurements: Revisiting Biotin-Streptavidin Interactions*. Biophysical Journal, 2008. 95(8): p. 3964-3976.
 132. Ray, C., J.R. Brown, and B.B. Akhremitchev, *Correction of Systematic Errors in Single-Molecule Force Spectroscopy with Polymeric Tethers by Atomic Force Microscopy*. J. Phys. Chem. B, 2007. 111(8): p. 1963-1974.
 133. Kufer, S.K., et al., *Single-Molecule Cut-and-Paste Surface Assembly*. Science, 2008. 319(5863): p. 594-596.
 134. Bockelmann, U., et al., *Unzipping DNA with Optical Tweezers: High Sequence Sensitivity and Force Flips*. Biophysical Journal, 2002. 82(3): p. 1537-1553.
 135. Liphardt, J., et al., *Reversible Unfolding of Single RNA Molecules by Mechanical Force*. Science, 2001. 292(5517): p. 733-737.
 136. Reuss, Andreas J., et al., *Tetracycline Determines the Conformation of Its Aptamer at Physiological Magnesium Concentrations*. Biophysical Journal, 2014. 107(12): p. 2962-2971.
 137. Li, T., E. Wang, and S. Dong, *Lead(II)-Induced Allosteric G-Quadruplex DNAzyme as a Colorimetric and Chemiluminescence Sensor for Highly Sensitive and Selective Pb²⁺ Detection*. Analytical Chemistry, 2010. 82(4): p. 1515-1520.
 138. Majhi, P.R. and R.H. Shafer, *Characterization of an unusual folding pattern in a catalytically active guanine quadruplex structure*. Biopolymers, 2006. 82(6): p. 558-569.
 139. Scheunemann, A.E., et al., *Binding of aminoglycoside antibiotics to helix 69 of 23S rRNA*. Nucleic Acids Research, 2010. 38(9): p. 3094-3105.
 140. Arya, D.P. and R.L. Coffee Jr, *DNA Triple Helix Stabilization by Aminoglycoside Antibiotics*. Bioorganic & Medicinal Chemistry Letters, 2000. 10(17): p. 1897-1899.

-
141. Willis, B. and D.P. Arya, *Recognition of RNA duplex by a neomycin–Hoechst 33258 conjugate*. *Bioorganic & Medicinal Chemistry*, 2014. 22(7): p. 2327-2332.
 142. Xi, H., et al., *Thermodynamics of Nucleic Acid “Shape Readout” by an Aminosugar*. *Biochemistry*, 2011. 50(42): p. 9088-9113.
 143. Hamilton, P.L. and D.P. Arya, *Natural product DNA major groove binders*. *Natural Product Reports*, 2012. 29(2): p. 134-143.
 144. Kankia, B.I., G. Barany, and K. Musier-Forsyth, *Unfolding of DNA quadruplexes induced by HIV-1 nucleocapsid protein*. *Nucleic Acids Research*, 2005. 33(14): p. 4395-4403.
 145. Puglisi, J.D. and I. Tinoco Jr, *[22] absorbance melting curves of RNA*, in *Methods in Enzymology*. 1989, Academic Press. p. 304-325.
 146. Puglisi, J.D. and I. Tinoco, Jr., *Absorbance melting curves of RNA*. *Methods Enzymol*, 1989. 180: p. 304-25.
 147. Felsenfeld, G. and S.Z. Hirschman, *A neighbor-interaction analysis of the hypochromism and spectra of DNA*. *Journal of molecular biology*, 1965. 13(2): p. 407-427.
 148. Siegfried, N.A. and P.C. Bevilacqua, *Chapter 13 Thinking Inside the Box: Designing, Implementing, and Interpreting Thermodynamic Cycles to Dissect Cooperativity in RNA and DNA Folding*, in *Methods in Enzymology*. 2009, Academic Press. p. 365-393.
 149. Manning, G.S., *The molecular theory of polyelectrolyte solutions with applications to the electrostatic properties of polynucleotides*. *Quarterly reviews of biophysics*, 1978. 11(02): p. 179-246.
 150. Moazed, D. and H.F. Noller, *Interaction of antibiotics with functional sites in 16S ribosomal RNA*. *Nature*, 1987. 327(6121): p. 389-394.
 151. Alper, P.B., et al., *Probing the Specificity of Aminoglycoside–Ribosomal RNA Interactions with Designed Synthetic Analogs*. *Journal of the American Chemical Society*, 1998. 120(9): p. 1965-1978.
 152. Mei, H.-Y., et al., *Inhibition of an HIV-1 Tat-derived peptide binding to TAR RNA by aminoglycoside antibiotics*. *Bioorganic & Medicinal Chemistry Letters*, 1995. 5(22): p. 2755-2760.
 153. Lacourciere, K.A., J.T. Stivers, and J.P. Marino, *Mechanism of Neomycin and Rev Peptide Binding to the Rev Responsive Element of HIV-1 As Determined by Fluorescence and NMR Spectroscopy*. *Biochemistry*, 2000. 39(19): p. 5630-5641.
 154. Wallis, M.G., et al., *A novel RNA motif for neomycin recognition*. *Chemistry & Biology*, 1995. 2(8): p. 543-552.
 155. Wallis, M.G. and R. Schroeder, *The binding of antibiotics to RNA*. *Progress in Biophysics and Molecular Biology*, 1997. 67(2–3): p. 141-154.
 156. Cowan, J.A., et al., *Recognition of a cognate RNA aptamer by neomycin B: quantitative evaluation of hydrogen bonding and electrostatic interactions*. *Nucleic Acids Research*, 2000. 28(15): p. 2935-2942.
 157. Jiang, L., et al., *Saccharide–RNA recognition in a complex formed between neomycin B and an RNA aptamer*. *Structure*, 1999. 7(7): p. 817-87.
 158. Freire, F., et al., *A simple NMR analysis of the protonation equilibrium that accompanies aminoglycoside recognition: Dramatic alterations in the neomycin-B protonation state upon binding to a 23-mer RNA aptamer*. *Chemical Communications*, 2007(2): p. 174-176.

-
159. Jucker, F.M., et al., *A network of heterogeneous hydrogen bonds in GNRA tetraloops*. Journal of Molecular Biology, 1996. 264(5): p. 968-980.
160. Ilgu, M., et al., *An adaptable pentaloop defines a robust neomycin-B RNA aptamer with conditional ligand-bound structures*. RNA, 2014. 20(6): p. 815-824.
161. Schroeder, S.J. and D.H. Turner, *Chapter 17 - Optical Melting Measurements of Nucleic Acid Thermodynamics*, in *Methods in Enzymology*. 2009, Academic Press. p. 371-387.
162. Cantor, C.R. and P. Schimmel, *Biophysical Chemistry, Part I: The Conformation of Biological Molecules*. Journal of Solid-Phase Biochemistry, 1980. 5(3).
163. Petersheim, M. and D.H. Turner, *Base-stacking and base-pairing contributions to helix stability: thermodynamics of double-helix formation with CCGG, CCGGp, CCGGAp, ACCGGp, CCGGUp, and ACCGGUp*. Biochemistry, 1983. 22(2): p. 256-263.
164. Breslauer, K.J., J.M. Sturtevant, and I. Tinoco, *Calorimetric and spectroscopic investigation of the helix-to-coil transition of a ribo-oligonucleotide: rA 7 U 7*. Journal of molecular biology, 1975. 99(4): p. 549-565.
165. Gralla, J. and D.M. Crothers, *Free energy of imperfect nucleic acid helices*. Journal of Molecular Biology, 1973. 73(4): p. 497-511.
166. Stromgaard, K., P. Krosgaard-Larsen, and U. Madsen, *Textbook of drug design and discovery*. 2009: CRC Press.
167. Barceló, F., D. Capó, and J. Portugal, *Thermodynamic characterization of the multivalent binding of chartreusin to DNA*. Nucleic Acids Research, 2002. 30(20): p. 4567-4573.
168. Wada, A., et al., *Fine Structure in the Thermal Denaturation of DNA: High Temperature-Resolution Spectrophotometric Studie*. CRC critical reviews in biochemistry, 1980. 9(2): p. 87-144.
169. Bereznyak, E., et al., *Thermal analysis of ligand-DNA interaction: determination of binding parameters*. AIMS Biophysics, 2015. 2(4): p. 423-440.
170. SantaLucia, J. and D.H. Turner, *Measuring the thermodynamics of RNA secondary structure formation*. Biopolymers, 1997. 44(3): p. 309-319.
171. Ren, W., et al., *Ultrasensitive Label-Free Resonance Rayleigh Scattering Aptasensor for Hg²⁺ Using Hg²⁺-Triggered Exonuclease III-Assisted Target Recycling and Growth of G-Wires for Signal Amplification*. Analytical Chemistry, 2016. 88(2): p. 1385-1390.
172. Katz, S., *The reversible reaction of Hg (II) and double-stranded polynucleotides a step-function theory and its significance*. Biochimica et Biophysica Acta (BBA) - Specialized Section on Nucleic Acids and Related Subjects, 1963. 68: p. 240-253.
173. Xu, E., et al., *An electrochemical study based on thymine-Hg-thymine DNA base pair mediated charge transfer processes*. RSC Advances, 2015. 5(61): p. 49819-49823.
174. Uchiyama, T., et al., *Raman spectroscopic detection of the T-Hg(II)-T base pair and the ionic characteristics of mercury*. Nucleic Acids Research, 2012. 40(12): p. 5766-5774.
175. Torigoe, H., A. Ono, and T. Kozasa, *HgII Ion Specifically Binds with T:T Mismatched Base Pair in Duplex DNA*. Chemistry – A European Journal, 2010. 16(44): p. 13218-13225.
176. Liu, G., et al., *Studies on the thymine-mercury-thymine base pairing in parallel and anti-parallel DNA duplexes*. New Journal of Chemistry, 2015. 39(11): p. 8752-8762.

177. Plum, G.E., K.J. Breslauer, and R.W. Roberts, *Thermodynamics and kinetics of nucleic acid association/dissociation and folding processes*. Comprehensive natural products chemistry, 1999. 7: p. 15-53.
178. Mishra, R.K., S. Nath, and S. Kumar, *Rupture of DNA aptamer: New insights from simulations*. The Journal of chemical physics, 2015. 143(16): p. 164902.

9. Appendix

X-ray Photoelectron Spectroscopy (XPS)

For the verification of a successful functionalization of the cantilever tips with RNA-strands, XPS measurements were performed by Hao Lu. XPS is also referred to as electron spectroscopy for chemical analysis (ESCA) with a sample depth of ≈ 10 nm. This technique was developed by Siegbahn and colleagues in 1960.

In an ultra-high vacuum (UHV) environment, the surface atoms of the sample are excited with X-rays photons. The excitation energy ($h\nu$) of these photons is higher than the binding energy of the atoms core level (BE). Consequently, the atoms are ionized and photoelectrons with a defined kinetic energy (KE) are emitted. The kinetic energy can be calculated according to the following equation:

$$KE = h\nu - BE - \phi_{\text{spec}}$$

with the work function of the solid (ϕ_{spec}) as instrumental correction factor, which accounts for the difference between the Fermi level and the vacuum level. The excitation energy ($h\nu$) is the product of the Planck constant ($h = 6.626 \times 10^{-34}$ J s) and the frequency (ν in Hz) of the radiation. The binding energy (BE) of the core level atoms is the energy difference between the ionized and the neutral atom. In typical XPS spectra, the number of detected photoelectrons is plotted versus the binding energy scale (in eV). Each electron configuration of the excited atoms (e.g. C1s, P2p) has its specified binding energy.

Typically X-ray sources like Aluminum (Al K α) or Magnesium (Mg K α) emit photons with energies of 1486.6 eV and 1253.6 eV, respectively. The measurement is typically performed in a UHV-chamber with a pressure of $< 10^{-9}$ mbar. This is necessary, because the counting detector is up to one meter away from the sample. Thus, the number of gas atoms, interfering with the emitted photoelectrons, has to be minimized. The detection limit of XPS is 0.2%

In this work, XPS was applied to determine the elemental composition of a cantilever, which was prepared according to the sample-preparation for the single-molecule force spectroscopy measurements. As result from the immobilization step the chip with all cantilevers was exposed to APTES and PEG-linkers (green oval in Figure 9.1a). The treatment with RNA containing solution was just performed on one site of the chip (blue oval in Figure 9.1a). In the XPS spectrum of cantilever 2, the presence of a peak at 134.3 eV indicates the presence of phosphorous (P2p). This is a straightforward proof for a successful immobilization of RNA onto the cantilever, because neither the APTES nor the PEG-linker carried phosphorous groups (Figure 9.1b). While the absence of this peak in the XPS spectrum of cantilever 1 indicates that no RNA was bound to this cantilever. The XPS spectrum of cantilever 1 indicates the presence of oxygen O1s by a peak at 532.9 eV. The O1s peak is

obviously broader in the XPS-spectrum of cantilever 2 (Figure 9.1c). This effect can be explained by the presence of different oxygen compounds from the modified linker. Overlapping peaks correspond to the carbon compounds (C1s) in the XPS-spectra of cantilever 1 and 2. The spectrum, corresponding to cantilever 1, has one main peak at 285.7 eV and a small peak at 288.7 eV (Figure 9.1d). In the XPS-spectrum of cantilever 2, the peak at 285.3 eV has a “shoulder” at approximately 286.9 eV, which can be originated from additional carbon compounds within immobilized RNA. This “shoulder” could also be an additional “fingerprint” for a successful RNA immobilization.

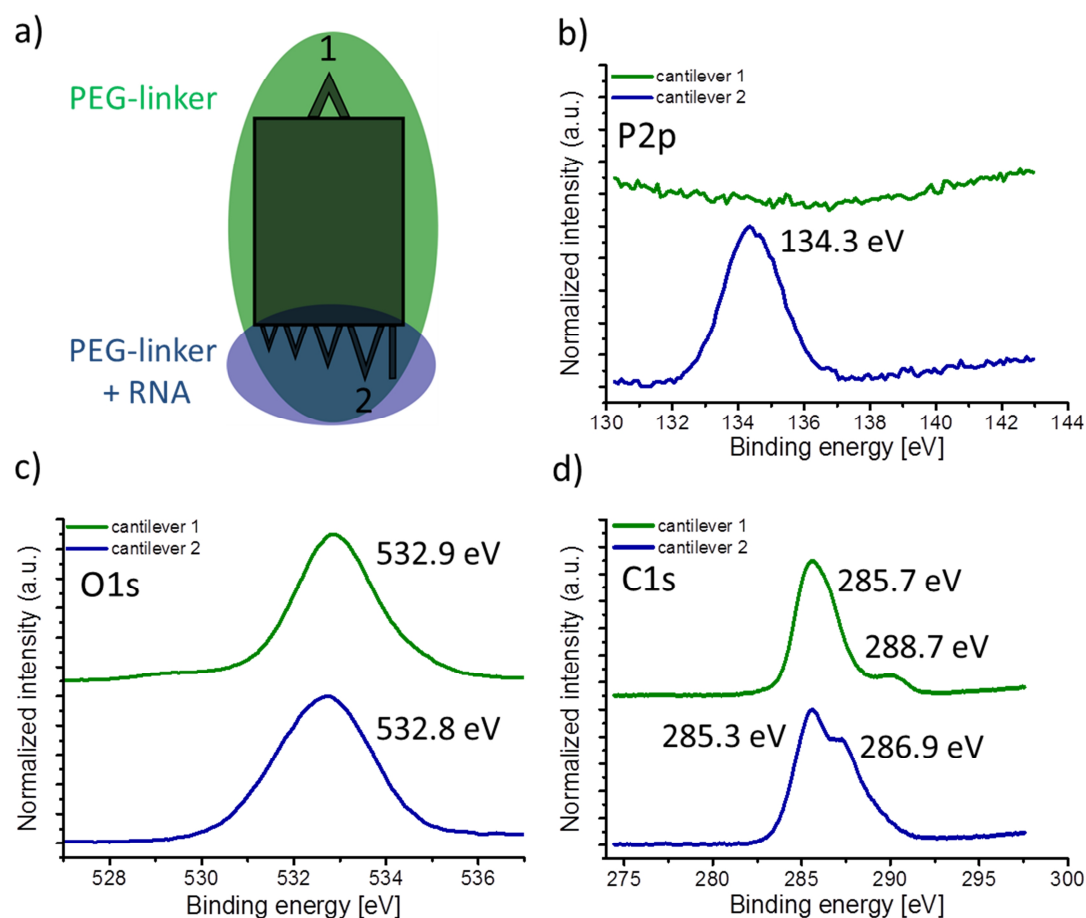


Figure 9.1. a) Scheme of the cantilever, which is treated with PEG-linker (green) and RNA (blue). b) Normalized intensity versus binding energy recorded of cantilever 1 and cantilever 2 of P2p, c) O1s, d) C1s.

X-ray Photoelectron Spectroscopy: Experimental

The XPS measurement was conducted on a Kratos Axis Ultra^{DLD} spectrometer (Kratos, Manchester, England). An Al K α excitation source with a photon energy of 1487 eV was used. The spectra were collected in a small spot mode ($\approx 110 \text{ mm}^2$) using a 0° take-off angle, defined as the angle between the surface normal and the axis of the analyzer lens. To avoid surface charging, the charge neutralizer was always used during spectra collection (filament current 1.6 Å, charge balance

2 V, and filament bias 1.3 V). The analyzer pass energy was set to 80 eV and a linear background was subtracted for all peak quantifications. The peak areas were normalized by the manufacturer supplied sensitivity factors and atomic compositions were calculated accordingly with CasaXPS software.

10. Acknowledgments

This part was removed from the electronic version of the document.

11. List of Publications

Nick, T. A., Oliveira, T. E. D., Pilat, D. W., Spenkuch, F., Butt, H. J., Helm, M., Netz, P.A. & Berger, R. (2016). Stability of a Split-RNA-Aptamer, Capable of Streptomycin Binding. *The Journal of Physical Chemistry B*.

Pilat, D. W., Pouligny, B., Best, A., Nick, T. A., Berger, R., & Butt, H. J. (2016). Surface forces between colloidal particles at high hydrostatic pressure. *Physical Review E*, 93(2), 022608.

12. List of Presentations

International Conference on Scanning Probe Microscopy on Soft and Polymeric Materials in Kerkrade; Oral presentation: Nick, T. A., Pilat, D. W., Butt, H. J., Helm, M. & Berger, R. “Rupture force based investigation of a split aptamer optimized for tetracycline binding” (2012)

7th Meeting of the GBM Study Group RNA Biochemistry

with workshop „RNA trafficking“; Poster presentation: Nick, T. A., Pilat, D. W., Butt, H. J., Helm, M. & Berger, R. “Rupture force based investigation of a split aptamer optimized for tetracycline binding” (2012)

XVI. Annual Linz Winter Workshop, Poster presentation: Nick, T. A., Pilat, D. W., Butt, H. J., Helm, M. & Berger, R. “Rupture force based investigation of a split aptamer optimized for tetracycline binding” (2014)

XVII. Annual Linz Winter Workshop, Poster presentation: Nick, T. A., Oliveira, T. E. D., Pilat, D. W., Spenkuch, F., Butt, H. J., Helm, M., Netz, P.A. & Berger, R. “Molecular Force Spectroscopy of a Split-Streptomycin-Aptamer” (2015)

IACIS, 15th Conference of the International Association of Colloid and Interface Scientists, Poster presentation: Nick, T. A., Oliveira, T. E. D., Pilat, D. W., Spenkuch, F., Butt, H. J., Helm, M., Netz, P.A. & Berger, R. “Stability of a Streptomycin-Aptamer” (2015)

13. Curriculum Vitae

This part was removed from the electronic version of the document.